MEASUREMENT OF WELD PENETRATION DEPTH USING NON-CONTACT ULTRASOUND METHODS

A Dissertation

Presented to

The Academic Faculty

by

Akio Kita

In Partial Fulfillment
of the Requirements for the Degree
Doctor of Philosophy in School of Mechanical Engineering

Georgia Institute of Technology

August, 2005

Measurement of Weld Penetration Depth using Non-Contact Ultrasound Methods

Approved by:

Dr. I. Charles Ume, Chairman
School of Mechanical Engineering
Georgia Institute of Technology

Dr. Ye-Hwa Chen
School of Mechanical Engineering
Georgia Institute of Technology

Dr. Wayne Book
School of Mechanical Engineering
Georgia Institute of Technology

Dr. Russell Mersereau
School of Electrical and Computer Engineering
Georgia Institute of Technology

Dr. John Buck
School of Electrical and Computer Engineering
Georgia Institute of Technology

Date Approved: June 23, 2003

Acknowledgements

I would like to thank my parents, Drs. Hitoshi and Takako Kita, and my sister, Ryoko Kita, for all of their support and love throughout my life.

I would like to thank my advisor, Dr. Charles Ume, for his guidance, support, and friendship. Dr. Ume has given valuable advice throughout this research project. I have also learned different facets of teaching a class and developed as a teacher from Dr. Ume and his Mechatronics classes.

I would like to thank all of my colleagues for their support: Dr. Bao Mi, Matt Rogge, Rienhard Powell, Carl Hanna, Lizheng Zhang, Dr. Sheng Liu, Dr. Hai Ding, and Wei Tan.

Table of Contents

List of Tables

List of Figures

Summary

Gas Metal Arc welding (GMAW) is one of the primary techniques used to join structural components together. The major obstacle precluding full closed-loop control of GMAW has been the lack of robust techniques using non-destructive and non-contact sensors capable of operating in high temperature and harsh environments typical of GMAW processes. This research uses laser generated ultrasound and electromagnetic acoustic transducer (EMAT) to receive ultrasound. Previous research has focused on ultrasonic shear wave time of flight (TOF) techniques to determine weld penetration depth, a key measure of weld quality.

The objective of this research was to use a new technique, frequency modulation of a laser phased array (FMLPA), to determine weld penetration depth. Theoretical background of the FMLPA was developed. An analytical model of the FMLPA was derived and validated through experimentation. A new EMAT was custom designed to be physically small, more broadband, and with higher signal to noise ratio than the old EMAT. This was designed and developed to assist in validating the FMLPA. The FMLPA was experimentally validated. However, both the FMLPA and shear wave TOF techniques have proven to be impractical for real-time control. These techniques are impractical because the required ultrasonic waves are difficult to acquire due to attenuation and interference from other waves.

A new type of wave called the RGLS wave was discovered during the course of this research. The RGLS wave was used to create a new RGLS TOF method for measuring

weld penetration depth. The RGLS TOF method for measuring weld penetration depth has proven to be highly accurate, precise, and repeatable. The RGLS TOF method for measuring weld penetration depth has been demonstrated to work both off-line after welding and real-time during welding. Although the FMLPA and shear wave TOF technique was proven to be impractical, the RGLS TOF method has met the ultimate goal of this research area. Other new methods such as the RGSL, RGLL, and RGSS TOF method related to the RGLS TOF method was also developed. Weld penetration results using the RGSL, RGLL, and RGSS TOF method are also presented.

The RGLS TOF method is suited for non-destructive and non-contact sensing. It will help future researchers achieve closed-loop control and automation of the GMAW process, which will help to improve quality and efficiency of welding, and also reduce waste and cost of welding parts together.

Chapter 1

Introduction

Gas Metal Arc welding (GMAW) is currently one of the techniques used to join structural components together. GMAW is also referred to as Metal Inert Gas welding (MIG). The American Welding Society changed the name MIG to GMAW after oxygen was added to stabilize the welding arc but in most countries, people continue to use the name MIG. GMAW is achieved by forming an arc between a metal electrode and a workpiece. The electrode melts and is transferred to a weld bead. The transfer is achieved by dipping the molten electrode into the weld bead, spraying the metal onto the weld bead, or forming metal droplets which fall onto the work piece. Shielding gas is used to protect a heated work piece and electrode from atmosphere. Shielding gas also becomes the arc's plasma and stabilizes the arc on the work piece.

Open-loop mechanization of the GMAW process is currently used. Welding parameters such as arc voltage, current, and distance from the work piece are established by a master welder to maintain desired weld geometry, maintain required mechanical properties of the weld, and limit weld discontinuities and defects. The established welding parameters are maintained by mechanization. This method of open loop control assumes that if all welding parameters are maintained within acceptable limits, the desired weld quality will be maintained. Unfortunately there are several disturbances that may affect the GMAW process: variations in seam width, misalignment of the electrode and seam, non-constant

electrode to work piece distance, insufficient shielding gas coverage, and disruption in wire feed rate. These disturbances may cause poor weld shapes, incomplete weld fusion, burn through, splatter, and porosity. Currently, welds are tested after the GMAW process. As a result, malformed or weak weld must be cut out and welded again or must be scrapped. Full closed loop control and automation of the GMAW process is being actively pursued to improve quality, reduce waste, and increase efficiency.

There are two dominant approaches researchers are attempting to model and control the GMAW process. The first approach uses traditional and adaptive controls [1-3]. The second approach uses a combination of neural networks for modeling and fuzzy logic for control [4-13]. Since GMAW processes are highly complex and non-linear, neural networks have predominantly been used to model the process in many recent research projects. Traditional methods of modeling are very simplified due to computational overhead associated with complex models. Simplification usually results in diminished accuracy. Also, creating a traditional model of the GMAW process based on physics and empirical data requires considerable effort. A neural network model is easier to implement. After training, neural network models are comparable to traditional models [14].

In GMAW research, the major obstacle to automated control and defect detection has not been the formulation of models or control algorithms. Instead, the major obstacle is lack of accurate and high resolution non-destructive and non-contact sensors that can operate in high temperature and harsh environments typical of GMAW processes. Sensors

currently used by researchers can be subdivided into four distinct categories: through arc sensing of current and voltage, sensing the thermal distribution in and around the weld pool, weld bead measurement using machine vision, and ultrasonic sensing.

1.1. Through Arc Sensing of Current and Voltage

The GMAW process can be viewed as a simple circuit consisting of a voltage source and two resistors. The positive terminal of the voltage source is the welding gun. The negative terminal of the voltage source corresponds to the work piece. The shielding gas between the electrode and work piece is the first resistor and the weld pool is the second resistor. Disturbances to the GMAW process are detected by measuring disturbances in the current and voltage of the circuit. The major disadvantage is that weld bead geometry or defects are not measured directly. However, this method is useful for detecting disturbances in the welding process. [5,7,9,13,14,16]

There are two main advantages to using through arc sensing of current and voltage: it is non-contact and economical. It is non-contact because current and voltage can be measured within the welding machine. It is economical because current and voltage is easily measured using cheap and available devices.

1.2. Thermal Distribution Sensor

During the GMAW process, temperature gradients on the top and bottom surfaces of the workpiece contain very useful information. Asymmetrical temperature gradients along

the seam indicate that the welding torch is not tracking the seam properly. Modeling the thermal energy absorbed by the workpiece and measuring temperature gradients along the bottom surface of the workpiece allows calculation of penetration depth. Measurements of the thermal distribution on the top surface can be used to indicate weld pool width and shape.

An infrared charge coupled device (CCD) camera provides a non-contact, direct, and digital method of measuring temperature gradients. In order to filter energy radiated directly from the arc, infrared wavelengths above 2 μm should be measured. There are several advantages of this sensing method. Sensors are non-contact and are available commercially. In addition, this method can measure the weld pool shape directly. The flaws within the volume of the material cannot be detected; however, this system can detect conditions in which flaws are likely to occur. [1,2,17]

1.3. Machine Vision

The sensor used in machine vision is a simple CCD camera and an image processing system. Direct pictures can be taken of the weld pool. Edge detection algorithms can be used to accurately outline the shape of the weld pool. By controlling the shape of a weld pool, weld consistency can be controlled. Machine vision techniques are also very good at seam tracking. Weld reinforcement height can also be measured. A laser stripe shines incident on the weld bead at an acute angle and a camera is placed directly over the stripe. The camera will see a "bump" in the line. The height of the bump is assumed to be proportional to weld reinforcement height. [3]

The advantages and disadvantages of a machine vision sensor are similar to the thermal distribution sensor. The advantages are the sensors are non-contact, CCD cameras are easily obtainable and available commercially, and this method can measure the weld pool shape directly. The disadvantage of this system is it cannot detect flaws within the volume of the material. [4,6,8,18]

1.4. Ultrasound Inspection

Ultrasonic inspection systems have been developed for a variety of purposes including crack detection in ceramics and airplane bodies; however, the application of ultrasound to measure weld bead dimensions and detect flaws is relatively new. Recent research includes rudimentary seam tracking [19,20].

For non-contact ultrasound generation, pulsed lasers and electro-magnetic acoustic transducers (EMAT) can be used. Pulsed lasers with nanosecond rise-times including Q-switched Neodymium doped Yttrium Aluminum Garnet (Nd:Yag) lasers and transversely excited atmosphere (TEA) CO2 lasers can be used to generate ultrasound. Using low power densities, thermoelastic generation can be achieved by rapid cycling of heat at a point on a surface. Thermal strain at the point causes a shearing motion within the material. At higher power densities, ablation occurs and the surface will recoil. Both of these methods will create ultrasonic waves within a material. In general, the ablative laser generation methods create stronger ultrasound. Focusing the generated ultrasound in a particular direction or using arrays of sources to create a stronger ultrasonic signal is

being researched [21-24]. Also the effect of heat generated by the welding process on ultrasound path has been researched. [25] EMATs consist of a static magnetic field and an oriented pick-up coil. When a large current is pulsed through the coil, eddy currents are induced in nearby metals. The Lorentz force interaction between the eddy currents and static magnetic field creates ultrasound within the sample.

EMATs are also non-contact receivers of ultrasound. EMAT reception of ultrasound works in the exact opposite of EMAT generation. The design, simulation, and optimization of EMATs is still being researched [26-29]. Signal filtering aside from the usual band-pass filtering and data averaging routines are being researched since the GMAW process creates electro-magnetic noise. Laser interferometry can be utilized for the non-contact reception of ultrasound. However, workpiece surfaces rarely have the optical qualities needed to use this method [30]. Also, over a wide frequency band EMATs are more sensitive to displacement than an interferometer [31].

The advantages to using ultrasound for sensing the GMAW process are obvious. This method allows for the direct measurement of the weld bead within the workpiece volume. It can detect internal defects, penetration depth, weld reinforcement height, and reinforcement width. The disadvantages are also obvious. Generation of ultrasound using EMATs and pulsed lasers are relatively new. Research in EMAT optimization and design for reception, signal filtering, and signal interpretation is sparse. Prior research has focused on using the time of flight (TOF) of a shear wave to measure weld penetration depth. [25,32-34]

Chapter 2

Background

This research project uses ultrasound to measure weld beads and weld quality because of its ability to measure a weld bead and surrounding structure directly. A Q-switched Nd:Yag laser is used to create ultrasound and an EMAT is used to receive ultrasound. It is imperative to discuss ultrasonic waves before discussing laser generation of ultrasound and EMAT reception of ultrasound.

2.1. Ultrasonic Waves

2.1.1. *Ultrasonic Bulk Waves*

In isotropic solids, two types of bulk waves can be produced: shear (transverse) and longitudinal (compression). The two waves travel at different speeds through a given material: shear speed C_S and longitudinal speed C_L. These speeds depend on Eq. 2-1 where λ and μ are Lame constants and ρ is the density. [22] In steel, longitudinal waves travel at 5960 m/s whereas shear waves travel at 3240 m/s.

$$C_S = \sqrt{\frac{\mu}{\rho}} \qquad C_L = \sqrt{\frac{\lambda + \mu}{\rho}} \qquad \textbf{Eq. 2-1}$$

When either a shear or longitudinal wave reflects from a flat boundary, shear and longitudinal waves are created. Eq. 2-4 through Eq. 2-3 are used to calculate amplitudes and reflection angles of the two reflected waves. [22]

For incident longitudinal waves:

$$\theta_L = \theta_I$$
$$\sin\theta_S = \kappa^{-1}\sin\theta_I$$
$$\frac{A_L}{A_I} = \frac{\sin 2\theta_I \sin 2\theta_S - \kappa^2 \cos^2 2\theta_S}{\sin 2\theta_I \sin 2\theta_S + \kappa^2 \cos^2 2\theta_S} \qquad \textbf{Eq. 2-2}$$
$$\frac{A_S}{A_I} = \frac{2\kappa \sin 2\theta_I \sin 2\theta_T}{\sin 2\theta_I \sin 2\theta_S + \kappa^2 \cos^2 2\theta_S}$$

For incident shear waves:

$$\theta_S = \theta_I$$
$$\sin\theta_L = \kappa \sin\theta_I$$
$$\frac{A_S}{A_I} = \frac{\sin 2\theta_I \sin 2\theta_L - \kappa^2 \cos^2 2\theta_I}{\sin 2\theta_I \sin 2\theta_L + \kappa^2 \cos^2 2\theta_I} \qquad \textbf{Eq. 2-3}$$
$$\frac{A_L}{A_I} = \frac{\kappa \sin 4\theta_I}{\sin 2\theta_I \sin 2\theta_L + \kappa^2 \cos^2 2\theta_I}$$

where:

$$\kappa = \frac{C_L}{C_S} \qquad \textbf{Eq. 2-4}$$

θ_I : Angle of incidence of incident wave in relation to boundary normal

θ_L : Angle of reflected longitudinal wave

θ_S : Angle of reflected shear wave

A_I : Amplitude of incident wave

A_L : Amplitude of reflected longitudinal wave

A_S : Amplitude of reflected shear wave

2.1.2. *Ultrasonic Surface Waves*

Rayleigh waves are the primary surface waves. Rayleigh waves displace material in two different directions: a displacement normal to the surface and a displacement parallel to the propagation direction shifted 90^o in relation to the normal displacement. The Rayleigh wave speed can be calculated with Eq. 2-5 by solving for C. The Rayleigh wave speed, C_R, is the real root C less than C_S. [22]

$$\left(2-\frac{C^2}{C_S^2}\right)-4\left(1-\frac{C^2}{C_L^2}\right)^{\frac{1}{2}}\left(1-\frac{C^2}{C_S^2}\right)^{\frac{1}{2}}=0 \qquad \textbf{Eq. 2-5}$$

A vertical transverse wave, shear vertical (SV), can create a non-Rayleigh surface wave. If a SV wave is incident on a surface and the calculated reflection angle of the reflected longitudinal wave is complex, a non-Rayleigh surface wave will be created. The speed of this surface wave, C_{sw}, is dependent on the speed of the transverse wave as shown in Eq. 2-6. [22]

$$C_{SW}=\frac{C_S}{\sin\theta_L} \qquad \textbf{Eq. 2-6}$$

2.2. Laser Generation of Ultrasound

There are three distinct ways laser generation of ultrasound can occur: thermoelastic, transition, and ablative. The mode of generation is selected by varying power density, the irradiated power per surface area.

2.2.1. *Thermoelastic*

Focusing a pulsing laser on a workpiece surface with low power densities expands and contracts a small cylinder of the workpiece by thermoelastic expansion and contraction. Normal forces arising from thermoelastic expansion and contraction can be ignored since the height of the heated cylinder is very small compared to the diameter of the cylinder in metals [35]. Along any vector on the surface that originates from the middle of the cylinder, forces generated from the expansion of the surface will appear as two forces: both originating from the middle of the cylinder, with equal magnitude, and with opposite directions along the vector. This has been modeled as a force dipole acting in the surface plane as shown in Fig. 2-1. [36]

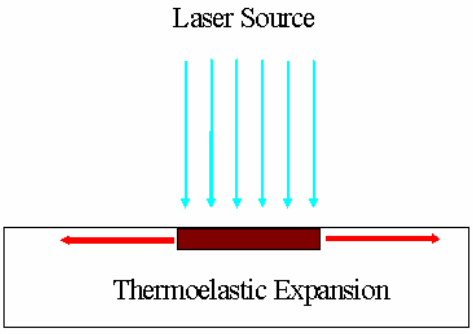

Fig. 2-1 : Thermo-Elastic Laser Ultrasound Generation

A directivity pattern is the variation of the generated wave amplitude with respect to the angle measured from the surface normal pointing into the workpiece. The directivity pattern created from a force dipole acting in the surface plane is given by Eq. 2-7 and Eq. 2-8. [36] Thermoelastic directivity patterns for steel are shown in Fig. 2-2.

$$u_L \propto \frac{\sin\theta \sin 2\theta \sqrt{\kappa^2 - \sin^2\theta}}{\left(\kappa^2 - 2\sin^2\theta\right)^2 + 4\sin^2\theta\sqrt{1-\sin^2\theta}\sqrt{\kappa^2 - \sin^2\theta}} \qquad \textbf{Eq. 2-7}$$

$$u_s \propto \frac{\kappa \sin 4\theta}{\kappa\left(1-2\sin^2\theta\right)^2 + 4\sin^2\theta\sqrt{1-\sin^2\theta}\sqrt{1-\kappa^2\sin^2\theta}} \qquad \textbf{Eq. 2-8}$$

where:

θ : Angle measured from the surface normal pointing into the work piece

u_l : Directivity of longitudinal waves

u_s : Directivity of shear waves

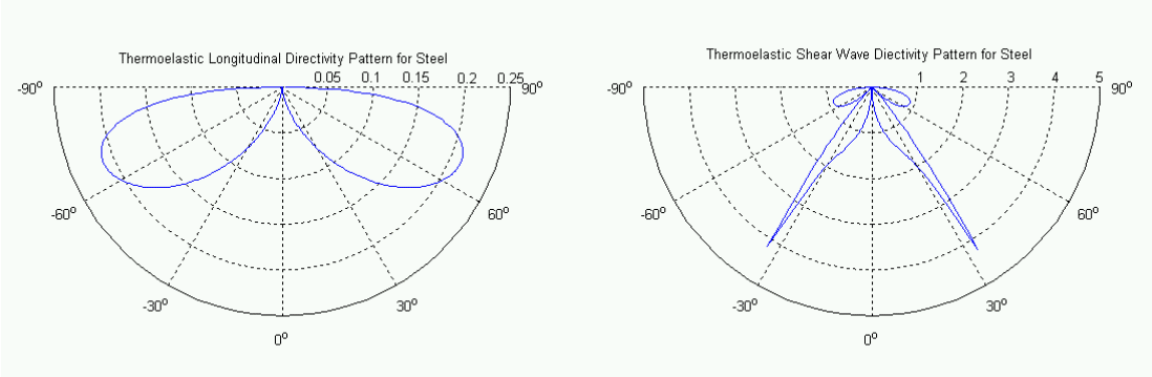

Fig. 2-2 : Thermoelastic Directivity Patterns for Steel

The frequency of the generated wave depends on the time it takes to heat and cool the material. Pulsed Lasers with nanosecond rise-times including Q-switched Nd:Yag lasers and TEA CO2 lasers can heat the material fast enough to generate ultrasonic waves.

The strongest ultrasound by thermoelastic generation occurs when differences between the heated and unheated temperatures of the work piece is large. With elevated temperatures within a GMAW work piece, power density has to be increased to get a large temperature variation. At some threshold, the power density will be strong enough to ablate the workpiece. When this point is reached, ablative ultrasound generation will dominate.

2.2.2. *Transition*

This mode of ultrasonic generation is not used and is not well documented in literature.

2.2.3. *Ablative*

When the power density is increased enough to vaporize a small portion of the workpiece, the surface will recoil as mass leaves the workpiece. The force of the recoil can be modeled as an impulse force along the surface normal pointing within the workpiece as shown in Fig. 2-3. Similar to the thermoelastic mode of generation, a pulsed laser with a fast enough rise time will create ultrasonic waves.

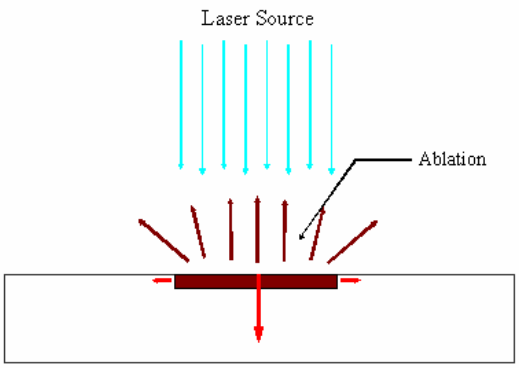

Fig. 2-3 : Ablative Laser Ultrasound Generation

The directivity of the generated ultrasound by an impulse force is given by Eq. 2-9 and Eq. 2-10. [36] The ablative directivity pattern for steel is shown in Fig. 2-4 .

$$u_L \propto \frac{2\kappa^2 \cos\theta\left(\kappa^2 - 2\sin^2\theta\right)}{\left(\kappa^2 - 2\sin^2\theta\right)^2 + 4\sin^2\theta\sqrt{1-\sin^2\theta}\sqrt{\kappa^2-\sin^2\theta}} \qquad \textbf{Eq. 2-9}$$

$$u_S \propto \frac{\sin 2\theta\sqrt{1-\kappa^2\sin^2\theta}}{\kappa\left(1-2\sin^2\theta\right)^2 + 4\sin^2\theta\sqrt{1-\sin^2\theta}\sqrt{1-\kappa^2\sin^2\theta}} \qquad \textbf{Eq. 2-10}$$

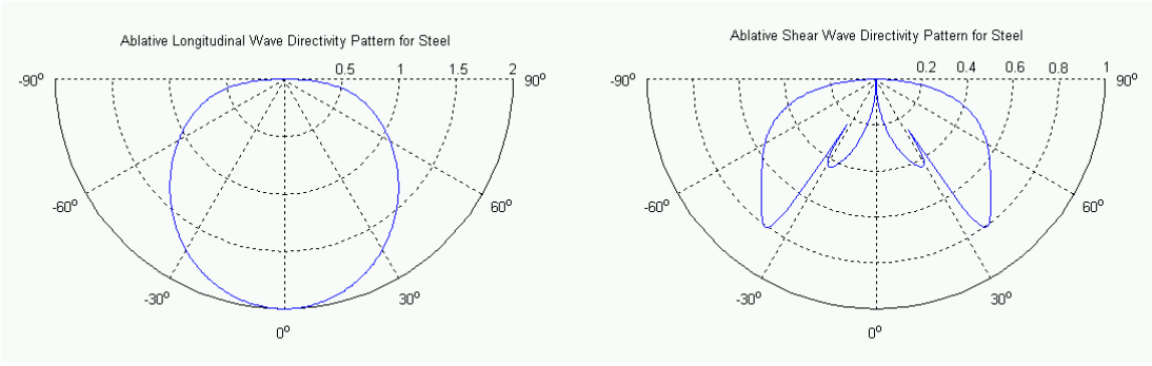

Fig. 2-4 : Ablative Directivity Pattern for Steel

Typically, stronger waves are created using the ablative mode of ultrasound generation than thermoelastic, especially in GMAW because of elevated work piece temperatures [22].

2.2.4. *Phased Array Generation*

If multiple laser sources are incident on a workpiece surface, the ultrasonic wave fronts generated from each source interacts to create a three-dimensional interference pattern within a workpiece. Each laser source with a unique location and time of irradiation is considered an array member. A collection of array members constitutes a phased array. Temporal and spatial arrangement of the ultrasonic wave fronts generated by each array member controls the interference pattern. Phased arrays can be used to enhance amplitudes of waves propagating towards a specific region of interest within a workpiece. This method of amplifying ultrasound to a specific region of interest is called beam steering. The phased array directivity pattern $u(\theta,\phi)$ of the ultrasound is the product of the array member directivity pattern $u_e(\theta)$ produced by an individual array member and the array gain $I_a(\theta,\phi)$ as shown in Eq. 2-11. [37]

$$u(\theta,\phi) = u_e(\theta) \cdot I_a(\theta,\phi) \qquad \textbf{Eq. 2-11}$$

The array gain is given by Eq. 2-12. [37]

$$I_a(\theta,\phi) = \left(\frac{\sin Nq}{N \sin q} \right)^2 \qquad q = \frac{\pi d}{\lambda}(\sin\theta - \sin\phi) \qquad \textbf{Eq. 2-12}$$

where:

θ : Angle measured from the surface normal pointing into the work piece

ϕ : Beam steering angle

N : Number of array members

d : Distance between array members

τ : Time delay between array members

λ : Acoustic wavelength of the propagating wave:

The beam steering angle is derived from simple trigonometry and Huygen's Principle and is given in Eq. 2-13.

$$sin(\phi) = \frac{\tau c_{L,S}}{d} \qquad \textbf{Eq. 2-13}$$

This formulation assumes that at a particular angle, individual hemispherical wave fronts will combine into a linear wave front as shown in Fig. 2-5.

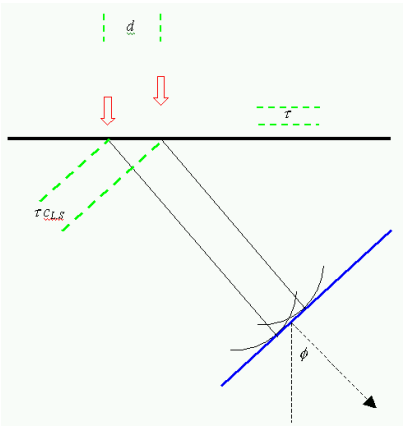

Fig. 2-5 :Wave fronts at Beam Steering Angle

It is important to note that the beam steering angle is not dependent on the frequency of the ultrasonic wave. However, the array gain equations are dependent on frequency and are valid for continuous waves only.

2.3. EMAT Reception

EMATs are relatively simple devices. An EMAT is comprised of a permanent magnet and a pickup coil as shown in Fig. 2-6. A small mass accelerating within a body has a velocity, v. Within an electrically conductive material with conductivity, σ, the velocity of the small mass interacts with a stationary magnetic field , B, radiating from an EMAT's permanent magnet to create eddy currents , J, as shown in Eq. 2-14. These eddy currents then induce a current in the pickup coil [38].

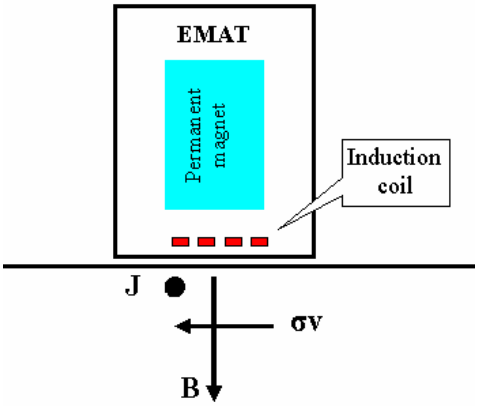

Fig. 2-6 : Schematic of EMAT

$$J = \sigma v \times B \qquad \textbf{Eq. 2-14}$$

EMATs have several advantages and disadvantages. EMATs are non-contact devices and can be moved without re-application of couplant. The non-contact nature of this device is suitable for automated inspection systems that require various testing points within a part. EMATs can be tuned to different frequencies and ultrasonic wave types. As with many electromagnetic materials, EMATs serve dual purposes. EMATs can be used to generate or receive ultrasonic signals. However, EMATs can only be used to measure

ultrasonic waves within a conductive material. Other shortcomings of EMATs include susceptibility to electro-magnetic noise and inefficiency.

2.4. Frequency Modulation of Laser Phased Array (FMLPA)

The ultrasound signal generated by a single laser pulse is broadband. A broadband signal is harder to filter from broadband noise than a narrowband signal. There are two methods to narrow the generated ultrasound's bandwidth. Temporal modulation of the laser source can narrow the bandwidth of the system by increasing power at the modulation frequency [39]. Array generation can also be used to modulate ultrasound if the ultrasound is sufficiently broadband. If an array is temporally phased but not spatially phased, the power at a particular frequency determined by the temporal phasing will increase; thus, the ultrasound's bandwidth will be narrowed and centered at this frequency [40]. A temporally phased array has the effect of introducing temporal modulation before the ultrasound is generated. If an array is spatially phased but not temporary phased, the differing distances from the generation point to the reception point and constant ultrasound speed will create temporal modulation. A spatially phased array has the effect of introducing temporal modulation after the ultrasound has been generated. A laser phased array with both temporal and spatial phasing will have modulation properties as well. Laser generated ultrasound is broadband and individual wave fronts do not interfere with each other at angles away from the steering angle [37]. In the situation where individual wave fronts created by the laser phased array do not interfere with each other, the array gain models do not apply. However, frequency modulation of ultrasound will occur. The modulation frequency will depend on wave front arrival time differences

Δt. Fig. 2-7shows a diagram of the wave fronts. Formulas for calculating the FMLPA are shown in Eq. 2-15 and Eq. 2-16.

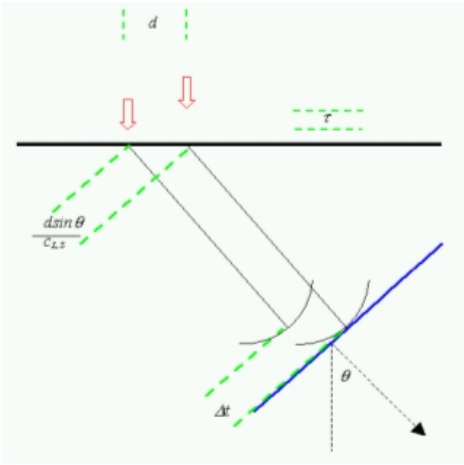

Fig. 2-7 : Wave fronts Away From Beam Steering Angle

From Fig. 2-7, the difference in wave front arrival time is:

$$\Delta t = \tau - \frac{d \ sin \ \theta}{c_{L,S}} \qquad \textbf{Eq. 2-15}$$

The FMLPA is:

$$f\,mod = \frac{1}{\Delta t} = \frac{c_{L,S}}{\tau c_{L,S} - d \sin\theta} \qquad \textbf{Eq. 2-16}$$

Plots of the FMLPA for steel longitudinal and shear waves, 2.1 mm d-spacing, and 2.43×10^{-7}sec time delay, are given in Fig. 2-8:

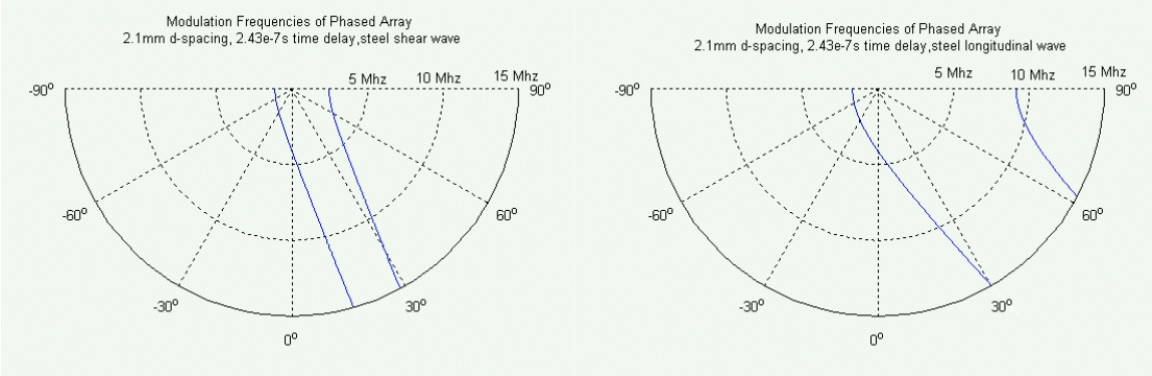

Fig. 2-8 : FMLPA for Steel

The FMLPA is dependent on the angle normal to the surface. The FMLPA are the same for both thermoelastic and ablative generation of laser ultrasound since both generation methods are broadband.

The change in FMLPA, $\Delta f\ mod$, due to change of d-spacing, Δd, is given by Eq. 2-17.

$$\Delta f\ mod = \frac{c_{L,S}}{(\tau c_{L,S} - (d + \Delta d)\sin\theta)} + \frac{c_{L,S}}{(\tau c_{L,S} - d\sin\theta)} \qquad \textbf{Eq. 2-17}$$

Plots of change in FMLPA, $\Delta f\ mod$, for steel longitudinal and shear waves, 2.1 mm d-spacing, 0.1 mm error in d-spacing, and 2.43×10^{-7}sec time delay, are given in Fig. 2-9. As Fig. 2-9 indicates, the FMLPA is sensitive to d-spacing errors.

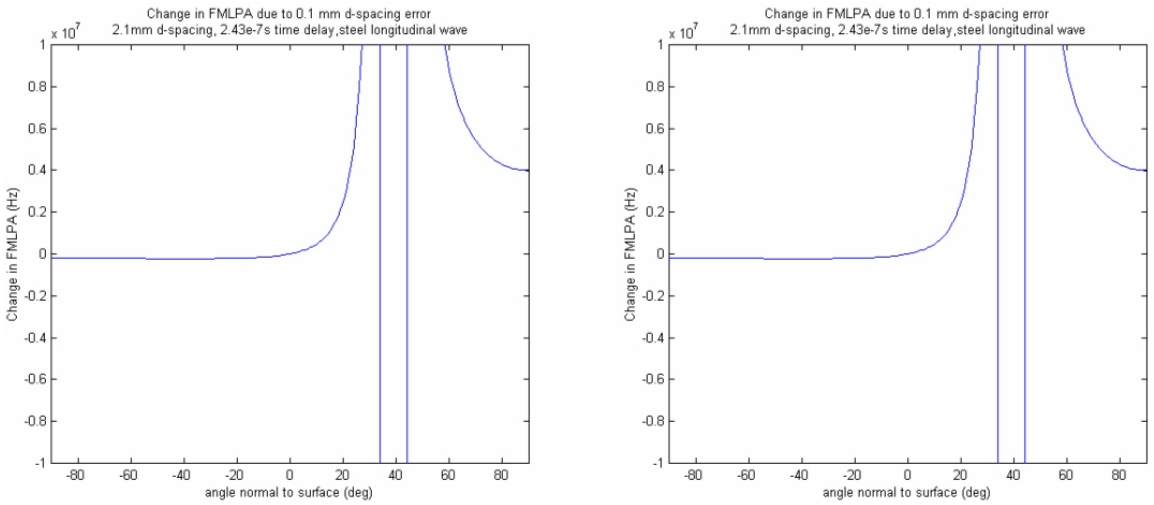

Fig. 2-9 : Change in FMLPA due to d-spacing error

To use the FMLPA in weld penetration depth measurements, the weld penetration depth must be related to the FMLPA of a received ultrasonic wave. Weld penetration depth and FMLPA of a received ultrasonic wave are related within an isotropic material where the angle of reflection of a bulk wave is the same as the angle of incidence and the ultrasound generation point is the same distance from the weld bead as the reception point. This is shown in the simple ray tracing as shown in Fig. 2-10.

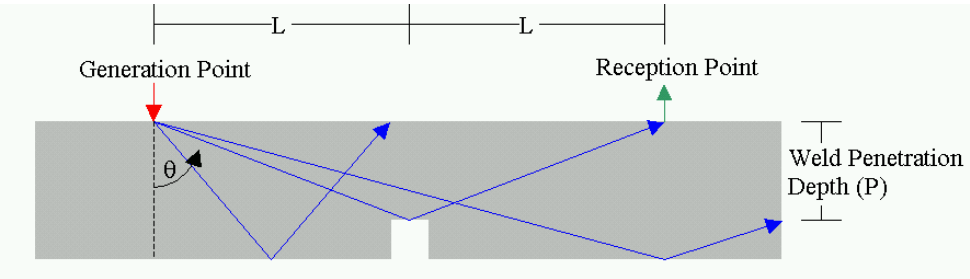

Fig. 2-10 : Simple Raytrace of Ultrasound through workpiece

Only one ultrasonic wave angle, θ, from the generated ultrasound will be received at the reception point if only one reflection is allowed. The relationship between θ, the penetration depth , $d_{penetration}$, and the distance between generation point and weld bead , L, is given by Eq. 2-18 to Eq. 2-20.

$$d_{penetration} = \frac{L}{tan(\theta)} \quad \textbf{Eq. 2-18}$$

By re-arranging equation Eq. 2-16, the relationship between θ and f_{mod} can be shown as:

$$\theta = arcsin\left(\frac{\tau \cdot c_{L,S}}{d} - \frac{c_{L,S}}{d \cdot f_{mod}}\right) \quad \textbf{Eq. 2-19}$$

Then by substituting Eq. 2-19 into Eq. 2-18, the relationship between P and f_{mod} is:

$$d_{penetration} = \frac{L}{tan(arcsin\left(\frac{\tau \cdot c_{L,S}}{d} - \frac{c_{L,S}}{d \cdot f_{mod}}\right))} \quad \textbf{Eq. 2-20}$$

Using the above relationship, the penetration depth can be determined by finding the modulated frequency of the received ultrasound. The modulation frequency is easily found by taking the Discrete Fourier Transform of a received ultrasonic signal. Increasing the number of samples taken can increase resolution of the measurement. TOF flight information can be used to determine if a shear wave or longitudinal wave was received.

As previously mentioned, TOF can also be used to find the penetration depth by the relationship given by Eq. 2-21. [25]

$$P = \sqrt{\left(\frac{TOF \cdot c_{L,S}}{2}\right)^2 - L^2} \quad \textbf{Eq. 2-21}$$

Chapter 3

Experimental Setup From Previous Research

This section describes the experimental setup used in prior research. A robotic welding system is used to weld two strips of 1018 steel. A laser phased array is used to generate ultrasound on one side of the weld bead. An EMAT is used to receive ultrasound on the opposite side of the weld bead. A diagram of the experimental setup is given in Fig. 3-1. Equipment used is listed below:

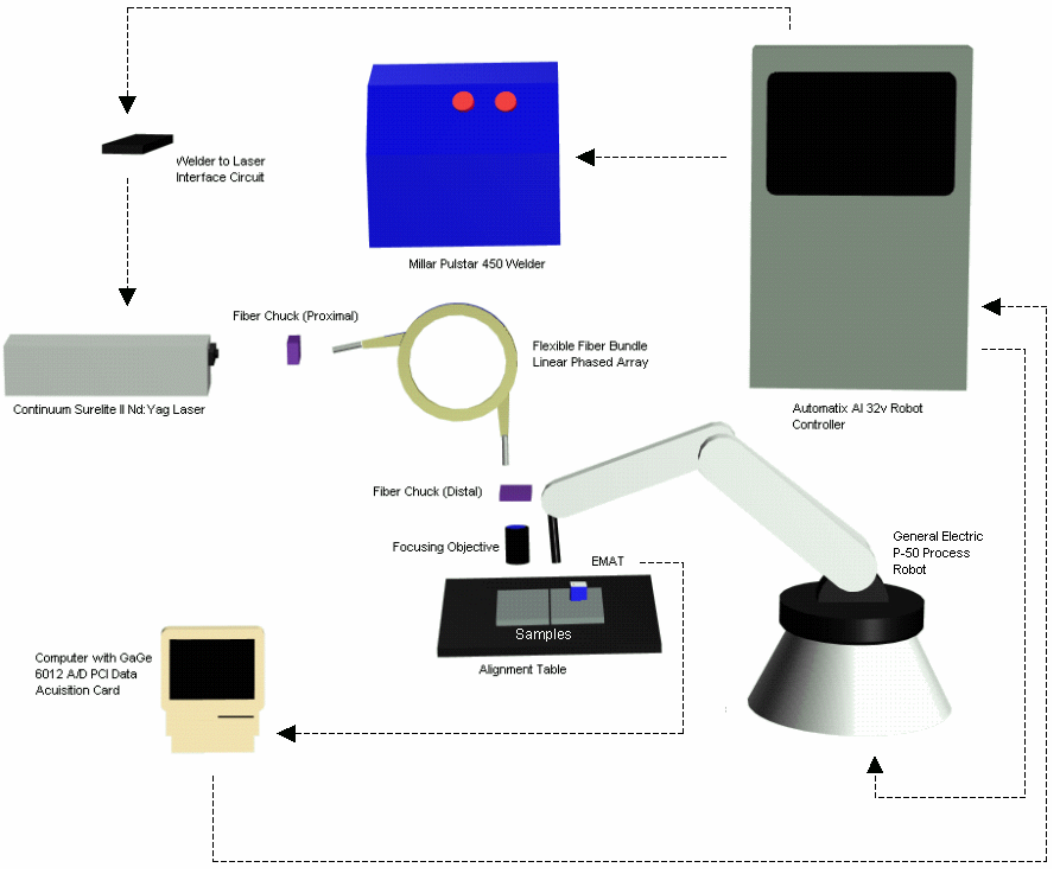

Fig. 3-1 : Experimental Setup

Laser

Continuum Surelite II Nd:Yag Laser used at 1064 nm wavelength.

Repetition Rate : 10 pulses/sec
Energy : 650 mJ/pulse
Pulsewidth : 5-7 ns
Divergence: 0.6 mrads
Energy Stability : 0.5 %
Power Drift: 3%

Laser Phased Array

Three bundles of fibers are used within the laser phased array. The first bundle consists of seven 2 m fibers. The second bundle consists of seven 52 m fibers. The third bundle consists of seven 102 m fibers. The output of the seven fibers in each bundle is placed right next to each other in order to create a line source. For the remainder of this document, each bundle will be referred to as a "seven fiber linear array member" since each bundle will be considered as a single array member. The term "array member" will be used to specify a laser source with a unique location and time of irradiance on a surface as described in Chapter 2.24. The term "phased array" will refer to a set of array members and is also described in Chapter 2.2.4. Since the laser phased array is a set of array members, the laser phased array has both temporal and spatial spacing. The laser is coupled into the fibers at the array's proximal end. Output from the array's distal end is focused onto a sample surface. The laser phased array output pattern is shown in Fig. 3-2. Power from the distal end of the fiber bundle is shown in Fig. 3-3.

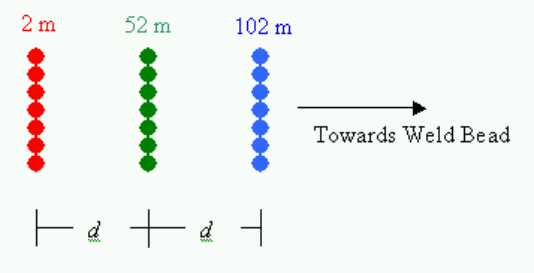

Fig. 3-2 : Phased Array Output on Work Piece

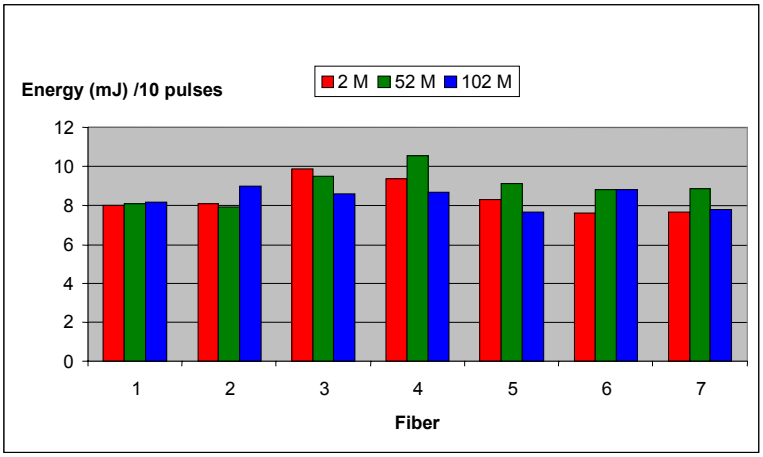

Fig. 3-3 : Energy Distribution among fibers

The time delay between the fibers can be calculated and is $2.43x10^{-7}$s as shown in Eq. 3-1.

Length Difference between fiber bundles: $\Delta l = 50$ m

Speed of light: $c = 3x10^{8}$ m/s

Index of refraction of fiber optics: $n = 1.46$

$$\tau = \frac{\Delta l \cdot n}{c} = \frac{50m \cdot 1.46}{3x10^{8} m/s} = 2.43x10^{-7} s \qquad \textbf{Eq. 3-1}$$

Since there has been accidental damage and shortening of the fibers, the calculated time delay is not correct. The measured time delay between the 2 m seven fiber linear array

member and 52 m seven fiber linear array member is $2.12x10^{-7}$ sec. The measured time delay between the 52 m seven fiber linear array member and 102 m seven fiber linear array member is $2.46x10^{-7}$ sec. The averaged time delay between fibers is $2.29x10^{-7}$s sec. [25]

Fiber Optics

Fibers used in the array are Ceramoptec Optran WF400/440 Silica fibers with high temperature Polyimide jacketing.

Spectra Range: 350-2500 nm
Temperature Range: -190^{o} to $+400^{o}$ C
Laser Damage Threshold: Nd:Yag 5.4 J/mm^2 (1 ms pulse) at 1060 nm
Core Diameter: 400 μm
Cladding Diameter: 440 μm
Jacketing Diameter: 470 μm
Index of refraction (n): 1.46 at 1064 nm wavelength

Flexible Fiber Bundle Linear Phased Array (Hopko)

A Flexible Fiber Bundle Linear Phased Array (patent pending) is used to contain fiber optics in a manageable bundle and protect fiber optics from weld splatter.

Focusing Objective (Hopko)

A custom focusing objective (patent pending) is used to focus laser power leaving the fiber optics onto a sample surface. Thermoelastic or Ablative generation of ultrasound can be obtained by varying the focal length of the focusing objective.

Fiber chuck- proximal (Mi)

A custom fiber chuck is used to align the proximal end of the fiber optics to the laser output.

Fiber chuck- distal (Kita)

A custom fiber chuck is used to hold fiber optics in an array pattern. The distance between array members can be adjusted.

Navy EMAT System

The Navy EMAT system used in this project was developed at the National Institute of Science and Technology (NIST) and was donated to Georgia Tech by the United States Navy. The Navy EMAT system consists of an EMAT, differential pre-amplifier, and band-pass filter.

The Navy EMAT housing is 0.105 m (4.13 in) long, 0.069 m (2.70 in) wide, and 0.160 m (6.18 in) high. It is protected from weld splatter by a sheet metal shield coated with welding anti-splatter. It is cooled with dry nitrogen at 10 psi since the Navy EMAT can experience elevated temperatures during welding. The Navy EMAT has a frequency response range from 30 kHz to 30 MHz. The detection aperture containing the induction coil of the Navy EMAT is 14.29 mm wide by 14.29 mm long and is located in the center of the bottom face of the Navy EMAT housing. The induction coil is a 25 turn, counter wound, center tapped coil. The coil outputs a differential voltage signal that is amplified by the differential pre-amplifier. The pre-amplified output is then sent to a 0.5 Mhz to 2 Mhz band-pass filter. The signal is digitized after filtering.

Data Acquisition System

A GaGe 6012 PCI A/D card is used to digitize signals. The card is installed on a 1 GHz Pentium III IBM compatible system.

Amplitude Resolution: 12 bit
Gain settings: 100 mV, 200 mV, 500 mV, 1 V, 2 V, 5 V, 10 V
Input Impedance: 50 Ω or 1M Ω
Single Channel maximum sample rate: 60 Mhz (16.7 ns time resolution)
Dual Channel maximum sample rate: 30 Mhz (33.4 ns time resolution)
Maximum number of samples per trigger: 1048576

Robot

The robot used is a General Electric 5 axis P-50 Process robot. An Automatix AI 32v controller running RAIL v6.04 is used to control this robot.

Welder

The welding machine used is a Miller Pulstar 450. A mixture of 98% Argon and 2% Carbon dioxide is used as shielding gas. The torch is mounted on the P-50 Process robot's end effector. The Automatix AI 32v controller remotely controls the Miller Pulstar 450.

Alignment Table (Mi)

A custom alignment table was machined in order to keep spatial relationships of the ultrasound generation point, samples, and ultrasound reception point constant.

Welder to Laser interface (Kita)

A circuit based on the Microchip PIC16F84 micro controller is used to interface the welder and laser. The welder can activate the laser with appropriate firing settings when welding starts. The Microchip 16F84 micro-controller is re-programmable for future equipment changes.

Acquisition program (Kita)

A Microsoft Windows compatible acquisition program was written in Borland C++ Builder. The new program can take full advantage of the acquisition speed of the GaGe 6012 PCI A/D. It is capable of storing A/D samples at 60 Mhz sampling rate on a Pentium I class computer. This program can be used with other GaGe Data Acquisition Products.

Analysis Program (Kita)

This Microsoft Windows compatible program can be used to average data samples, find times when data amplitude crosses a threshold, and take Fast Fourier Transforms of the signals. This program was written in Borland C++ Builder.

Chapter 4

LURL EMAT

A new custom EMAT (LURL EMAT) was developed to be physically smaller and more broad band than the Navy EMAT. The signal quality obtained using the LURL EMAT is significantly better than the Navy EMAT in terms of signal to noise quality, less chirp, and frequency range. A comparison picture of the LURL EMAT and Navy EMAT is shown in Fig. 4-1.

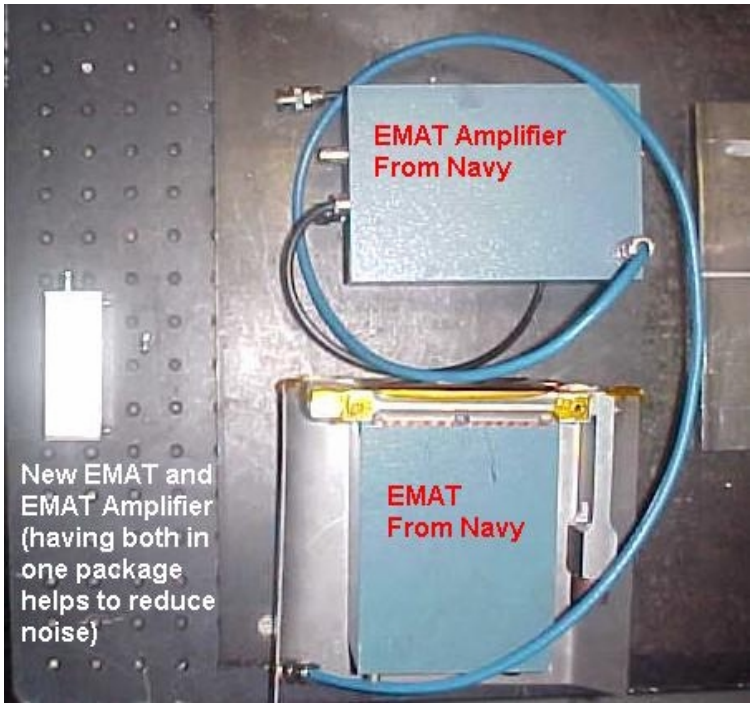

Fig. 4-1 : Comparison of the LURL and NAVY EMATs

All components of the new LURL EMAT is encased in a 1.25”x 1.25”x 4” aluminum square stock. A 0.75” x 0.75” x 0.25” rectangular neodymium magnet provides a permanent magnetic field. Eddy currents are picked up by 30 Ω coil of 44 gauge copper

wire in a racetrack configuration fiber-glassed to one pole face of the neodymium magnet. A National Semiconductor LMH6624 broad band amplifier with a bandwidth of up to 1.5 GHz was used as a differential amplifier. Effort was made to keep leads from the coil to amplifier as short as possible. Surface mount components were used in order to fit a 9V battery for the amplifier, the amplifier, magnet, and coil inside of the square stock. The new LURL EMAT was used in conjunction with an adjustable Khronhite filter. The Khronhite filter was configured as a band pass filter from 100 kHz to 5 Mhz to prevent low frequency noise and aliasing.

Chapter 5

Validation of FMLPA and Array Gain Models

5.1 Experimental Setup

Ultrasonic waveforms were recorded along the top of a half cylinder in order to validate theoretical FMLPA. The experimental setup is shown in Fig. 5-1. Distance "R" between laser phased array and sensor was kept constant. The laser phased array described in chapter 3 was focused on the diametric flat surface of the half cylinder to ablatively generate ultrasound. Ultrasonic waveforms were taken using the LURL EMAT. A V153 Panametrics "Video-scan" piezo-electric transducer (PZT) was also used to validate the LURL EMAT.

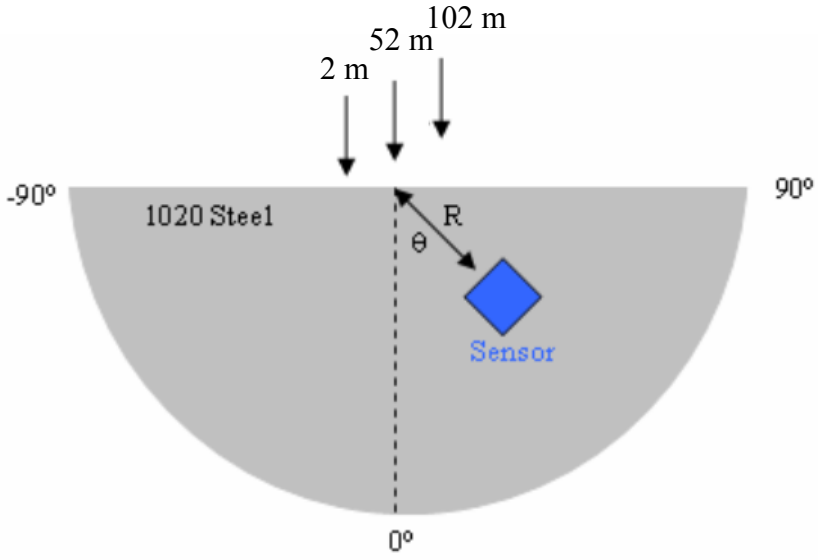

Fig. 5-1 : Experimental Setup for Validation of FMLPA

5.2. Feasibility of FMLPA

The FMLPA method relies on two criteria:

1. At angles away from the beam steering angle, ultrasound generated by each laser phased array members do not interfere with each other
2. Ultrasound generated by each individual laser phased array member can be detected

Signals obtained using the LURL EMAT positioned at $\theta = -80^{o}$ are shown in Fig. 5-2. Fig. 5-3 shows similar results using a V153 PZT. Theoretically, ultrasound from the 2 m seven fiber linear array member should arrive at the LURL EMAT followed by ultrasound from the 52 m seven fiber linear array member and then ultrasound from 102 m seven fiber linear array member. The first waveform is with no array members blocked. There are three peaks observable in the waveform corresponding to the three array members. The second waveform is with the 2 m seven fiber linear array member blocked. The first peak corresponding to the 2 m seven fiber linear array member is gone in the second waveform. The third with the 52 m seven fiber linear array member blocked shows the second peak corresponding to the 52 m seven fiber linear array member is gone. The fourth with the 102 m seven fiber linear array member blocked shows the third peak disappearing since the third peak corresponds to the 102 m seven fiber linear array member. These waveforms prove that laser phased array ultrasound do not interfere with each other away from the beam steering angle and can be observed individually.

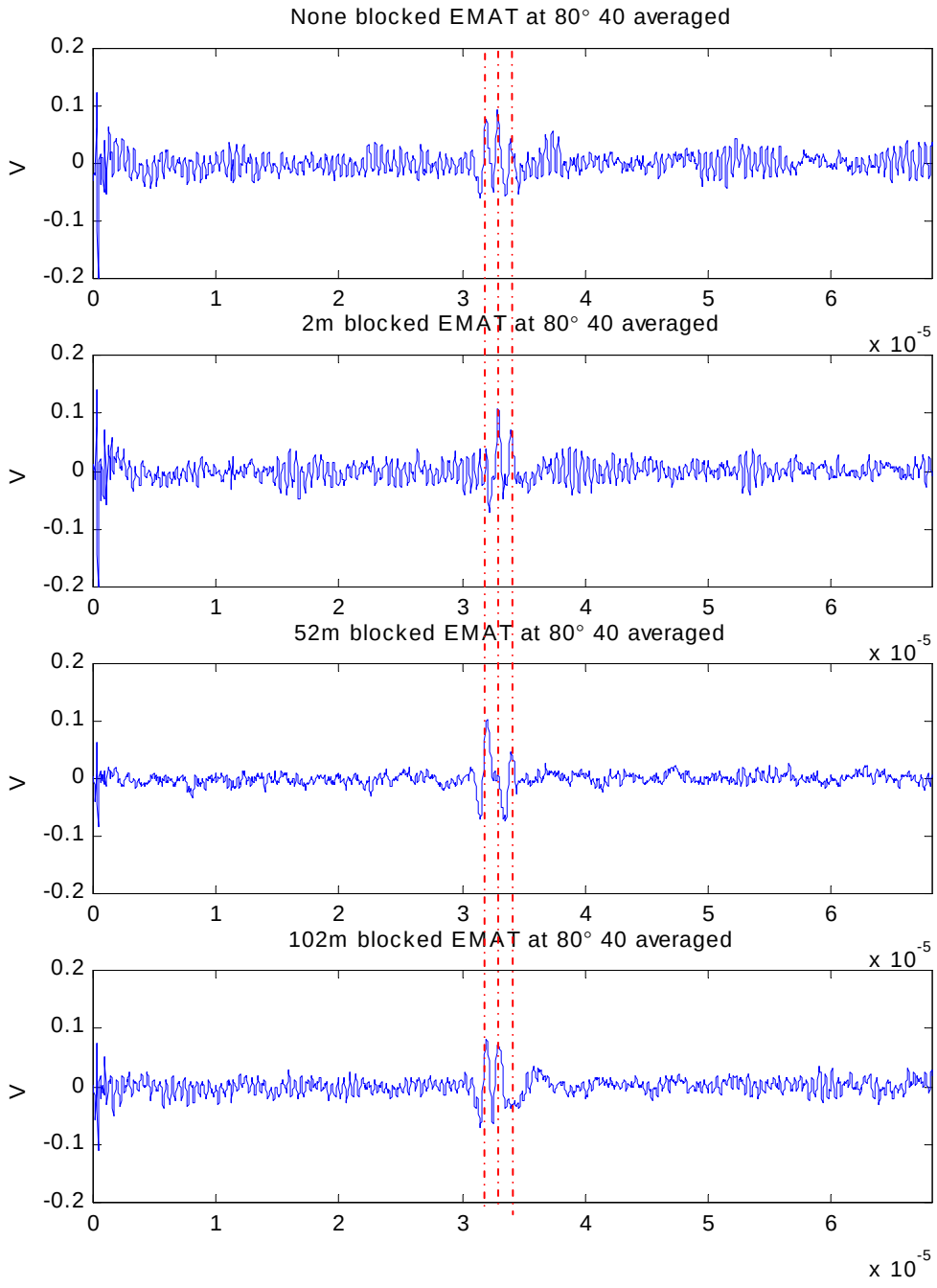

Fig. 5-2 : LURL EMAT signals at -80^{o}

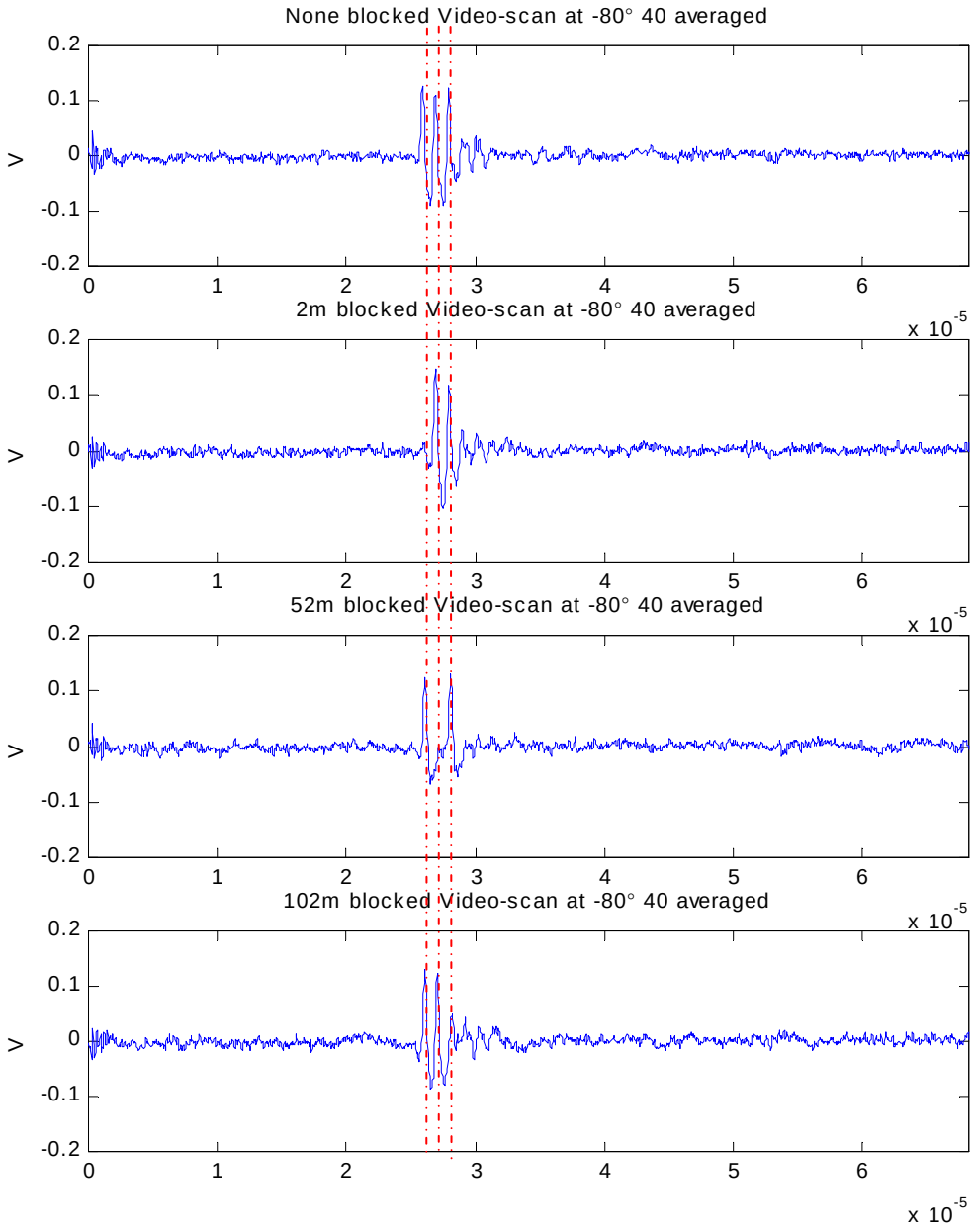

Fig. 5-3 :V153 PZT signals at -80^{o}

5.3. 2.55 mm Laser Phased Array D-spacing With LURL EMAT

Ultrasonic waveforms were obtained from -80^{o} to 80^{o} in 5 degree increments to verify FMLPA for a 2.55 mm d-spacing. The LURL EMAT was used as the receiver. The waveforms obtained were averaged 40 times. Each averaged waveform was continuous wavelet transformed (CWT) using a Morlet wavelet as the mother wavelet. The absolute value of the CWT (abs(CWT) was then taken and a magnitude, time, frequency representation of the original waveform was obtained. The frequency at which the maximum magnitude occurs in each abs(CWT) was taken as the FMLPA of the original waveform.

Experimental FMLPA and theoretical FMLPA are shown in Fig. 5-4 for angles -80^{o} to -55^{o}. From -80^{o} to -55^{o}, the experimental FMLPA from 992 kHz to 1.4 MHz. These frequencies agree with the theoretical FMLPA. The abs(CWT) maximum drops to 240 kHz at -50^{o} and stays below 367 kHz for the remaining angles. At these angles, the FMLPA does not apply or cannot be acquired due to the ultrasound from each seven fiber linear array member interfering with each other.

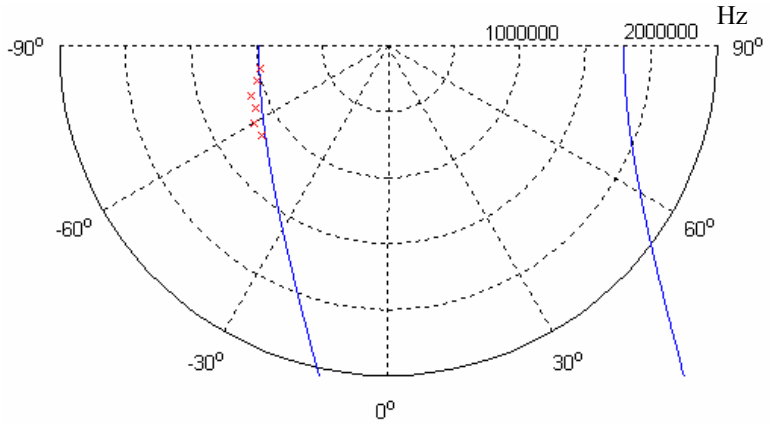

Fig. 5-4 : Theoretical FMLPA (—) and LURL EMAT Experimental Data (x) for 2.55 mm d-spacing

Theoretical and experimental laser phased array directivity pattern for 1 Mhz and 1.3 Mhz is shown in Fig. 5-5 and Fig. 5-6 respectively. Ultrasonic waveforms were obtained from -80^{o} to 80^{o} in 5 degree increments to verify the Array Gain for a 2.55 mm d-spacing. The LURL EMAT was used as the receiver. Obtained waveforms were averaged 40 times. Each averaged waveform was continuous wavelet transformed (CWT) using a Morlet wavelet as the mother wavelet. The maximum magnitude in each abs(CWT) at 1 Mhz and 1.3 Mhz was obtained for each waveform and was used as the experimental directivity pattern of the laser phased array for 1 Mhz and 1.3 Mhz generated ultrasound respectively. Both the theoretical and experimental laser phased array directivity patterns are scaled to 1 at the beam steering angle. The theoretical laser phased array directivity pattern was modified to account for the LURL EMAT's 10^{o} aperture by using a +/-5^{o} moving average.

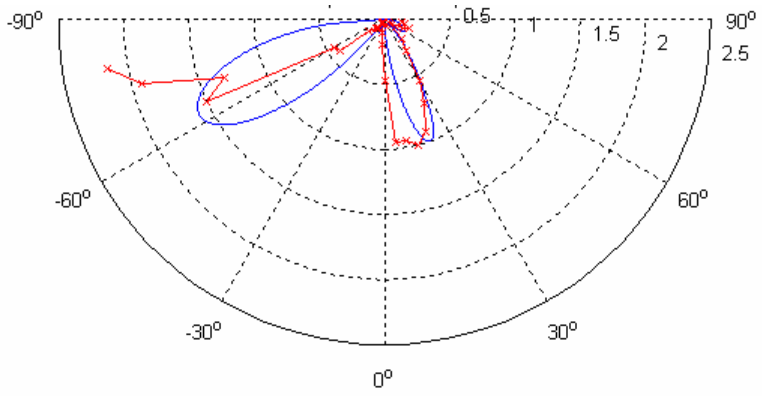

Fig. 5-5 : Theoretical (—) and LURL EMAT Experimental (-x-) Normalized Array Directivity Pattern for 1 Mhz compensated for 10^{o} aperture

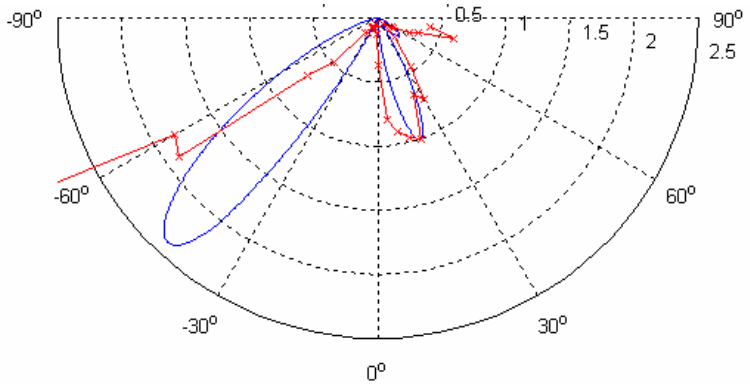

Fig. 5-6 : Theoretical (—) and LURL EMAT Experimental (-x-) Normalized Array Directivity Pattern for 1.3 Mhz compensated for 10^{0} aperture.

A slight error between experimental directivity pattern and theoretical was observed between -50° to 90° where the FMLPA is not valid. These slight errors will be investigated in chapters 5.5-5.7. Angles where the FMLPA is valid show a greater discrepancy. The array gain models indicate that the ultrasound from each seven fiber linear array member destructively interfere at the angles where the FMLPA is valid. Since the FMLPA is valid, the ultrasound from each seven fiber linear array member

does not interfere with each other at all and cannot destructively interfere. The increased amplitude at the angles were the FMLPA is valid is due to the power of the FMLPA and not ultrasound from each seven fiber linear array member interfering with each other. For example, in Fig. 5-4 at 65^{o} the FMLPA frequency is close to 1.3 Mhz. This results in a high amplitude at 65^{o} for the experimental directivity pattern for 1.3 Mhz in Fig. 5-6.

5.4. 2.55 mm Laser Phased Array D-spacing with V153 Video-Scan PZT

The experiment in section 5.3 was repeated using a V153 PZT to validate the results obtained using the LURL EMAT. A comparison between theoretical and experimental FMLPA is shown in Fig. 5-7.From -80^{o} to -65^{o}, the experimental FMLPA ranges from 992 kHz to 1.222 MHz. Once again the experimental FMLPA shows good agreement with the theoretical FMLPA. The abs(CWT) maximum drops to 280 kHz at -60^{o} and stays below 900 kHz for the rest of the angles. At these angles, the FMLPA does not apply or cannot be acquired due to the ultrasound from each seven fiber linear array member interfering with each other or due to the bandwidth of the sensor. The V153 PZT has a narrower bandwidth than the LURL EMAT and cannot acquire as high a FMLPA frequency as the LURL EMAT. However, similar FMLPA results were obtained using the LURL EMAT and V153 PZT sensors between -80^{o} and -65^{o}.

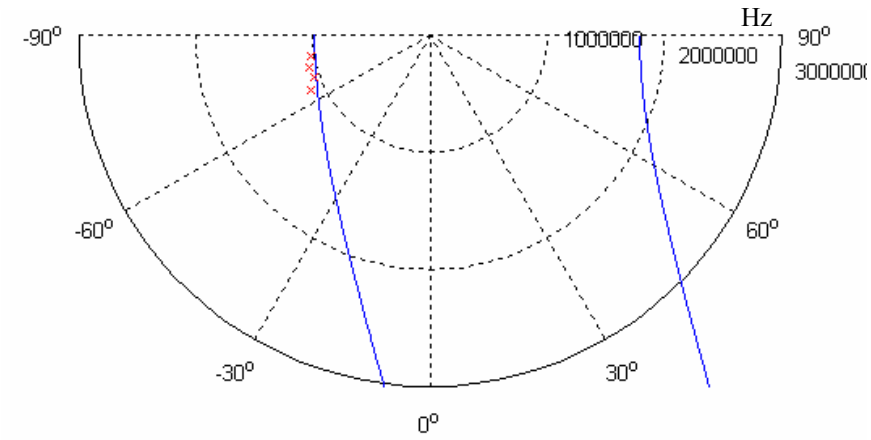

Fig. 5-7 : Theoretical FMLPA (—) and V153 PZT Experimental Data (x) for 2.55 mm d-spacing

Theoretical and experimental laser phased array directivity pattern for 1 Mhz and 1.3 Mhz is shown in Fig. 5-8 and Fig. 5-9 respectively. The experiment was identical to the directivity pattern experiment in chapter 5.3 with the exception that the V153 PZT was used instead of the LURL EMAT.

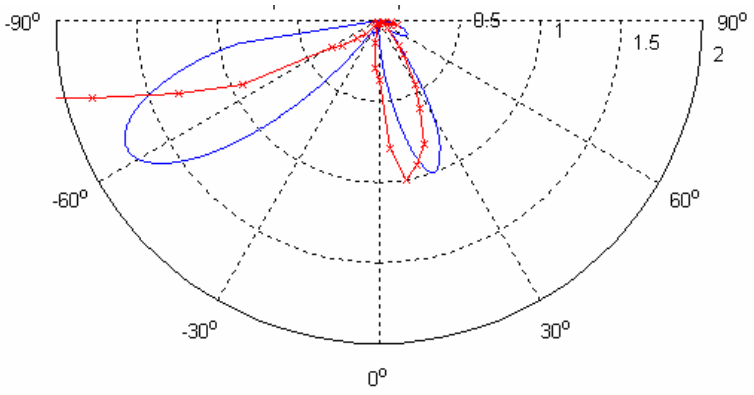

Fig. 5-8 : Theoretical (—) and V153 PZT Experimental (-x-) Normalized Array Directivity Pattern for 1 Mhz compensated for 10^0 aperture.

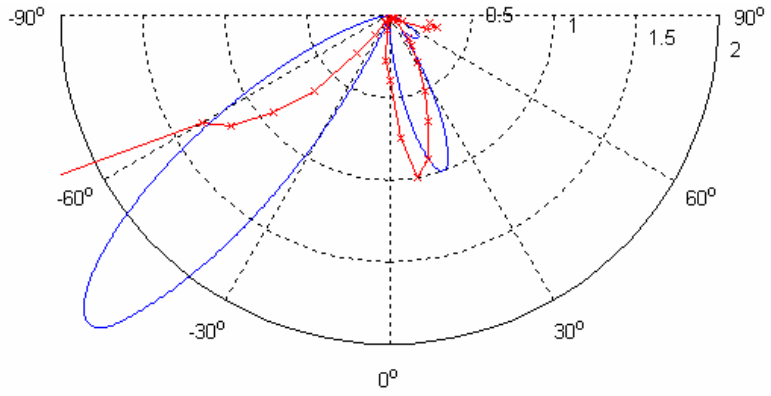

Fig. 5-9 : Theoretical (—) and V153 PZT Experimental (-x-) Normalized Array Directivity Pattern for 1.3 Mhz compensated for 10^0 aperture

Once again, a slight error between the experimental and theoretical laser phased array directivity pattern was observed where the FMLPA is not valid between -60° and 90°. These slight errors will be investigated in chapters 5.5-5.7. Angles where the FMLPA is valid between -80° and -65° show a greater discrepancy due to the same reason given in chapter 5.3. However, this experimental laser phased array directivity patterns obtained using the V153 PZT sensor and LURL EMAT is very similar. Differences between the experimental laser phased array directivity patterns may be due to the sensors' different frequency responses.

5.5. Array Gain for Seven Fiber Linear Array Members and Different Time Delays between Array Members

Array gain equations depend on the time-delays between array members. However, there has been accidental damage to the fibers resulting in different time-delays between array members. The difference in array gain due to different time-delays between array members should be determined to see if it is causing the slight error between experimental and theoretical array gains where the FMLPA is not valid. The previous theoretical plots also assumed each array member was a point source. The difference in array gain for point source array members and seven fiber linear array members should also be determined to see if it is causing the slight error between experimental and theoretical array gains where the FMLPA is not valid. In order to account for the differences, the derivation of array gain equation must be known. The following array gain proof was derived since the derivation is not in literature.

5.5.1. *Array Gain Proof*

The phase shift between two consecutive point source array members due to d-spacing is:

$$ps_d = \frac{2\pi\, d\, sin\,\theta}{\lambda\omega}$$

where :
d *:* d − spacing
θ *: angle* from normal
λ : wave length
ω : frequency

Eq. 5-1

The phase shift between two consecutive point source array members due to time delay is:

$$ps_t = -\frac{2\pi\tau c}{\lambda\omega}$$

Eq. 5-2

where :
τ *:* time delay
c : wave speed (shear or longitudinal)

The total phase shift is:

$$ps = \frac{2\pi d \sin\theta}{\lambda\omega} - \frac{2\pi\tau c}{\lambda\omega}$$

Eq. 5-3

If ϕ is the beam steering angle where the phase shift due to time delay and d-spacing match (0 phase shift angle).

$$\frac{2\pi d \sin\phi}{\lambda\omega} - \frac{2\pi\tau c}{\lambda\omega} = 0 = ps$$
$$\frac{2\pi d \sin\phi}{\lambda\omega} = \frac{2\pi\tau c}{\lambda\omega}$$
$$d \sin\phi = \tau c$$
$$\sin\phi = \frac{\tau c}{d}$$

Eq. 5-4

Then:

$$ps = \frac{2\pi d \sin\theta}{\lambda\omega} - \frac{2\pi d \sin\phi}{\lambda\omega} = \frac{2\pi d(\sin\theta - \sin\phi)}{\lambda\omega}$$

Eq. 5-5

For N member array, the total wave at any point is given by the following due to Huygens Principle:

$$totalwave(t) = f(t-(N-1)ps) + f(t-(N-2)ps).....f(t-ps) + f(t) \qquad \textbf{Eq. 5-6}$$

Vogel defined $q = \omega \cdot ps/2$. In terms of q:

$$totalwave(t) = f(t-\frac{2(N-1)q}{\omega}) + f(t-\frac{2(N-2)q}{\omega}).....f(t-\frac{2q}{\omega}) + f(t) \qquad \textbf{Eq. 5-7}$$

To find the power, the Fourier Transform must be taken:

$$TotalWave(\omega) = F(\omega)e^{j2(N-1)q} + F(\omega)e^{j2(N-2)q} ..... + F(\omega)e^{j2q} + F(\omega)$$
$$TotalWave(\omega) = F(\omega)(e^{j2(N-1)q} + e^{j2(N-2)q} ..... + e^{j2q} + 1) \qquad \textbf{Eq. 5-8}$$

This can be reduced to a geometric series:

$$r = e^{j2q}$$
$$TotalWave(\omega) = F(\omega)(r^{(N-1)} + r^{(N-2)} ....r + 1) = F(\omega)\left(\frac{1-r^N}{1-r}\right) = F(\omega)\left(\frac{1-e^{j2Nq}}{1-e^{2jq}}\right) \qquad \textbf{Eq. 5-9}$$

Then use Euler Identities to find the final Fourier transforms:

$$TotalWave(\omega) = F(\omega)\left(\frac{e^{jNq}\left(e^{-jNq} - e^{+jNq}\right)}{e^{jq}\left(e^{-jq} - e^{+jq}\right)}\right) = F(\omega)e^{j(N-1)q}\left(\frac{\left(e^{jNq} - e^{-jNq}\right)}{\left(e^{jq} - e^{-jq}\right)}\right)$$
$$TotalWave(\omega) = F(\omega)e^{j(N-1)q}\left(\frac{sin(Nq)}{sin(q)}\right) = N\,F(\omega)e^{j(N-1)q}\left(\frac{sin(Nq)}{N\,sin(q)}\right) \qquad \textbf{Eq. 5-10}$$

The power is:

$$TotalMagnitude(\omega) = \left|N\,F(\omega)e^{j(N-1)q}\left(\frac{sin(Nq)}{N\,sin(q)}\right)\right| = \left|N\,F(\omega)\right|\left|\left(\frac{sin(Nq)}{N\,sin(q)}\right)\right| \qquad \textbf{Eq. 5-11}$$

$$TotalPower(\omega) = \left|N\ F(\omega)\right|^2 \left(\frac{sin(Nq)}{N\ sin(q)} \right)^2 \quad \textbf{Eq. 5-12}$$

Therefore the Array Gain is:

$$ArrayGain(\theta,\lambda,\tau,d,N) = \left(\frac{sin(N\,q)}{N\,sin(q)} \right)^2 = I_a(\theta,\lambda,\tau,d,N) \quad \textbf{Eq. 5-13}$$

$\left|N\ F(\omega)\right|^2$ is the sum power from all array members. However for laser generated ultrasound, F(w) depends on θ. This can be factored out:

$$\left|N\ F(\omega)\right|^2 = u_e(\theta)\left|N\ F_2(\omega)\right|^2 \quad \textbf{Eq. 5-14}$$

where :
$u_e(\theta)$ *: directivity pattern of one array element*
$F_2(\omega)$ *: average power of one array element*

The total laser phased array directivity pattern is:

$$u(\theta,\lambda,\tau,d,N) = u_e(\theta) I_a(\theta,\lambda,\tau,d,N) \quad \textbf{Eq. 5-15}$$

Rose's point source model for ablative shear wave generation was used for $u_e(\theta)$ in the previous sections since the ultrasound was ablatively generated.

$$u_e(\theta) = u_S \propto \frac{\sin 2\theta \sqrt{1-\kappa^2 \sin^2\theta}}{\kappa\left(1-2\sin^2\theta\right)^2 + 4\sin^2\theta\sqrt{1-\sin^2\theta}\sqrt{1-\kappa^2\sin^2\theta}} \quad \textbf{Eq. 5-16}$$

where:

$$\kappa = \frac{C_L}{C_S}$$
C_L : *longitudinal wavespeed*
C_S : *shear wavespeed*

By modifying this derivation, the difference in array gain due to unequal time delay between array members and due to point source array members versus seven fiber linear array members can be derived.

5.5.2. *Difference in Array Gain for Different Time Delays Between Array Members*

The time delay from each array member in the experimental setup is not uniform due to accidental breaking of the fibers. The array gain derivation using different time delays between point source array members is as follows:

Phase delay due to d-spacing:

$$ps_d = \frac{2\pi d \sin\theta}{\lambda\omega} \qquad \textbf{Eq. 5-17}$$

where :
d *:* d − spacing
θ *: angle* from normal
λ : wave length

Phase delays due to time delays:

$$ps_{t1} = -\frac{2\pi\tau_1 c}{\lambda\omega} \qquad \textbf{Eq. 5-18}$$

where :
τ_1 *:* time delay from 2m array member to 52m array member
c *:* wave speed (shear or longitudinal)

$$ps_{t2} = -\frac{2\pi\tau_2 c}{\lambda\omega} \qquad \textbf{Eq. 5-19}$$

where :

τ_2 *:* time delay from 52m array member to 102m array member

c : wave speed (shear or longitudinal)

Between 2 m and 52 m point source array members, total phase shift is:

$$ps1 = \frac{2\pi d \sin\theta}{\lambda\omega} - \frac{2\pi\tau_1 c}{\lambda\omega} \qquad \textbf{Eq. 5-20}$$

Since, $\sin\phi_1 = \frac{\tau_1 c}{d}$:

$$ps1 = \frac{2\pi d \sin\theta}{\lambda\omega} - \frac{2\pi d \sin\phi_1}{\lambda\omega} = \frac{2\pi d(\sin\theta - \sin\phi_1)}{\lambda\omega} \qquad \textbf{Eq. 5-21}$$

Similarly between 52 m and 102 m point source array members:

$$\sin\phi_2 = \frac{\tau_2 c}{d} \qquad \textbf{Eq. 5-22}$$

$$ps2 = \frac{2\pi d(\sin\theta - \sin\phi_2)}{\lambda\omega} \qquad \textbf{Eq. 5-23}$$

Using Huygens Principle, the total wave from the three array members is:

$$totalwave(t) = f(t - ps2 - ps1) + f(t - ps1) + f(t) \qquad \textbf{Eq. 5-24}$$

Take the Fourier Transform:

$$\begin{aligned} TotalWave(\omega) &= F(\omega)e^{j\omega(ps1+ps2)} + F(\omega)e^{j\omega ps1} + F(\omega) \\ &= F(\omega)(e^{j(\omega ps2+ps1)} + e^{j\omega ps1} + 1) \end{aligned} \qquad \textbf{Eq. 5-25}$$

Magnitude and power is:

$$TotalMagnitude(\omega) = \left|F(\omega)(e^{j\omega(ps2+ps1)} + e^{j\omega ps1} + 1)\right|$$
$$= \left|3F(\omega)\right|\left|\frac{(e^{j\omega(ps2+ps1)} + e^{j\omega ps1} + 1)}{3}\right| \quad \textbf{Eq. 5-26}$$

$$TotalPower(\omega) = \left|3F(\omega)\right|^2\left|\frac{(e^{j\omega(ps2+ps1)} + e^{j\omega ps1} + 1)}{3}\right|^2 \quad \textbf{Eq. 5-27}$$

Therefore the Array Gain with unequal time delays is:

$$ArrayGain(\theta,\lambda,\tau_1,\tau_2,d) = I_{a\ different\ \tau}(\theta,\lambda,\tau_1,\tau_2,d)$$
$$= \left|\frac{(e^{j(\frac{2\pi d(\sin\theta-\sin\phi_2)}{\lambda}+\frac{2\pi d(\sin\theta-\sin\phi_1)}{\lambda})} + e^{j\frac{2\pi d(\sin\theta-\sin\phi_1)}{\lambda}} + 1)}{3}\right|^2 \quad \textbf{Eq. 5-28}$$

Sum Power from the three array members is $\left|3F(\omega)\right|^2$ but the directivity component must be factored out:

$$\left|3\,F(\omega)\right|^2 = u_e(\theta)\left|3\,F_2(\omega)\right|^2 \quad \textbf{Eq. 5-29}$$

where :
$u_e(\theta)$ *: directivity pattern of array member*
$F_2(\omega)$ *: average power of array member*

The total directivity pattern is:

$$u(\theta,\lambda,\tau,d) = u_e(\theta) I_{a\ different\ \tau}(\theta,\lambda,\tau_1,\tau_2,d)$$
$$= u_S(\theta) I_{a\ different\ \tau}(\theta,\lambda,\tau_1,\tau_2,d) \qquad \textbf{Eq. 5-30}$$

Once again the ablative shear wave generation directivity pattern, $u_S(\theta)$, is used for the directivity pattern of an array member, $u_e(\theta)$, since ultrasound was generated ablatively during the experiments in chapter 5.3 and 5.4.

The measured time delay between the 2 m seven fiber linear array member and 52 m seven fiber linear array member is 2.12×10^{-7} sec. The measured time delay between the 52 m seven fiber linear array member and 102 m seven fiber linear array member is 2.46×10^{-7} sec. Fig. 5-10 shows the array gain using these unequal time delays between point source array members and the array gain using the original averaged time delay of 2.29×10^{-7}s sec between point source array members . It is apparent from Fig. 5-10 the effect of small differences in time delay is very slight since the two array gains mostly overlap one another. The unequal time delays do not explain the differences between experimental and theoretical laser phased array directivity patterns.

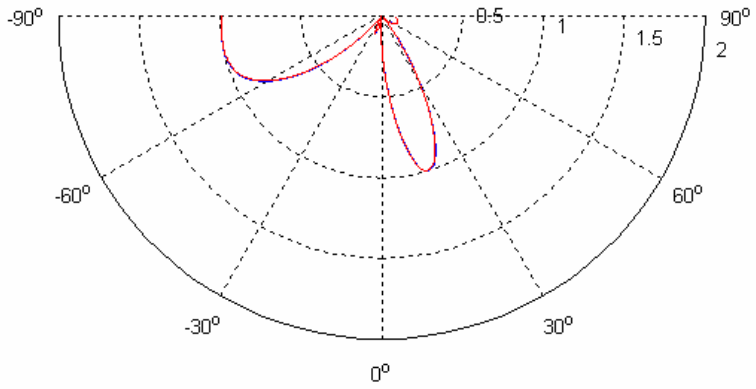

Fig. 5-10 : Theoretical Regular Array Gain (—) with 2.29×10^{-7} sec time delay, and Theoretical Array Gain with different time delays (—) of 2.12×10^{-7} sec and 2.46×10^{-7} sec time delay for steel shear wave at 1 Mhz compensated for 10^{0} aperture

5.5.3. *Difference in Array Gain for Seven Fiber Linear Array Member Versus Point Source Array Members*

The difference in array gain between seven fiber linear array members and point source array members was determined since the difference in time delay between array members did not explain the differences between theoretical and experimental laser phased array directivity patterns. Fig. 5-11 shows the spatial schematic of the seven fiber linear array members and LURL EMAT. *M* is the fiber number within a seven fiber linear array member and *N* is the array member number at each point, $P_{M,N}$.

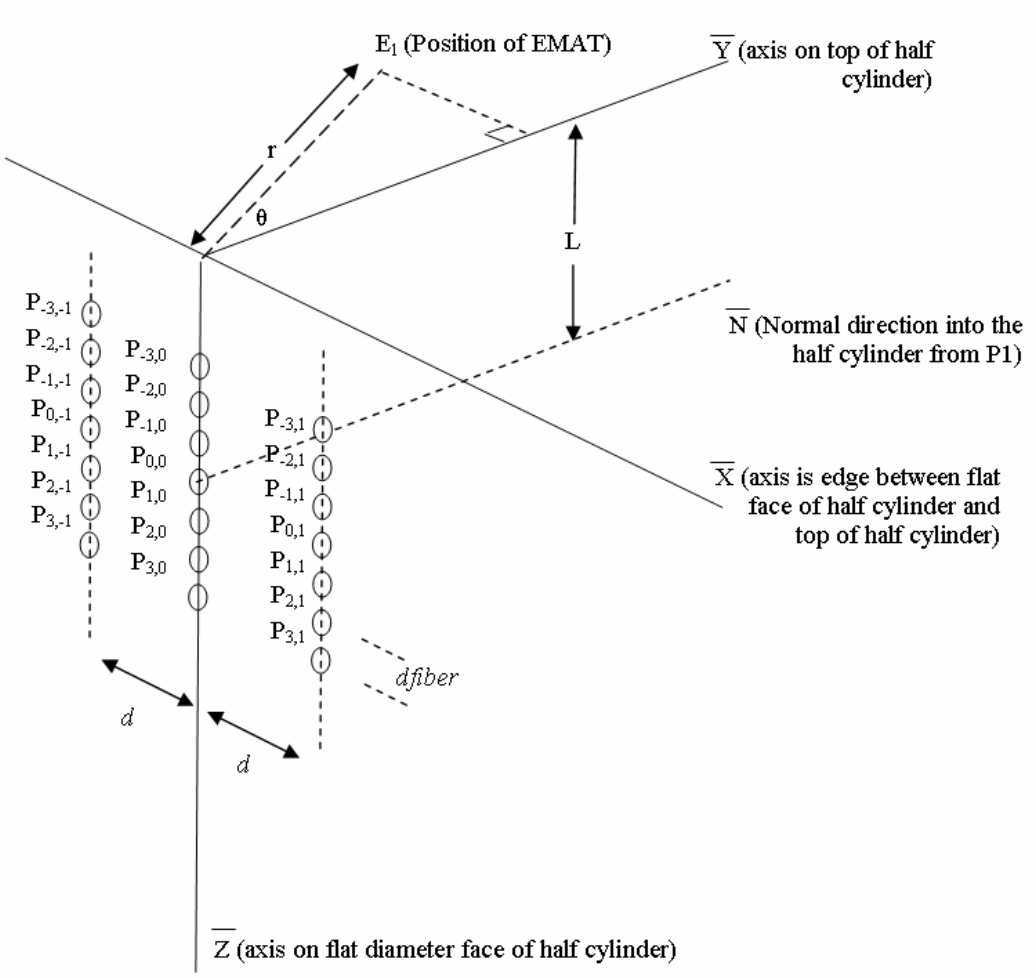

Fig. 5-11 : Schematic of 7 point line source on half cylinder

Using geometry, the distance between any point $P_{M,N}$ to E_1 is:

$$\overline{P_{M,N}E_1} = \sqrt{(r\cos\theta)^2 + (L + M \cdot dfiber)^2 + (r\sin\theta + N \cdot d)^2} \qquad \textbf{Eq. 5-31}$$

The phase shift from any fiber to the fiber at P0,0 due to spatial differences is:

$$ps_d(M,N) = \frac{2\pi\left(\overline{P_{M,N}E_1} - \overline{P_{0,0}E_1}\right)}{\lambda\omega} \qquad \textbf{Eq. 5-32}$$

The phase shift from any fiber to the fiber at $P_{0,0}$ due to time delay, τ, is:

$$ps_t(N) = -\frac{2\pi\tau c \cdot N}{\lambda\omega} \quad \textbf{Eq. 5-33}$$

The total phase shift from any fiber to the fiber at $P_{0,0}$ is :

$$ps\ (M,N) = \frac{2\pi\left(\overline{P_{M,N}E_1} - \overline{P_{0,0}E_1}\right)}{\lambda\omega} - \frac{2\pi\tau c \cdot N}{\lambda\omega} \quad \textbf{Eq. 5-34}$$

Using Huygens Principle, the total wave is:

$$totalwave(t) = \sum_{N=-1}^{1}\sum_{M=-3}^{3} f(t - ps(M,N)) \quad \textbf{Eq. 5-35}$$

The Fourier Transform of the total wave is:

$$\begin{aligned} TotalWave(\omega) &= \sum_{N=-1}^{1}\sum_{M=-3}^{3} F(\omega)(e^{j\omega\, ps(M,N)}) \\ &= F(\omega)\sum_{N=-1}^{1}\sum_{M=-3}^{3}(e^{j\omega\, ps(M,N)}) \end{aligned} \quad \textbf{Eq. 5-36}$$

Then take magnitude and power:

$$TotalMagnitude(\omega) = \left|F(\omega)\right|\left|\sum_{N=-1}^{1}\sum_{M=-3}^{3}(e^{j\omega\, ps(M,N)})\right| \quad \textbf{Eq. 5-37}$$

$$TotalPower(\omega) = \left|21\cdot F(\omega)\right|^2\left|\sum_{N=-1}^{1}\sum_{M=-3}^{3}\frac{(e^{j\omega\, ps(M,N)})}{21}\right|^2 \quad \textbf{Eq. 5-38}$$

Therefore the Array Gain is:

$$ArrayGain(\theta,\lambda,M,N,dfiber,L,r,d) = I_{a\ linearray}(\theta,\lambda,M,N,dfiber,L,r,d)$$

$$= \left| \sum_{N=-1}^{1} \sum_{M=-3}^{3} \frac{(e^{j\omega\ ps(M,N)})}{21} \right|^2$$

$$= \left| \sum_{N=-1}^{1} \sum_{M=-3}^{3} \frac{(e^{j\left\{ \frac{2\pi\left(\overline{P_{M,N}E_1} - \overline{P_{0,0}E_1}\right)}{\lambda} - \frac{2\pi\tau cN}{\lambda} \right\}})}{21} \right|^2 \qquad \textbf{Eq. 5-39}$$

Once again the ablative shear wave generation directivity pattern, $u_S(\theta)$, is used for the directivity pattern of an array member, $u_e(\theta)$, since ultrasound was generated ablatively during the experiments in chapter 5.3 and 5.4.

Fig. 5-12 shows the array gain using point source array members and the array gain using seven fiber linear array members. Difference in array gain between a point source array members and seven fiber linear array members are very slight because both array gains are nearly identical in Fig. 5-12. This does not explain the slight difference between experimental and theoretical directivity patterns.

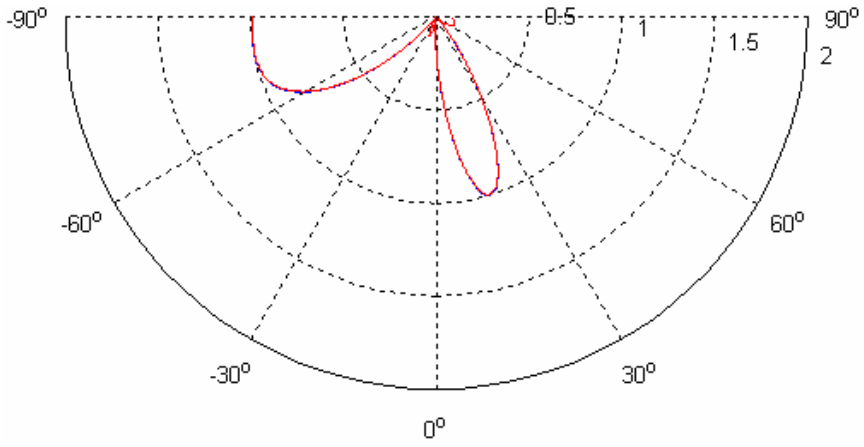

Fig. 5-12 : Theoretical Array Gain (—) with point source array members and Theoretical Array Gain (-x-) with 7 point line sources array members for 1 Mhz compensated for 10^0 aperture

5.6. Directivity of a Single Source

The final factor that may explain the difference between theoretical and experimental array gains is the directivity pattern of a single seven fiber linear array member. The experimental directivity pattern for the 52 m seven fiber linear array member for generated ultrasound at 1 Mhz and 1.3 Mhz was measured using the V153 PZT and are shown in Fig. 5-13 through Fig. 5-14. The experimental directivity pattern for the 52 m seven fiber linear array member for generated ultrasound at 1 Mhz and 1.3 Mhz was also measured using the LURL EMAT and are shown in Fig. 5-15 through Fig. 5-16.

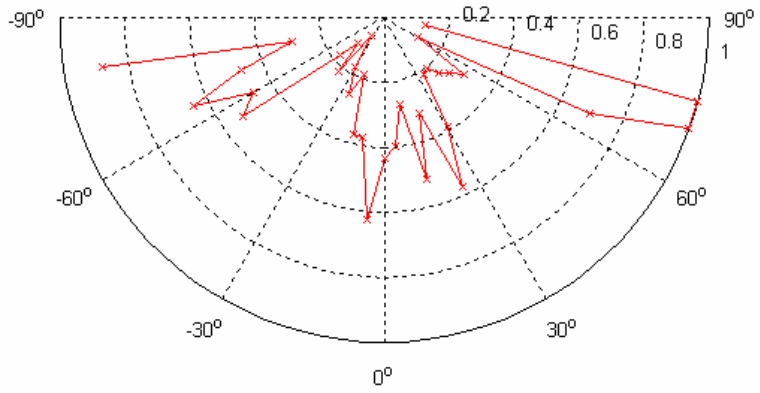

Fig. 5-13 : V153 PZT Experimental Directivity Pattern from the 52 m Seven Fiber Linear Array Member at 1 Mhz

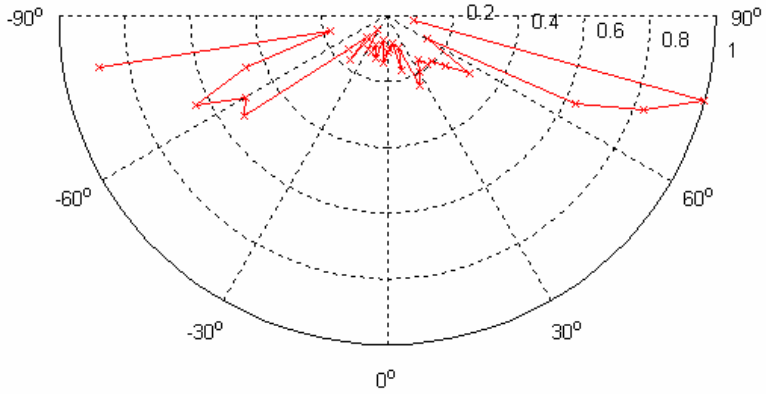

Fig. 5-14 : V153 PZT Experimental Directivity Pattern from Point Source at 1.3 Mhz

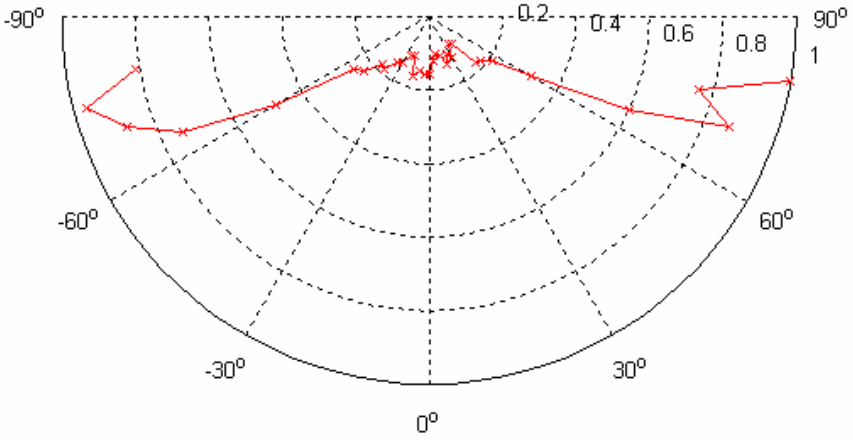

Fig. 5-15 : LURL EMAT Experimental Directivity Pattern from 52 m Seven Fiber Linear Array Member at 1 Mhz

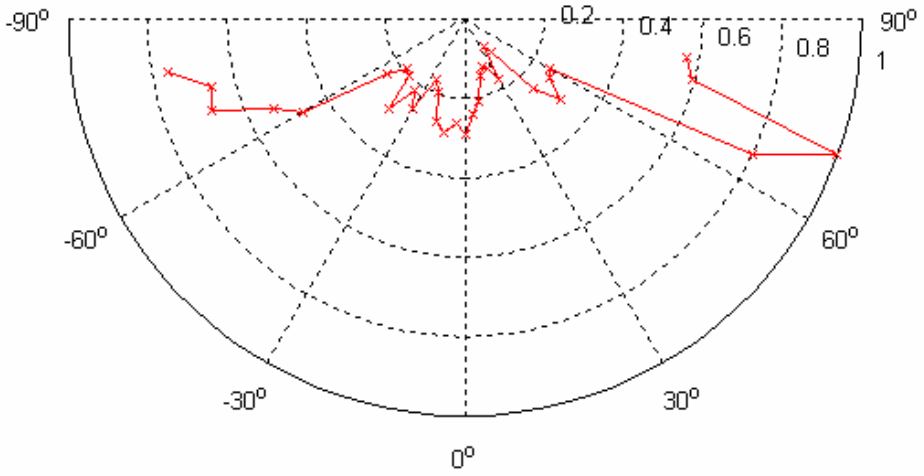

Fig. 5-16 :LURL EMAT Experimental Directivity Pattern from 52 m Seven Fiber Linear Array Member at 1.3 Mhz

These array member directivity patterns do not look like theoretical directivity patterns for ablative shear wave generation from a point source. A scan around the top of the half cylinder was done to better visualize the received waveform and is shown in Fig. 5-17.

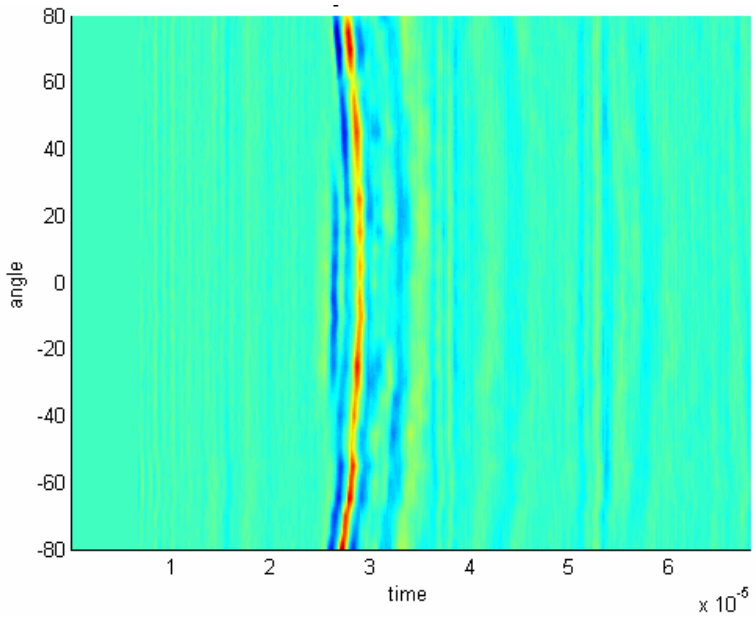

Fig. 5-17 : Top surface scan of half cylinder

The wave-front corresponding to the shear wave is linear at around 2.5×10^{-5} sec. There is another wave-front that varies with the angle following close to the shear wave. In the experimental setup, the only wave-front arrival time that can vary with angle is a surface (Rayleigh) wave as shown in Fig. 5-18.

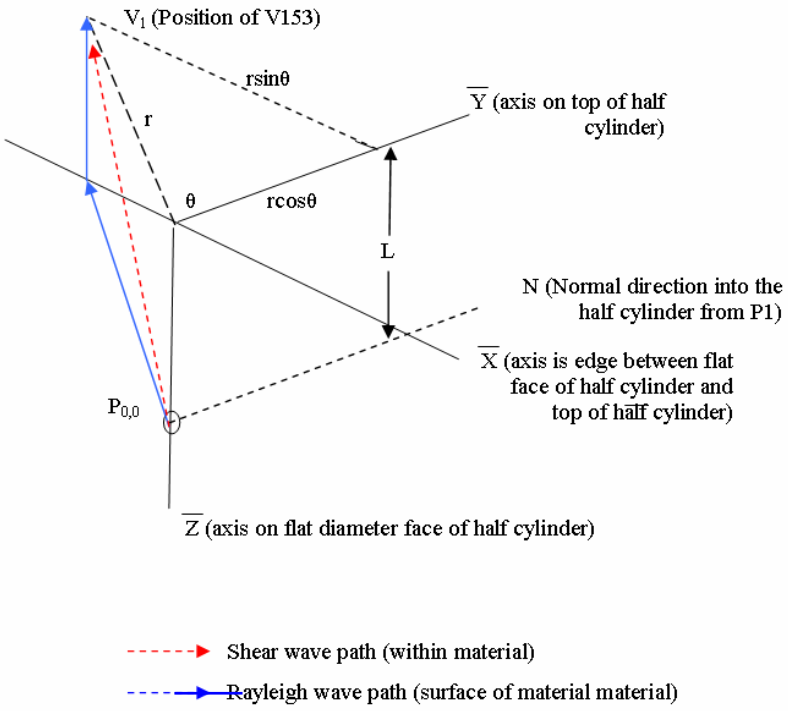

Fig. 5-18 : Schematic of propagation paths from source ($P_{0,0}$) to reception point (V_1)

The path length of the Rayleigh wave varies with θ:

$$path\ length\ Rayliegh\ wave = \sqrt{(r\sin\theta)^2 + (L + r\cos\theta)^2} \qquad \textbf{Eq. 5-40}$$

Path length for the shear wave is constant with respect to θ:

$$path\ length\ shear\ wave = \sqrt{(r)^2 + (L)^2} \qquad \textbf{Eq. 5-41}$$

Arrival times are:

$$\tau_R = \frac{\sqrt{(r\sin\theta)^2 + (L + r\cos\theta)^2}}{C_R} \qquad \textbf{Eq. 5-42}$$

$$\tau_S = \frac{\sqrt{(r)^2 + (L)^2}}{C_s} \qquad \textbf{Eq. 5-43}$$

The results are shown in Fig. 5-19 using: r = .076m, L = .004m, C_s = 3240 m/s, and C_R = 2980 m/s. The previous top surface scan in grayscale is shown as well as the theoretical shear and Rayleigh wave arrival times. There is a laser delay of $1.6\text{x}10^{-6}$ sec.

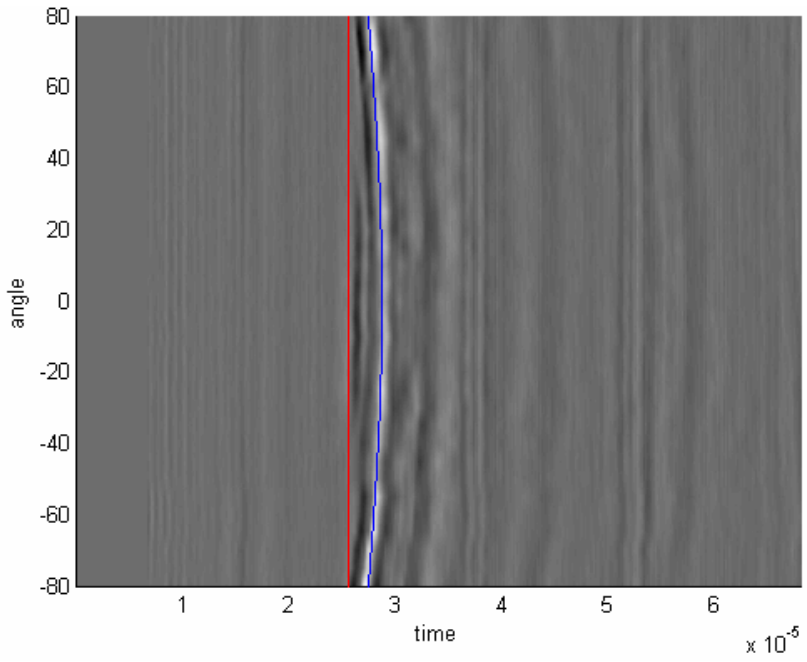

Fig. 5-19 : Top surface scan and Theoretical Arrival Times: Shear (red), Rayleigh (blue)

The reason why the experimental array member directivity pattern for the 52 m seven fiber linear array member does not look like the ablative shear wave directivity from a point source might be the result of the shear and Rayleigh wave interfering with each other. This is highly probable since both waves arrive at the sensor very close together. Array member directivity from shear and surface wave interference from a point source can be calculated. First find the phase shifts:

$$ps_R = \frac{2\pi c_R \tau_R}{\lambda_R w} \quad \textbf{Eq. 5-44}$$

$$ps_S = \frac{2\pi c_S \tau_S}{\lambda_S w} \quad \textbf{Eq. 5-45}$$

Using Huygens Principle, the total wave shear and surface is:

$$totalwave(t) = f_S(t - ps_S) + f_R(t - ps_R) \quad \textbf{Eq. 5-46}$$

Take the Fourier Transform:

$$TotalWave(\omega) = F_S(\omega)e^{j\omega ps_S} + F_R(\omega)e^{j\omega ps_R} \quad \textbf{Eq. 5-47}$$

Then take magnitude and power:

$$TotalMagnitude(\omega) = \left|F_S(\omega)e^{j\omega ps_S} + F_R(\omega)e^{j\omega ps_R}\right| \quad \textbf{Eq. 5-48}$$

$$TotalPower(\omega) = \left|F_S(\omega)e^{j\omega ps_S} + F_R(\omega)e^{j\omega ps_R}\right|^2 \quad \textbf{Eq. 5-49}$$

The surface wave generation does not have an angle dependency but shear wave generation does:

$$F_S(\omega) = u_S(\theta) F_{S2}(\omega) \qquad \textbf{Eq. 5-50}$$

where :
$u_S(\theta)$ *: directivity pattern for generated shearwave*
$F_{S2}(\omega)$ *: average power of generated shearwave*

Therefore:

$$TotalPower(\omega) = \left| u_S(\theta) F_{S2}(\omega) e^{j\omega ps_S} + F_R(\omega) e^{j\omega ps_R} \right|^2 \qquad \textbf{Eq. 5-51}$$

The average power of the shear wave generation and surface wave generation can be written as a ratio to one another.

$$\frac{F_{S2}(\omega)}{F_R(\omega)} = \alpha \qquad \textbf{Eq. 5-52}$$

By substitution:

$$TotalPower(\omega) = \left| \alpha\, u_S(\theta) F_R(\omega) e^{j\omega ps_S} + F_R(\omega) e^{jw ps_R} \right|^2$$

$$TotalPower(w) = \left| F_R(\omega) \right|^2 \left| \alpha\, u_S(\theta) e^{j\omega ps_S} + e^{j\omega ps_R} \right|^2$$

$$TotalPower(\omega) = \left| F_R(\omega) \right|^2 \left| \alpha\, u_S(\theta) e^{j\frac{2\pi c_S \tau_S}{\lambda_S}} + e^{j\frac{2\pi c_R \tau_R}{\lambda_R}} \right|^2 \qquad \textbf{Eq. 5-53}$$

The waveform at 0^0 shown in Fig. 5-20 where shear and surface wave have the greatest time separation can be used to determine α.

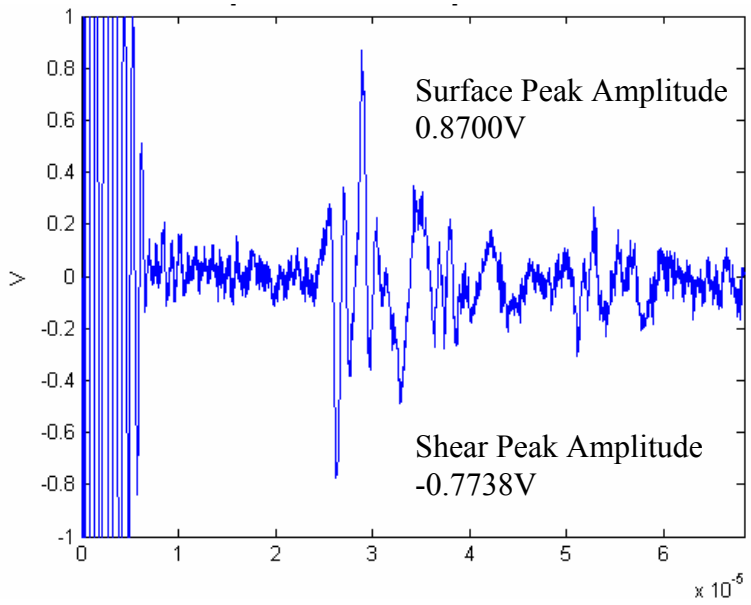

Fig. 5-20 : Waveform at 0° using V153 PZT

Using the peak amplitudes, α = -0.7738/0.8700 = -0.8894. The theoretical and experimental array member directivity patterns when shear and surface waves interfere from a point source for both the V153 PZT and LURL EMAT is shown in Fig. 5-21 thru Fig. 5-24. All theoretical array member directivity patterns have been compensated for an aperture of 10° using a +/- 5° moving average.

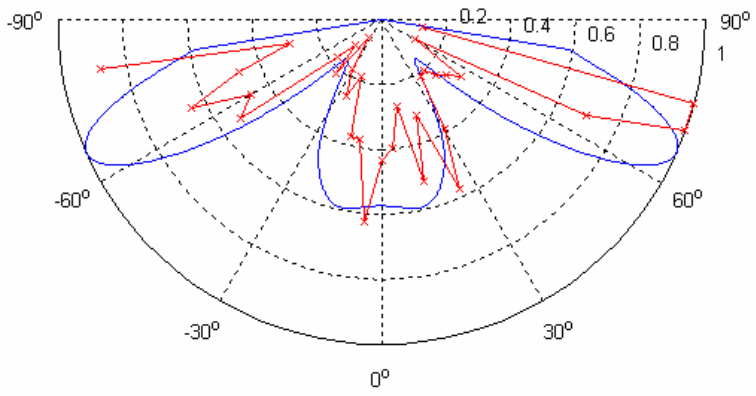

Fig. 5-21 : Theoretical (—) and V153 PZT Experimental (-x-) Directivity Pattern when shear and surface wave fronts interfere from point source at 1 Mhz compensated for an aperture of 10^{o}

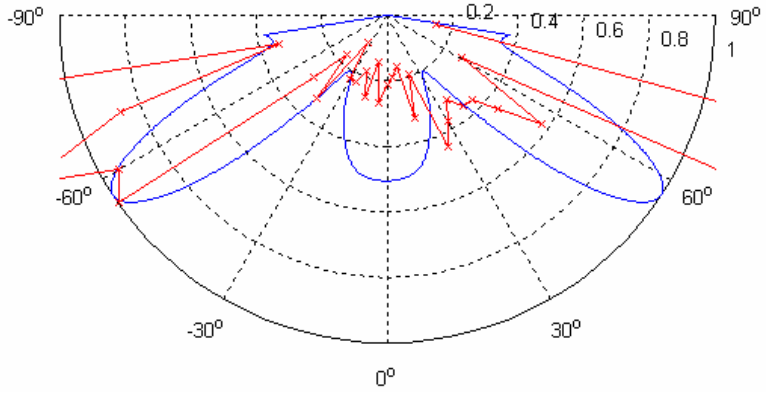

Fig. 5-22 :Theoretical (—) and V153 PZT Experimental (-x-) Directivity Pattern when shear and surface wave fronts interfere from point source at 1.3 Mhz compensated for an aperture of 10^{o}

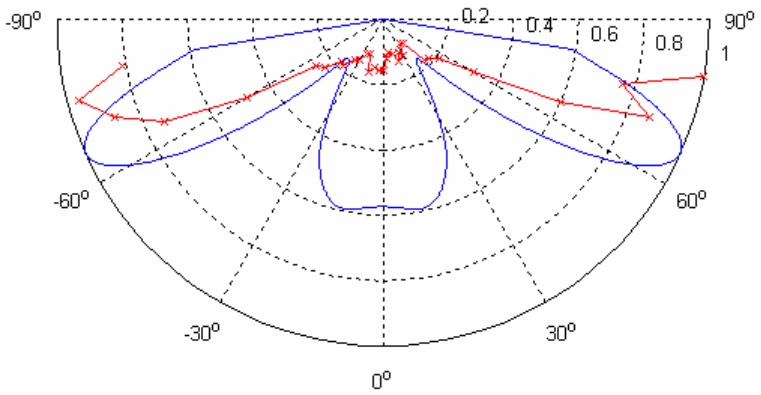

Fig. 5-23 : Theoretical (—) and LURL EMAT Experimental (-x-) Directivity Pattern when shear and surface wave fronts interfere from point source at 1 Mhz compensated for an aperture of 10°

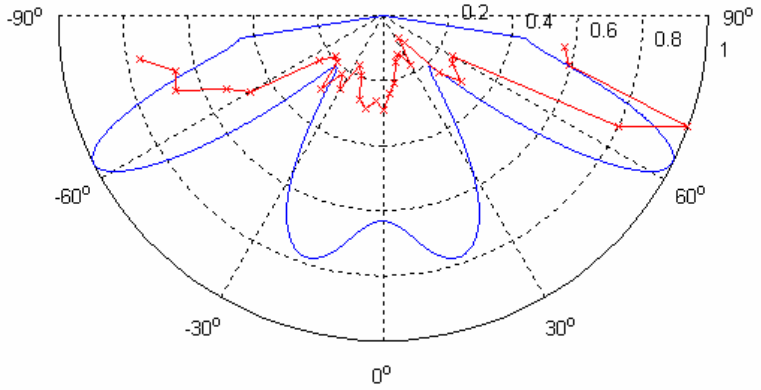

Fig. 5-24 : Theoretical (—) and LURL EMAT Experimental (-x-) Directivity Pattern when shear and surface wave fronts interfere from point source at 1.3 Mhz compensated for an aperture of 10°

The experimental data fits the array member directivity pattern for when shear and surface waves interfere from a point source better than a shear wave from a point source. The match between experimental data and theoretical data is still not exact especially between -30° and 30°. Between -30° and 30° the shear wave and Rayleigh wave fronts have the greatest TOF difference and may not be completely interfering with each other. The theoretical array gain will be the following if this single source directivity pattern is used:

$$u(\theta,\phi)= \left(\frac{\sin(Nq)}{N\sin(q)}\right)^2 \left|\alpha\, u_S(\theta) e^{j\frac{2\pi c_S \tau_S}{\lambda_S}} + e^{j\frac{2\pi c_R \tau_R}{\lambda_R}}\right|^2 \qquad \textbf{Eq. 5-54}$$

Experimental and theoretical laser phased array directivity pattern using the LURL EMAT and the array member directivity pattern for when shear and surface waves interfere from a point source is shown in Fig. 5-25 and Fig. 5-26.

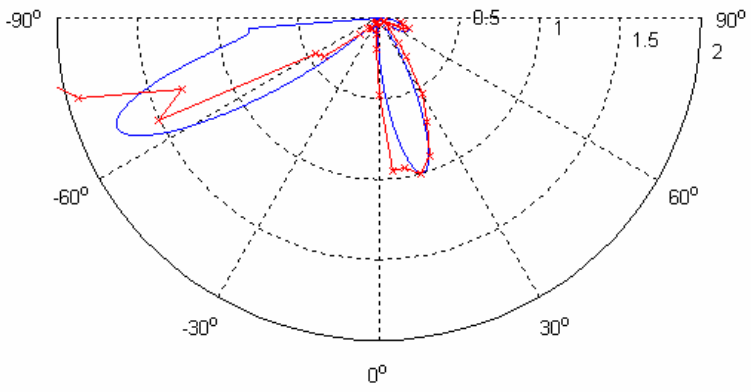

Fig. 5-25 : Theoretical (—) and LURL EMAT Experimental (-x-) Normalized Array Directivity Pattern using shear and surface wave front interference for 1 Mhz compensated for aperture of 10°.

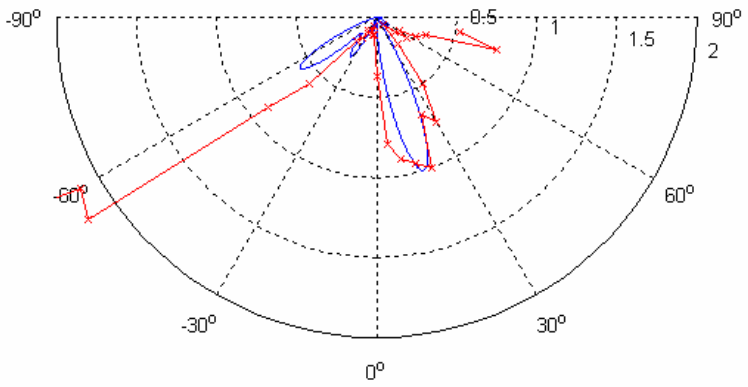

Fig. 5-26 : Theoretical (—) and LURL EMAT Experimental (-x-) Normalized Array Directivity Pattern using shear and surface wave front interference for 1.3 Mhz compensated for aperture of 10°.

Experimental and theoretical laser phased array directivity pattern using the V153 PZT and the array member directivity pattern for when shear and surface waves interfere from a point source is shown in Fig. 5-27 and Fig. 5-28.

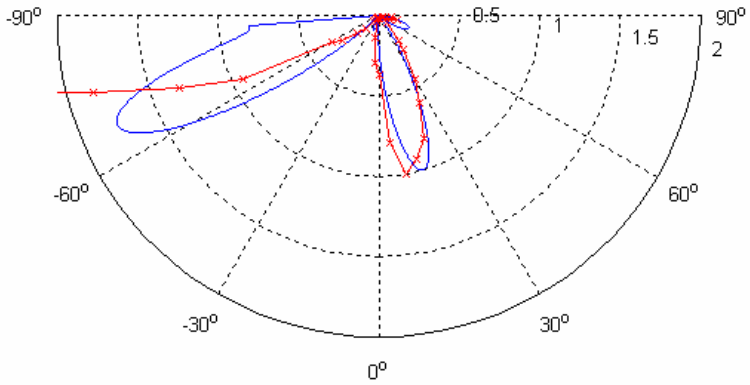

Fig. 5-27 : Theoretical (—) and V153 PZT Experimental (-x-) Normalized Array Directivity Pattern using shear and surface wave front interference for 1 Mhz compensated for aperture of 10°.

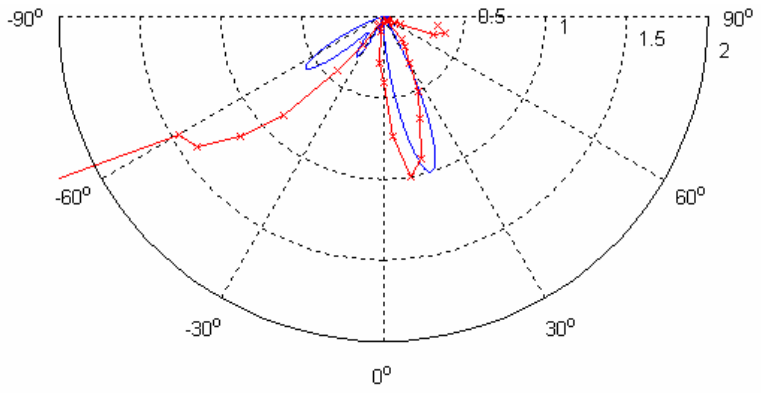

Fig. 5-28 : Theoretical (—) and V153 PZT Experimental (-x-) Normalized Array Directivity Pattern using shear and surface wave front interference for 1.3 Mhz compensated for aperture of 10^{o}.

It can be seen that the experimental and theoretical laser phased array directivity patterns match better using the point source array member directivity pattern for when shear and surface waves interfere. This also shows that the directivity pattern from each array member can be comprised of different types of waves. The types of waves that the sensor can receive and when the waves arrive at the sensor is therefore an important parameter when adjusting a laser phased array.

5.7. Discussion of FMLPA and Array Gain Results

The data presented in this chapter showed that the FMLPA and array gain equations both apply to laser phased arrays. The FMLPA is valid for angles where the ultrasound from each array member does not interfere with each other. The array gain equations still apply for angles where ultrasound from each array member does interfere with each other. Since the array gain equations do not apply where the FMLPA is valid, the laser array should not be configured using only the array gain equations. The array gain equations

may indicate that ultrasound from the array destructively interferes at certain angles but if the FMLPA is valid in these angles, the ultrasound from the array may not destructively interfere. This can lead to unexpected ultrasonic waves appearing in data. The fact that laser ultrasound generation is capable of generating all types of ultrasonic waves should also be taken into account when configuring a laser phased array.

The array gain derivation shown in this chapter has proven to be very useful. Array gains for different array configurations such as arrays using seven fiber linear array members and unequal time delays between array members were obtainable with modifications to the original array gain derivations. The array gain derivations also show that the array gain was derived with the assumption that ultrasound from each array member will always interfere with each other.

The existence of the FMLPA means that it can be used to measure weld penetration depth. However , the unexpected result that both the EMAT and PZT observed a shear and Rayleigh wave interfering with each other from an array member indicates that more basic research should be done before using the FMLPA to measure weld penetration depth. If the FMLPA is going to be used to measure weld penetration depth, the types of ultrasonic waves the EMAT or PZT receives and the path of the ultrasonic waves between the generation and reception point on a weld sample needs to be determined first. This will help determine the correct configuration and placement of the laser phased array need to measure weld penetration depth using the FMLPA.

Chapter 6

Observable Ultrasonic Waves using EMAT and Piezo Sensors

The array can be adjusted so that the shear waves reflecting from the bottom of the weld bead does not interfere with any other wave if the types of ultrasonic waves the EMAT and PZT receive is determined and the propagation path of the ultrasonic wave is known. This will enable accurate weld penetration depth measurements using the FMLPA. This section of research will use the following sensors: Navy EMAT, LURL EMAT, and Panametrics Videoscan V153 PZT. Ultrasonic waves will be created using a single laser point source in a flat plate. The signal received by the various sensors will be analyzed to determine which ultrasonic waves are acquired and what paths the ultrasonic waves traveled between generation and reception points. The experimental setup is shown in Fig. 6-1. The thickness, *T*, of the sample is .0258 m. The distance, *D*, between source and receiver will be varied. Ultrasound is generated using a single point source from Laser Photonics Laser.

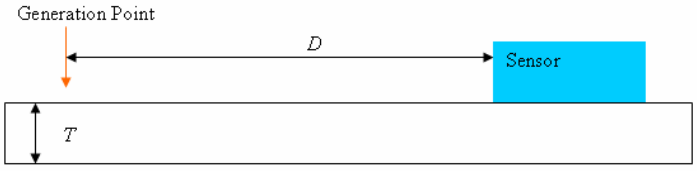

Fig. 6-1 : Experimental Setup for determining what types of ultrasonic waves sensors can observe

A set of signals when D = 0.25 m is shown in Fig. 6-2. All three sensors receive similar waveforms but the LURL EMAT sensor exhibits the least amount of chirp and has highest bandwidth.

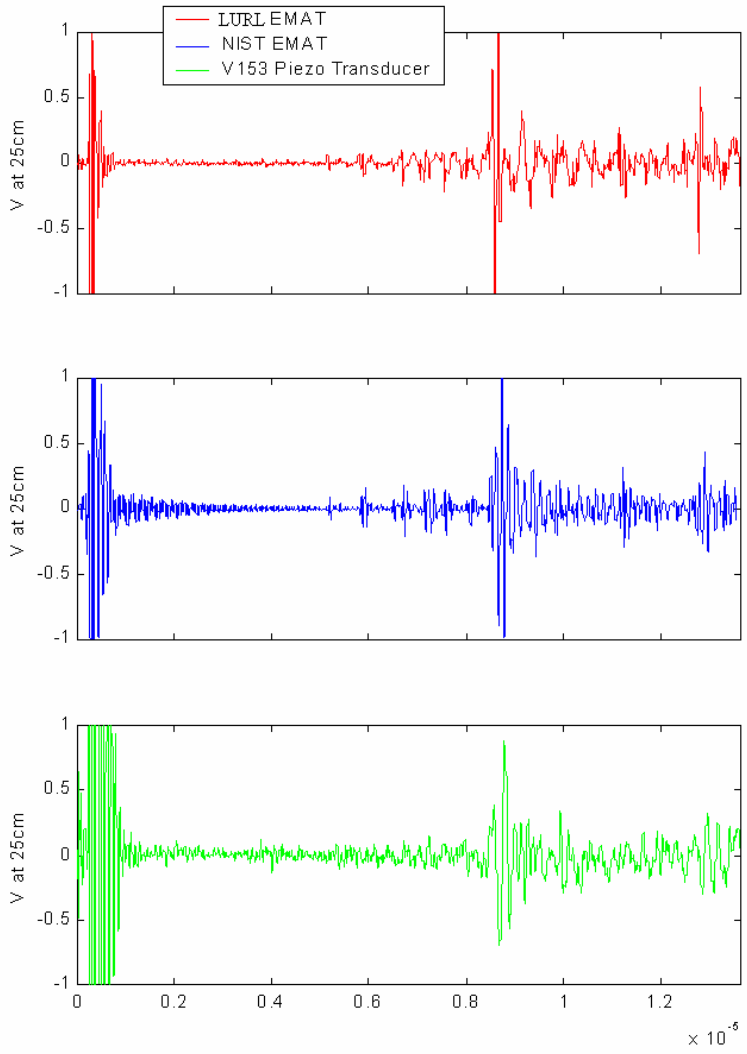

Fig. 6-2 : Example Signals From Various Sensors

An example set of signals for various D is shown in Fig. 6-3. Signals from each sensor is overlaid on top of one another.

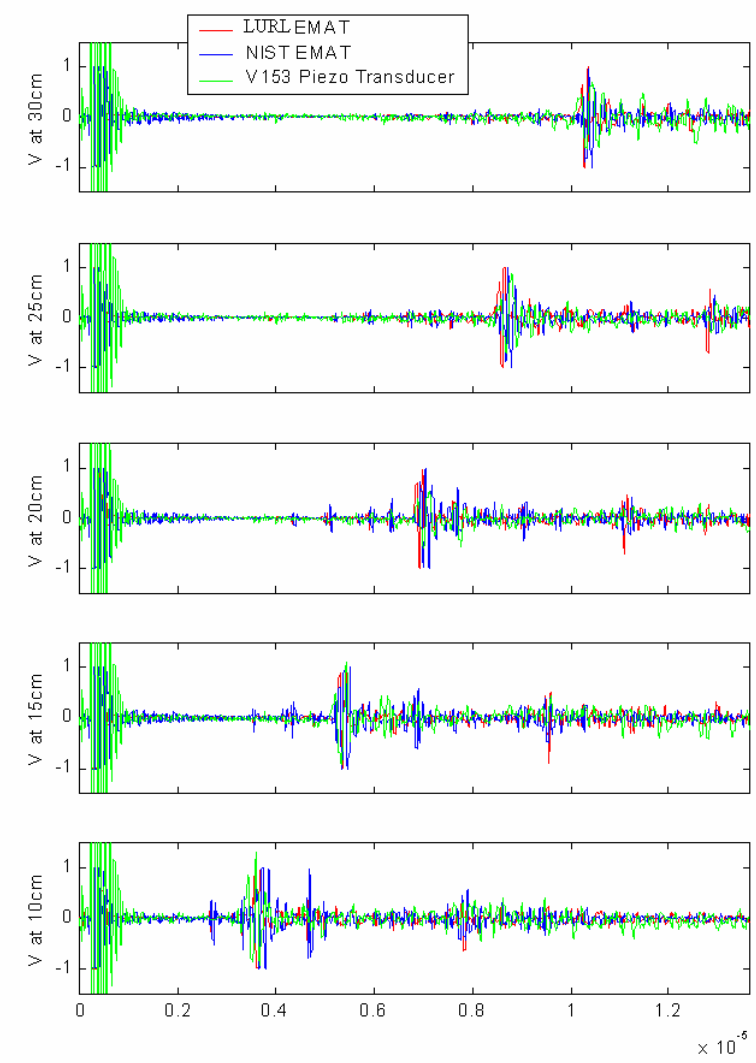

Fig. 6-3 : Example Signals for different D

Data for all three sensors was converted into a 3D (*D*, time, and amplitude) representation and is shown in Fig. 6-4 thru Fig. 6-6.

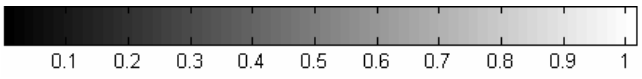

Volts

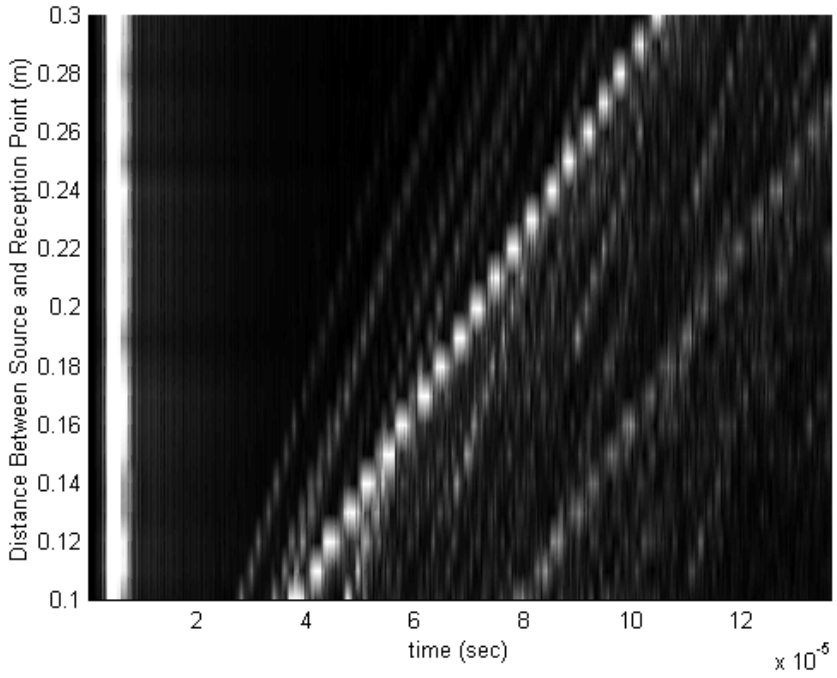

Fig. 6-4 : Navy EMAT Data

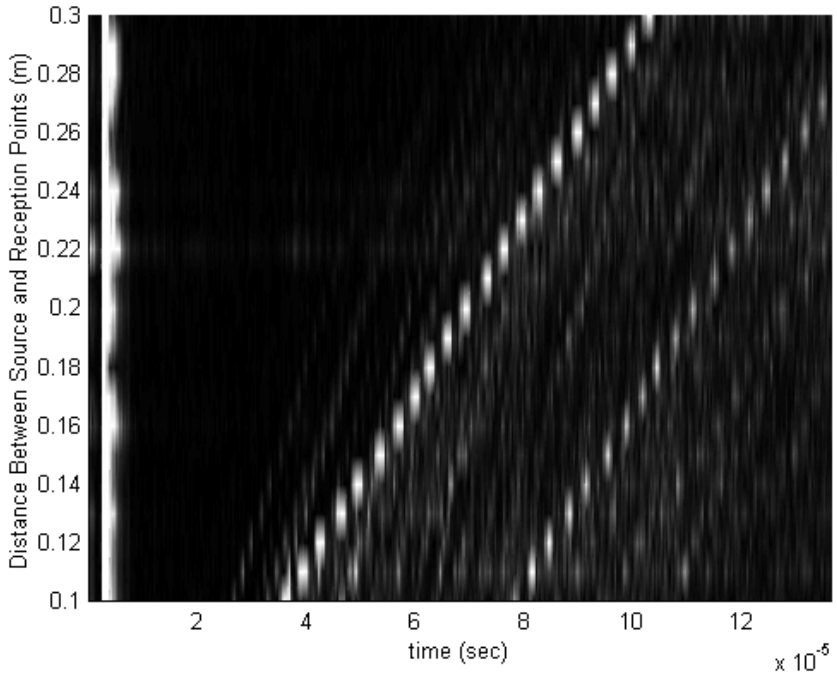

Fig. 6-5 : LURL EMAT data

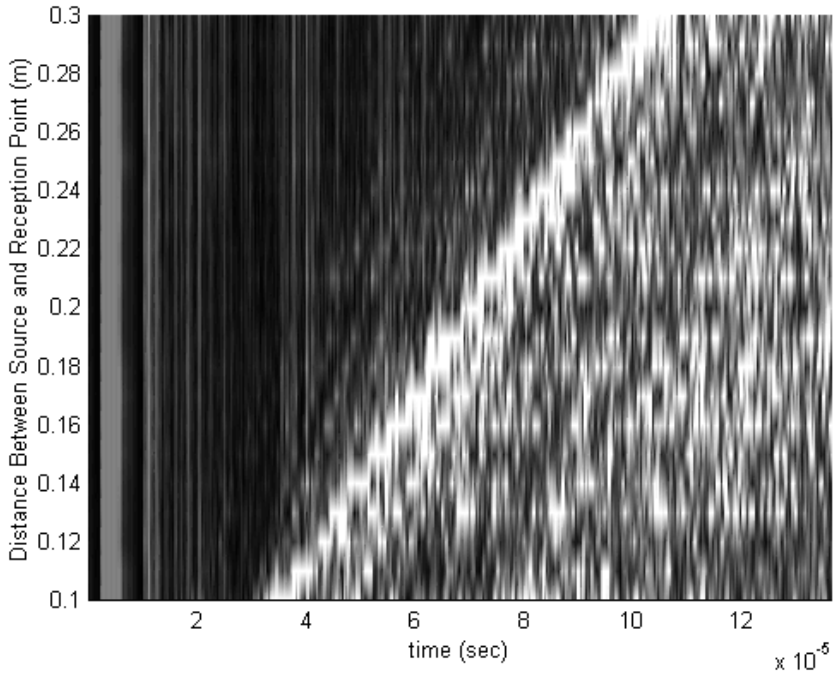

Fig. 6-6 : V153 PZT Data

In Fig. 6-4 thru Fig. 6-6, the white diagonal lines within each data set is a ultrasonic wave front. The slopes and locations of ultrasonic wave fronts vary because each ultrasonic wave's propagation path has a different dependence on *D*. Theoretical TOF of different ultrasonic waves were overlaid on top of experimental data to see which waves were observable. The following ultrasonic waves were detectable:

1. Rayleigh (Surface Waves)

   The detected Rayleigh wave traveled on the top surface directly from the generation point to the sensor as shown in Fig. 6-7. The TOF of the Rayleigh wave, TOF_R , is given by Eq. 6-1.

$$TOF_R = D / C_R$$ **Eq. 6-1**

C_R .: Speed of Rayliegh Wave in Steel

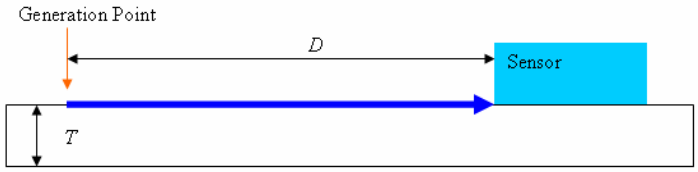

Fig. 6-7 : Rayleigh Propagation Path

2. Shear

The detected shear wave travels from the generation point to the bottom surface of the plate as a shear. From the bottom surface of the plate, the shear wave reflects back up to the sensor as shown in Fig. 6-8. The TOF for the shear wave, TOF_S, is given by Eq. 6-2 .

$$TOF_S = \frac{\sqrt{D^2 + (2T)^2}}{C_S}$$ **Eq. 6-2**

C_S .: Speed of Shear Wave in Steel

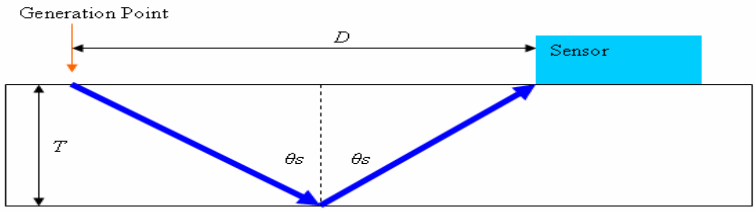

Fig. 6-8 : Shear Propagation Path

3. LS Mode converted waves.

A longitudinal wave travels from the generation point to the bottom surface of the plate. From the bottom surface, the longitudinal wave mode converts and reflects back up to the sensor as a shear wave as shown in Fig. 6-9. This wave path will be referred to as the LS Mode converted wave. Since the wave mode converts from a longitudinal to shear wave, the reflection angles, θ_S and θ_L , are not equal and must be determined before the TOF can be calculated. Eq. 6-3 and Eq. 6-4 must be iterated to find θ_S and θ_L . Then TOF of the LS Mode converted wave , TOF_{LS}, may be calculated using Eq. 6-5.

$$\frac{sin(\theta_s)}{C_s} = \frac{sin(\theta_l)}{C_l} \qquad \textbf{Eq. 6-3}$$

$$D = T\left(tan(\theta_s) + tan(\theta_l)\right) \qquad \textbf{Eq. 6-4}$$

$$TOF_{LS} = \frac{T}{C_s\, cos(\theta_s)} + \frac{T}{C_l\, cos(\theta_l)} \qquad \textbf{Eq. 6-5}$$

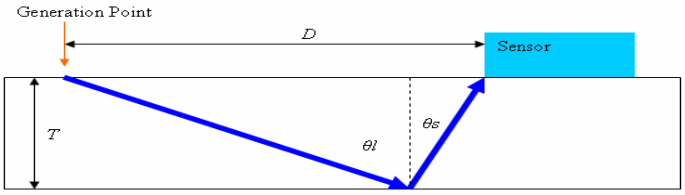

Fig. 6-9 : LS mode converted wave propagation path

4. L(M)S(N)R_LS Mode converted wave

This is a special case of the LS Mode converted wave. A generated shear or longitudinal wave from the generation point can reflect back and forth between the top and bottom surface. At each reflection, the shear or longitudinal wave generates both a shear and longitudinal wave reflection. Every time a shear or longitudinal wave reflects from the top surface, a portion of the energy will become a LS Mode converted wave as shown in Fig. 6-10. Fig. 6-10 is a little confusing because it is showing only the propagation path. It seems like the bouncing shear or longitudinal wave is suddenly veering off to become the LS Mode converted wave; however, ultrasonic wave fronts are really hemispherical and each reflection is hemispherical. This wave propagation path will be referred to as the L(M)S(N)R_LS Mode converted wave where *M* is the number of reflections as a longitudinal wave and *N* is the number of reflections as a shear wave. The TOF the L(M)S(N)R_LS mode converted wave, $TOF_{L(M)S(N)R\_LS}$, is given by Eq. 6-6.

$$TOF_{L(M)S(N)} = \frac{T \cdot M}{C_L} + \frac{T \cdot N}{C_S} + TOF_{LS} \qquad \textbf{Eq. 6-6}$$

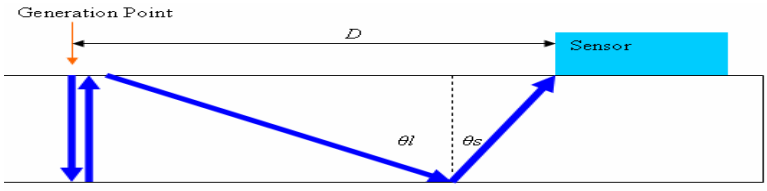

Fig. 6-10 : L(M)S(N)R_LS Mode converted wave propagation path

Theoretical TOF of the observable ultrasonic wave types were overlaid on top of experimental data for LURL EMAT, Navy EMAT, and V153 PZT and are shown in Fig. 6-11 thru Fig. 6-16.

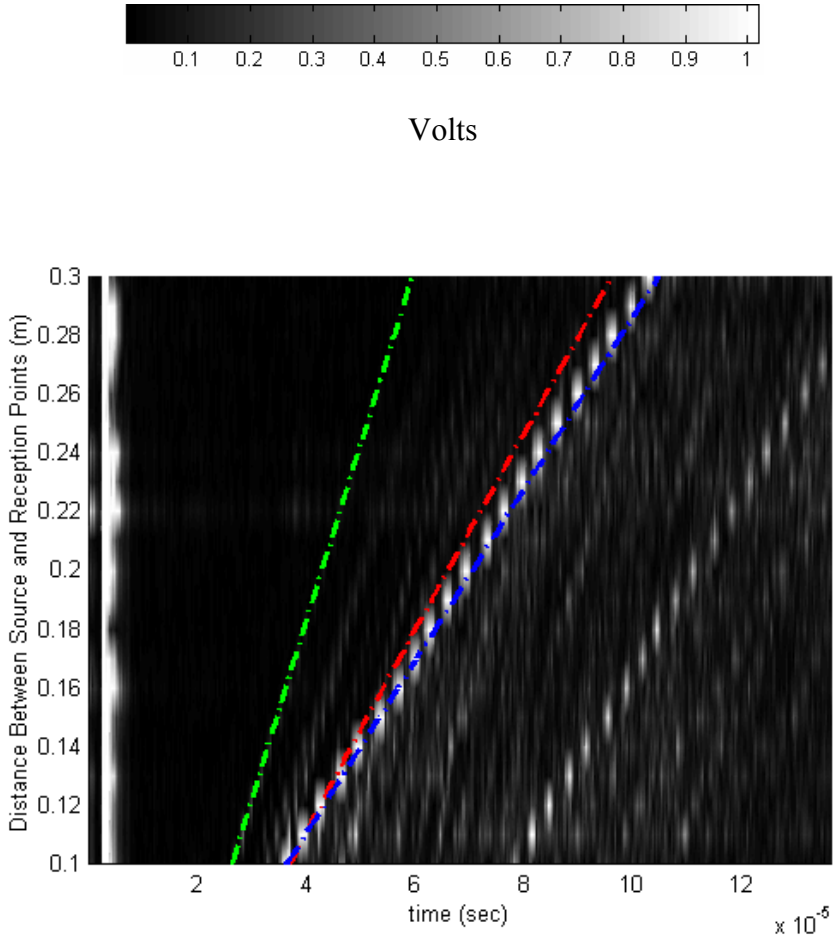

Fig. 6-11 : LURL EMAT "distance" B-Scan with TOF_R (Blue), TOF_S (Red), and TOF_{LS} (Green)

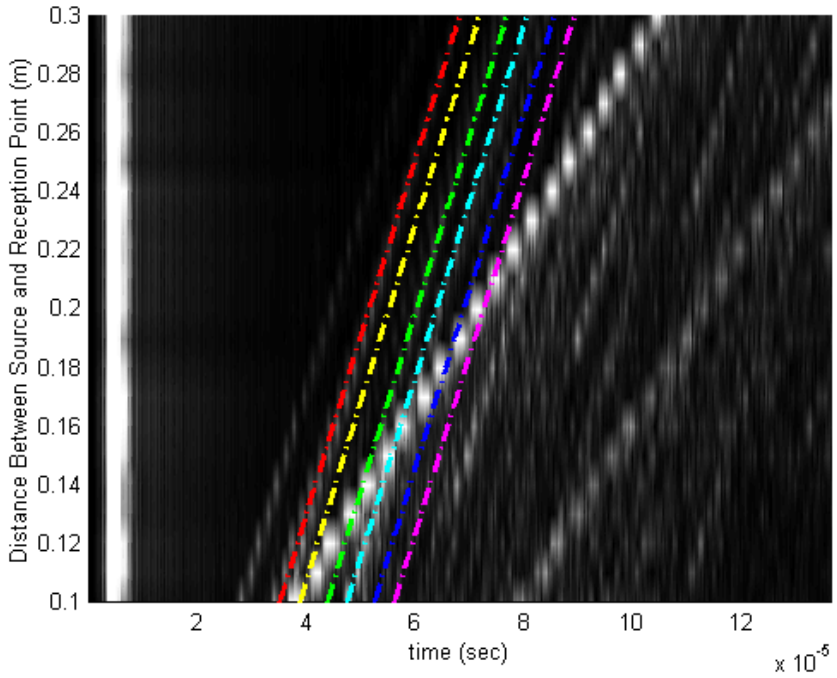

Fig. 6-12 : LURL EMAT "distance" B-Scan with TOF_{L2S0R_LS} (Red), TOF_{L1S1R_LS} (Yellow), TOF_{L4S0R_LS} (Green), TOF_{L3S1R_LS} (Cyan), TOF_{L6S0R_LS} (Blue), and TOF_{L5S1R_LS} (Magenta)

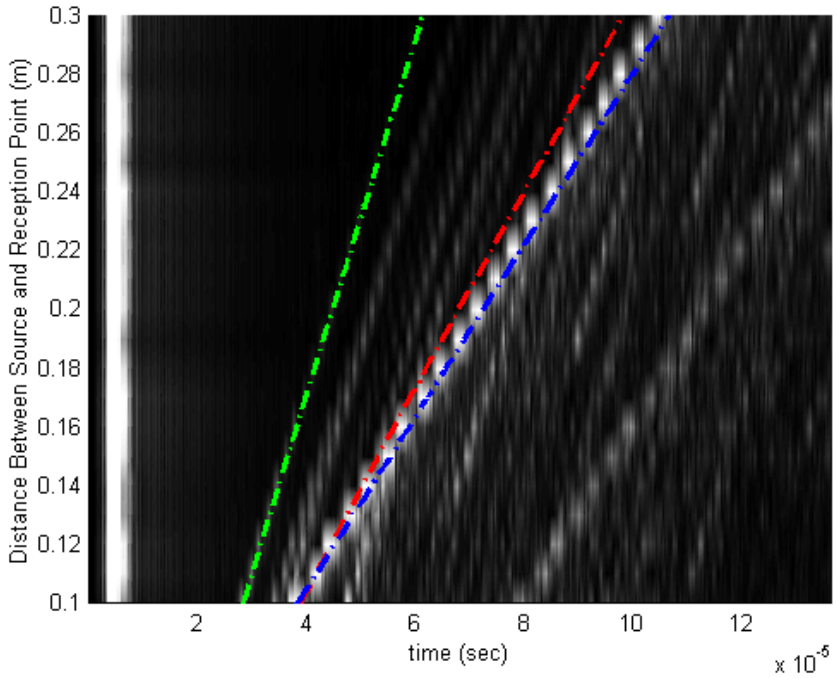

Fig. 6-13 : Navy EMAT "distance" B-Scan with TOF_R (Blue), TOF_S (Red), and TOF_{LS} (Green)

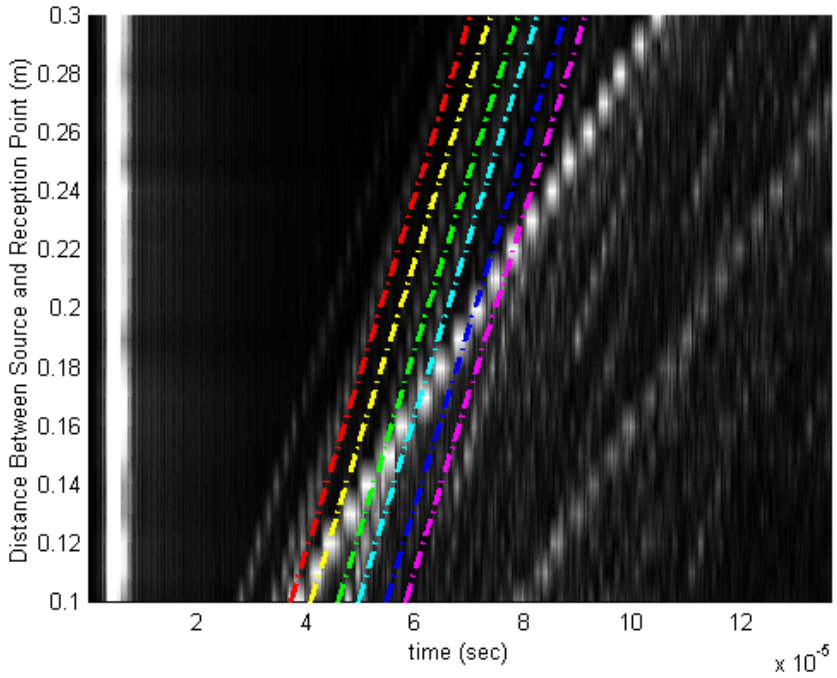

Fig. 6-14 : Navy EMAT "distance" B-Scan with TOF_{L2S0R_LS} (Red), TOF_{L1S1R_LS} (Yellow), TOF_{L4S0R_LS} (Green), TOF_{L3S1R_LS} (Cyan), TOF_{L6S0R_LS} (Blue), and TOF_{L5S1R_LS} (Magenta)

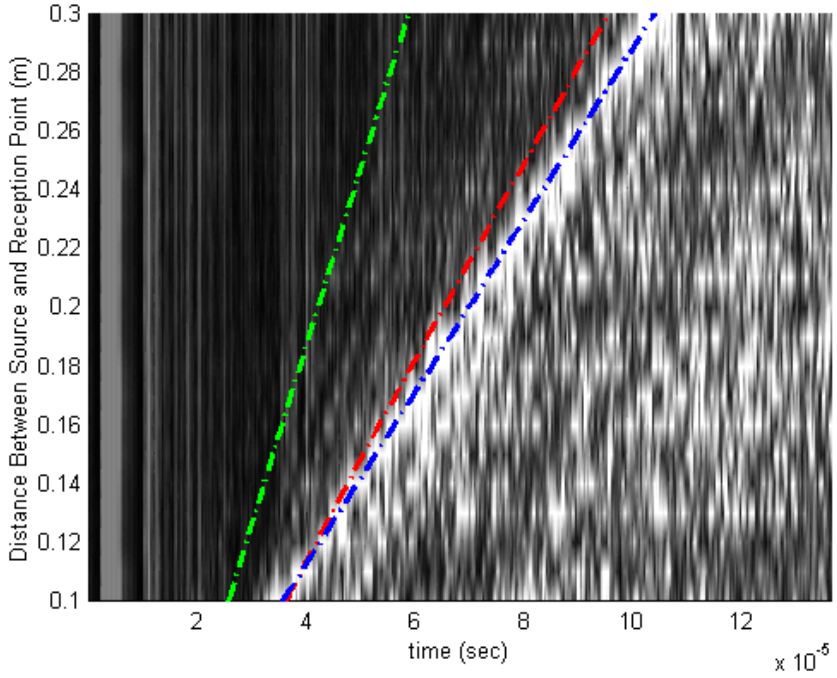

Fig. 6-15 : V153 PZT "distance" B-Scan with TOF_R (Blue), TOF_S (Red), and TOF_{LS} (Green)

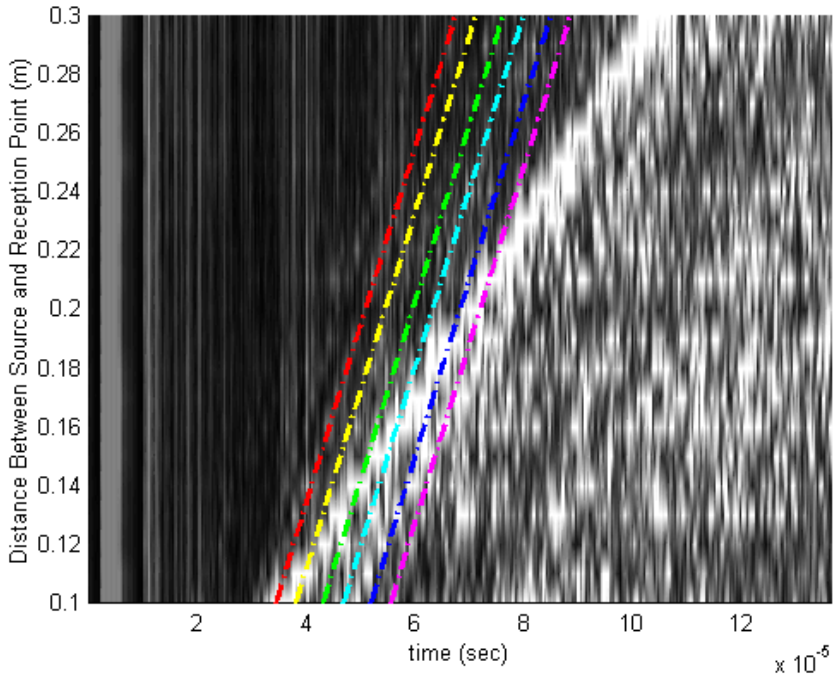

Fig. 6-16 : V153 PZT "distance" B-Scan with TOF_{L2S0R_LS} (Red), TOF_{L1S1R_LS} (Yellow), TOF_{L4S0R_LS} (Green), TOF_{L3S1R_LS} (Cyan), TOF_{L6S0R_LS} (Blue), and TOF_{L5S1R_LS} (Magenta)

It is apparent that the LURL EMAT, NAVY EMAT, and V153 PZT can acquire Rayleigh, shear, LS mode, and L(M)S(N)R_LS mode waves since the wave fronts of these waves match well with experimental data.

6.1. Simulation of Ultrasonic Propagation though a Weld bead

Simulation of ultrasonic waves acquired by a sensor during welding can be obtained if the theoretical TOF equations are modified to account for the weld. Shear wave will be deflected from bottom of weld bead and the modified TOF_S equation is shown in Eq. 6-7. Eq. 6-7 only applies if the ultrasound generation and reception points are equidistant from the weld seam. Rayleigh wave will travel over the weld reinforcement and the

modified TOF_L equation is shown in Eq. 6-8 . The weld reinforcement is assumed to be a half cylinder in Eq. 6-8. LS and L(M)S(N)R_LS modes cannot propagate if penetration depth is not deep enough because it is reflected back towards the generation point by the weld seam. This condition is shown in Eq. 6-9.

$$TOF_S = \frac{\sqrt{D^2 + (2d_{penetration})^2}}{C_S} \quad \textbf{Eq. 6-7}$$

where:

C_S : Speed of shear wave in steel

D : Distance between generation and reception points

$d_{penetration}$: Penetration depth

$$TOF_R = (D + H_{reinforcement}\pi - 2 \cdot H_{reinforcement}) / C_R \quad \textbf{Eq. 6-8}$$

where:

C_R : Speed of Rayleigh wave in steel

$H_{reinforcement}$: Weld reinforcement height

$$if \quad \frac{D}{2\tan(\theta_l)} > d_{penetration} \quad then \quad TOF_{LS} \quad does \quad not \quad exist \quad \textbf{Eq. 6-9}$$

Four extreme cases were simulated using modified TOF equations for 0.0126 m thick samples. These four cases represent the extremes of what the robotic welder is capable of achieving. Fig. 6-17 shows the simulation for 0.0126 m penetration depth and 0 m weld reinforcement height. LS and L(M)S(N)R_LS modes obscure the shear wave. Fig. 6-18 shows the simulation for 0.001 m penetration depth and 0 m weld reinforcement height. Fig. 6-19 shows simulation for 0.0126 m penetration depth and 0.01 m weld

reinforcement height. LS and L(M)S(N)R_LS modes once again obscure the shear wave. Fig. 6-20 shows simulation for 0.001 m penetration depth and 0.01 m weld reinforcement height.

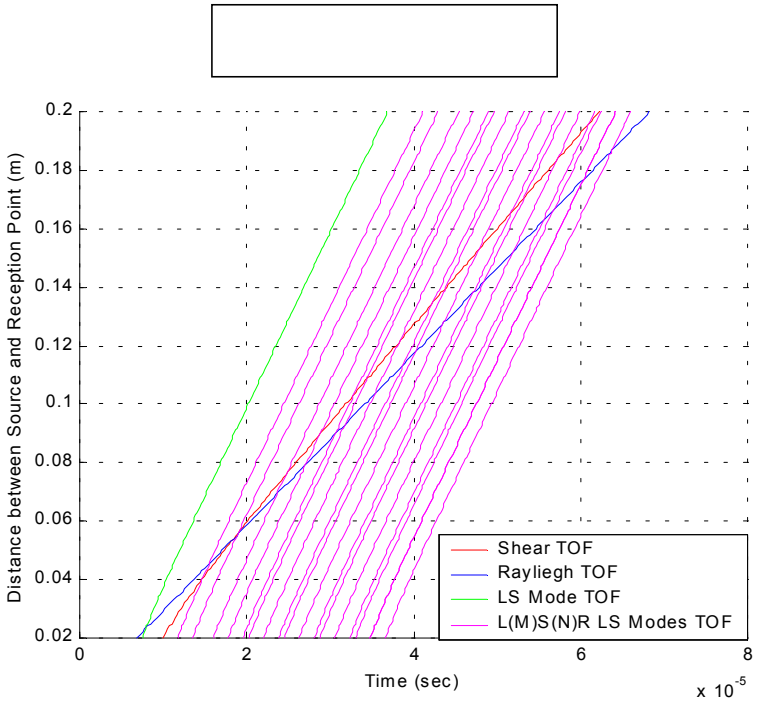

Fig. 6-17 : Theoretical TOFs for 0.0126 m thick sample, 0 m weld reinforcement height, 0.0126 m penetration depth

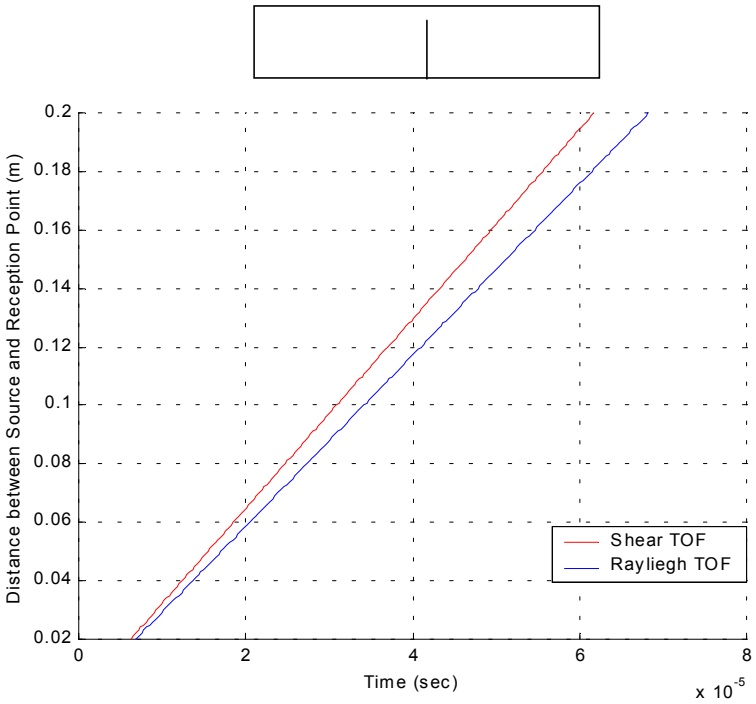

Fig. 6-18 : Theoretical TOFs for 0.0126 m thick sample, 0 m weld reinforcement height, 0.001 m penetration depth

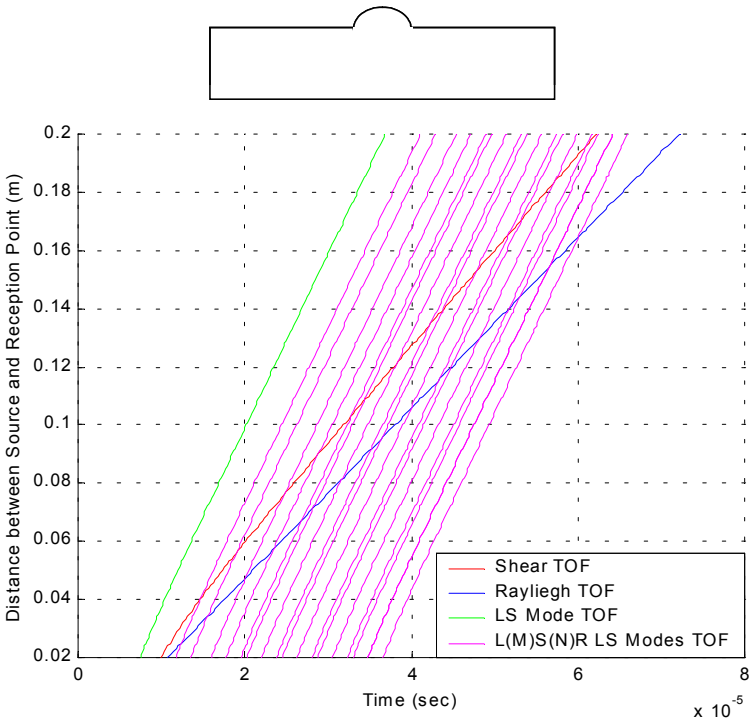

Fig. 6-19 : Theoretical TOFs for 0.0126 m thick sample, 0.01 m weld reinforcement height, 0.0126 m penetration depth

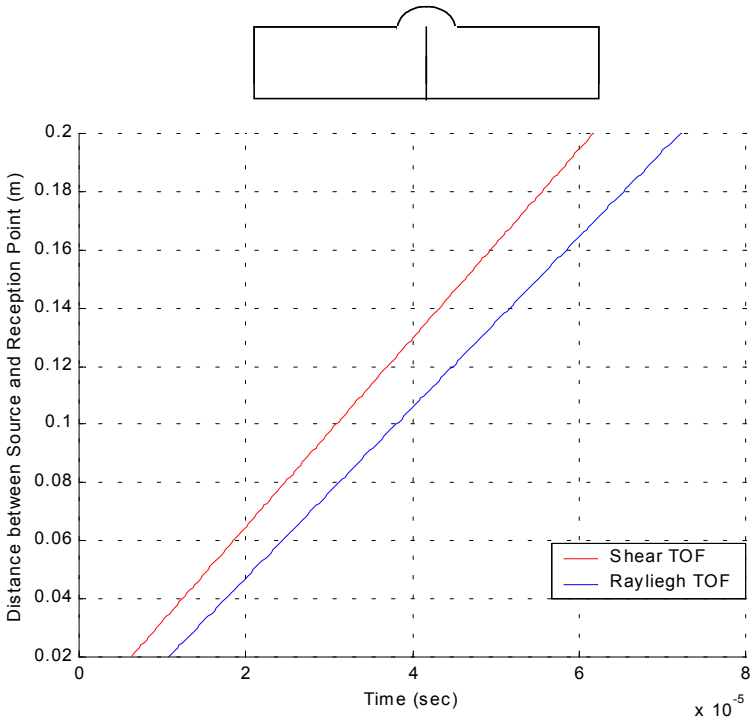

Fig. 6-20 : Theoretical TOFs for 0.0126 m thick sample, 0.01 m weld reinforcement height, 0.001 m penetration depth

These simulations show two important facts regarding the ultrasound propagation though a weld bead. First, LS Mode converted waves and L(M)S(N)R_LS Mode converted waves will obscure the shear wave and the Rayleigh wave if the weld penetration depth is too deep. This will be investigated further in the next section, Section 6.2. Second, the shear and Rayleigh wave arrive very close together used when the penetration depth is shallow. The shear and Rayleigh wave separate as the distance between source and generation points, *D*, increases. If the shear and Rayleigh wave arrive too closely, the two waves may interfere with each other. Therefore, the distance between source and generation point, *D*, has to be large enough so the shear and Rayleigh waves do not interfere.

6.2. Maximum Allowable Penetration Depth for a given Distance between Source and Reception Points

Simulations indicate the shear wave will be obscured if the LS and L(M)S(N)R_LS modes are allowed to propagate. The penetration depth where the LS and L(M)S(N)R(LS) Mode converted waves can propagate though the weld bead is the maximum allowable penetration depth, $d_{maxpenetration}$, because the Shear TOF and FMLPA method of measuring weld penetration depth relies on detecting the shear wave. The relationship between the maximum allowable penetration depth, $d_{maxpenetration}$, and distance between source and reception point, D, can be derived from Eq. 6-9 and is given in Eq. 6-10.

$$d_{max\ penetration} = \frac{D}{2\tan(\theta_l)} \qquad \textbf{Eq. 6-10}$$

Fig. 6-21 shows maximum allowable penetration depth vs. distance between source and reception points for a 0.0126 m thick sample. The maximum allowable penetration depth decreases as the distance between source and reception point increases. As an example, Fig. 6-22 shows LURL EMAT signals for two different welded samples. Each signal was taken with D of 0.06 m and a thickness of 0.0126 m. The first signal has a penetration depth of 4.51 mm and no L(M)S(N)R_LS modes can be seen. The second signal has a penetration depth of 8.61 mm and L(M)S(N)R_LS modes can be seen.

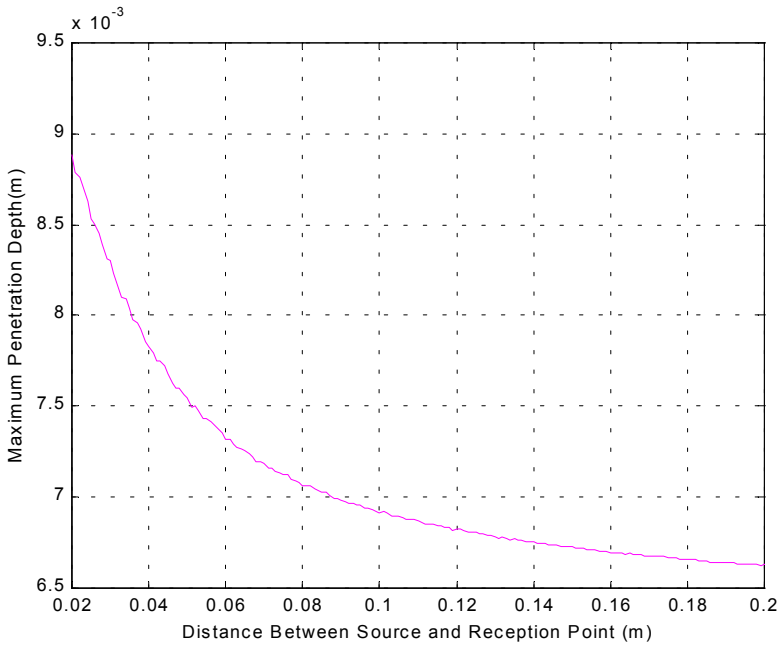

Fig. 6-21 : Maximum weld penetration depth , Dmax penetration, for 0.0126 m samples.

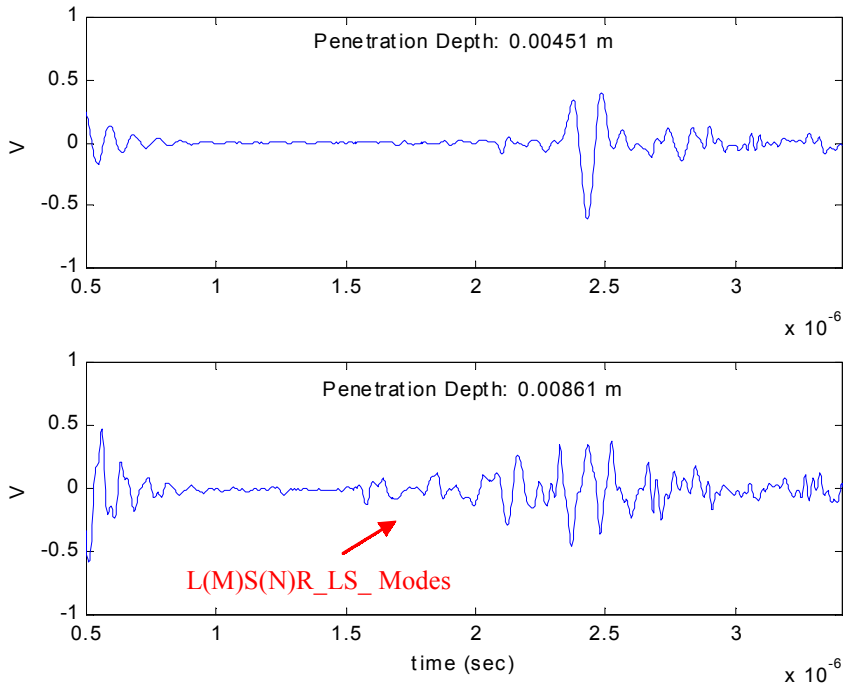

Fig. 6-22 : LURL EMAT signals for two different penetration depths

Fig. 6-23 shows maximum allowable penetration depth vs. distance between source and reception points for a 0.00635 m thick sample. As an example, Fig. 6-24 shows LURL EMAT signals for two different welded samples. Each signal was taken with *D* of 0.04 m and a thickness of 0.00635 m. The first signal has a penetration depth of 3.52 mm and no L(M)S(N)R_LS modes can be seen. The second signal has a penetration depth of 6.65 mm and L(M)S(N)R_LS modes can be seen.

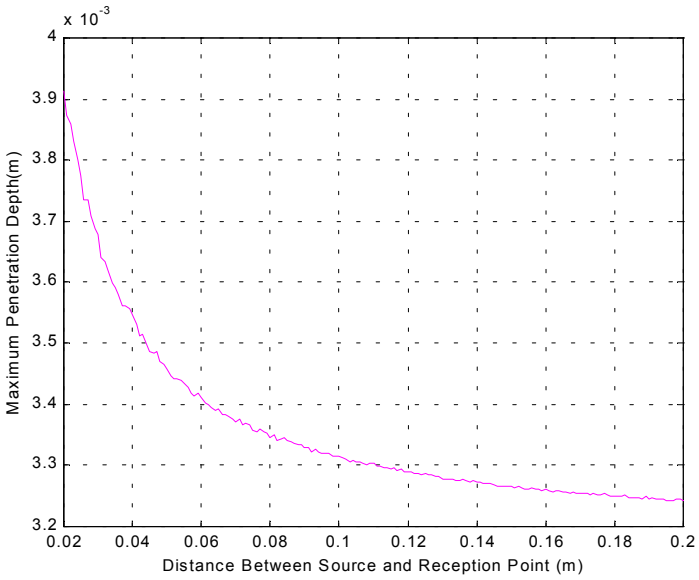

Fig. 6-23 : Maximum weld penetration depth , Dmax penetration, where the LS and L(M)S(N)R_LS modes cannot propagate though vs. D for 0.00635 m samples.

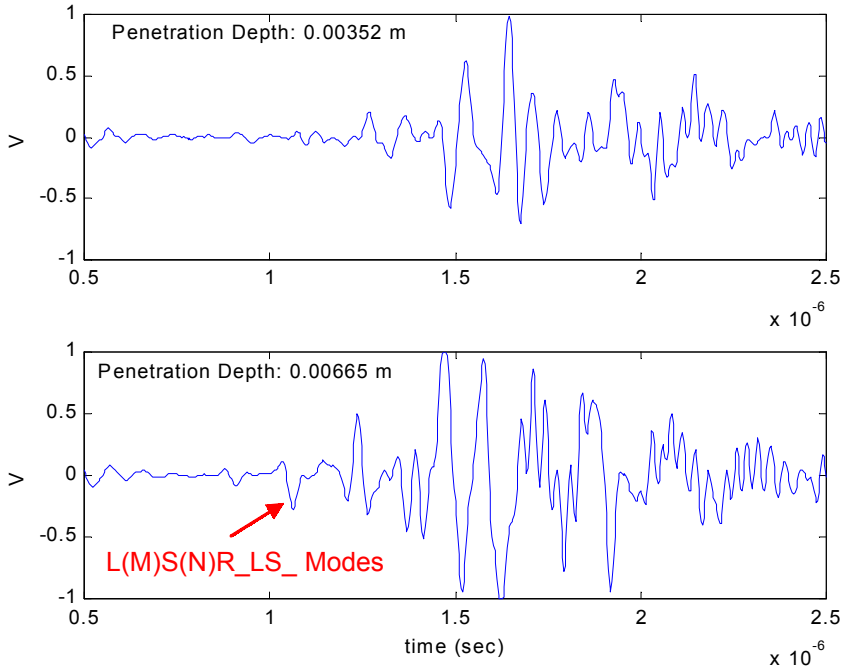

Fig. 6-24 : LURL EMAT signals for two different penetration depths using 0.00635 m samples. Distance between source and reception point is 0.04 m

These results indicate that there is a limitation on the maximum weld penetration depth that can be measured due to the LS and L(M)S(N)R_LS mode converted waves. This limitation includes the shear TOF and FMLPA method of weld penetration depth measurement since the L(M)S(N)R_LS mode can obscure the shear wave. Any other ultrasonic weld penetration depth measurement method should be checked to make sure the LS and L(M)S(N)R_LS Mode converted waves will not affect the measurement results.

Chapter 7

Ultrasonic Speeds In Weld Samples

Currently, all research in this area have used published values for ultrasound wave speeds by Scrubby and Moss for steel. [21,22,25] Ultrasonic wave speeds vary slightly between different types of steel like 1018 (low carbon), 1020 (low carbon), 1040 (medium carbon), 1060 (high carbon) etc. Shear TOF and FMLPA methods of measuring weld penetration depth accuracy depend on accurate ultrasonic wave speed. Ultrasonic wave speeds for the type of steel used for weld samples was measured.

7.1. Rayleigh Wave Speed Measurement

The experimental setup used to measure Rayleigh wave speed is shown in Fig. 7-1. Two laser pulses are fired at the same time onto a piece of steel used for weld samples. A distance of 0.050 m separates where the two laser pulses are incident on the surface. A EMAT or PZT is placed directly inline with the two laser pulses.

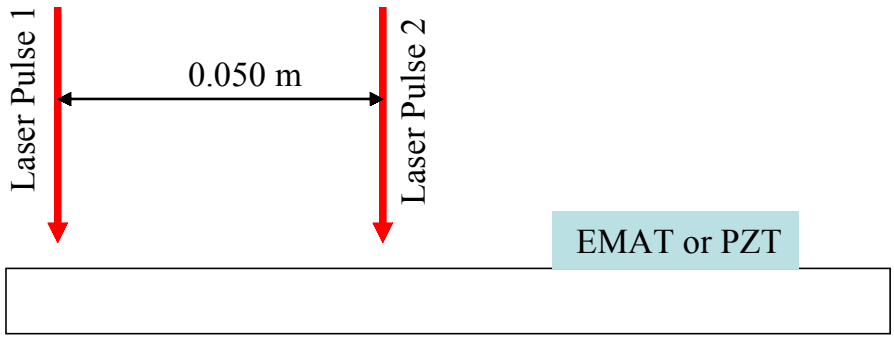

Fig. 7-1 : Experimental Setup to Measure Rayleigh Wave Speed

Rayleigh wave speed was calculated using Eq. 7-1.

$$C_R = \frac{0.050}{\tau 2 - \tau 1} \qquad \textbf{Eq. 7-1}$$

Where:

C_R : Rayleigh wave speed

$\tau 1$: Rayleigh wave arrival time from laser pulse 1

$\tau 2$: Rayleigh wave arrival time from laser pulse 2

The signal obtained with the LURL EMAT is shown in Fig. 7-2. Rayleigh wave speed measurement results with the LURL EMAT are as follows:

Rayleigh Speed: 3000.05 m/s

Published Rayleigh Speed: 2980 m/s

Percent Difference: 0.67 %

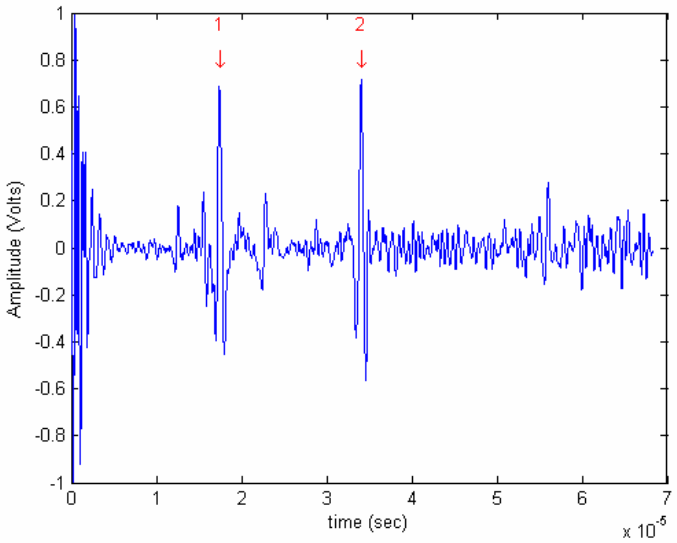

Fig. 7-2 : Received LURL EMAT signal

1 : Rayleigh wave from laser pulse 2

2 : Rayleigh wave from laser pulse 1

The signal obtained with a V153 PZT is shown in Fig. 7-3. Rayleigh wave speed measurement results with the V153 PZT are as follows:

Rayleigh Speed: 3000.00 m/s

Published Rayleigh Speed: 2980 m/s

Percent Difference: 0.67 %

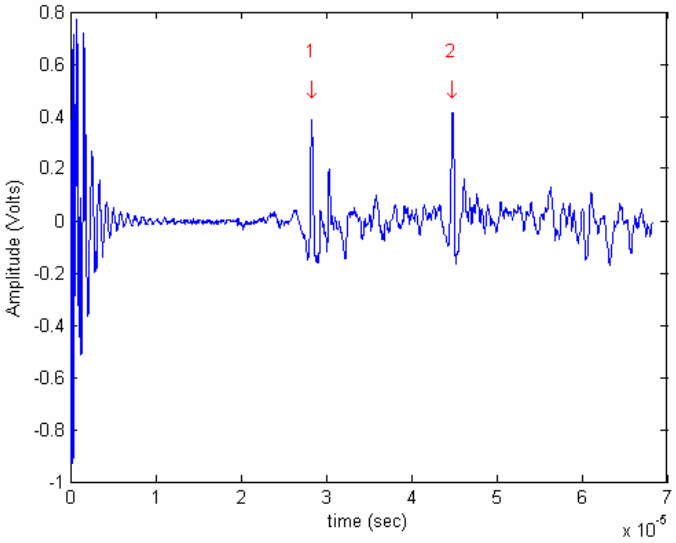

Fig. 7-3 : Received V153 PZT signal

1 : Rayleigh wave from Array Member 1

2 : Rayleigh wave from Array Member 2

The measured Rayleigh wave speeds using both the LURL EMAT and V153 PZT are 3000 m/s. The difference between the published and measured wave speed might be due to heavy oxidation on the sample surface. This is a 20 m/s difference from the published wave speed. The following chapters will use the measured 3000 m/s instead of the published 2980 m/s wave speed.

7.2. Shear and Longitudinal Wave Speed Measurements

The experimental setup used to measure shear and longitudinal wave speed is shown in Fig. 7-4. A single laser pulse is fired on one side of a piece of steel used for weld samples. An EMAT or PZT is placed on the opposite side of the laser pulse. A shear or longitudinal wave generated by the laser pulse will reflect back and forth between the two sides of the sample. Consecutive shear or longitudinal waves received by the EMAT or PZT has to travel twice the thickness of the steel sample. The LURL EMAT cannot acquire longitudinal waves so it will be used to measure shear wave speed. A V153 Panametrics shear wave PZT will also be used to measure shear wave speed. A A403 Panametrics longitudinal wave PZT will be used to measure longitudinal wave speed.

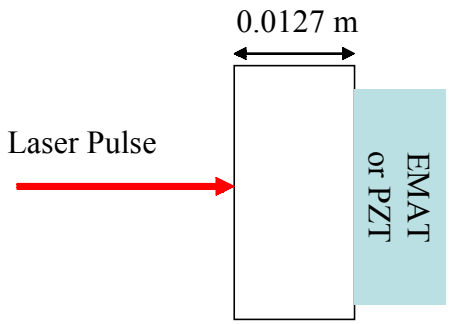

Fig. 7-4 : Experimental Setup to Measure Shear and Longitudinal Wave Speed

The shear and longitudinal wave speed was calculated using Eq. 7-2.

$$C_{S,L} = \frac{4 \cdot 0.0127}{\tau 2 - \tau 1} \qquad \textbf{Eq. 7-2}$$

Where: $C_{S,L}$: Shear or longitudinal wave speed

$\tau 1$: Direct wave

$\tau 2$: 2nd Reflected Wave

The signal obtained with the LURL EMAT is shown in Fig. 7-5. Shear wave speed measurement results with the LURL EMAT are as follows:

Shear Speed: 3234.30 m/s

Published Shear Speed: 3240 m/s

Percent Difference: -0.18 %

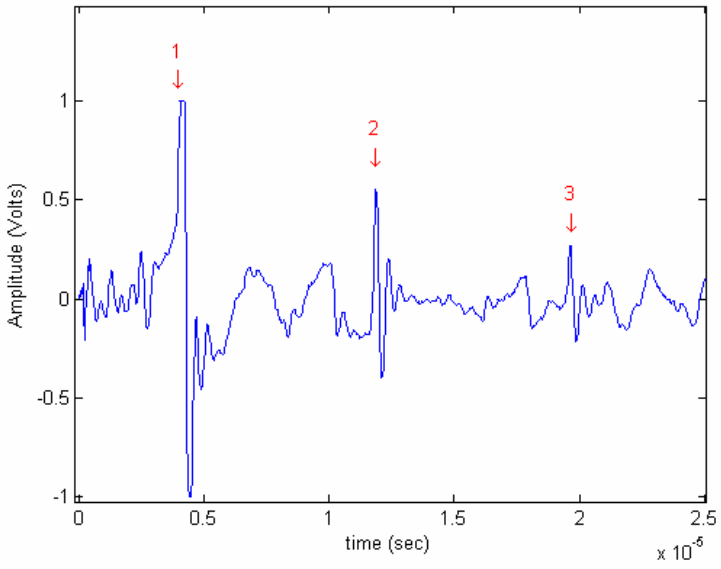

Fig. 7-5 : Received LURL EMAT

1 : Direct Shear

2: 1st Reflection

3: 2nd Reflection

The signal obtained with the V153 PZT is shown in Fig. 7-6. Shear wave speed measurement results with the V153 PZT are as follows:

Shear Speed: 3236.04 m/S

Published Shear Speed: 3240 m/s

Percent Difference: -0.18 %

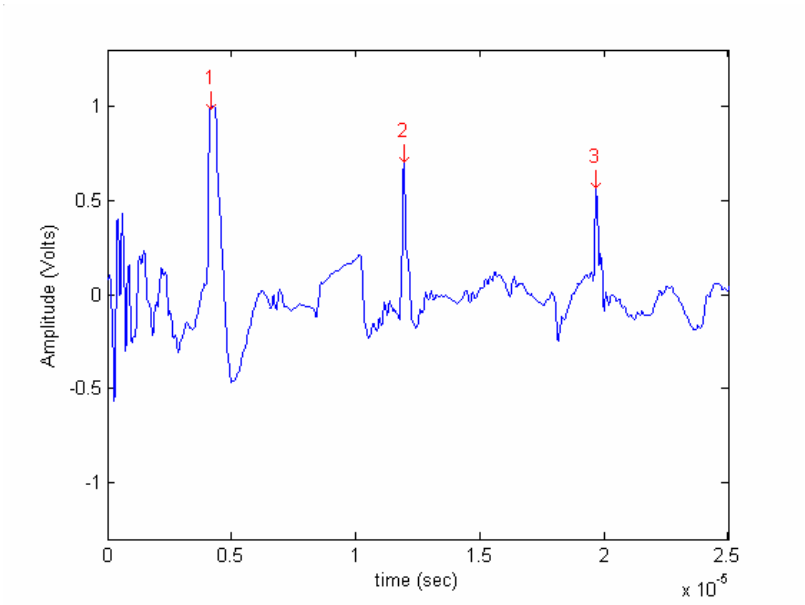

Fig. 7-6 : Received V153 PZT Signal

1 : Direct Shear

2 : 1st Reflection

3: 2nd Reflection

The signal obtained with a A403 longitudinal wave PZT is shown in Fig. 7-7.

Longitudinal wave speed measurement results with the A403 PZT are as follows:

Longitudinal Speed: 5964.91

Published Longitudinal Speed: 5960 m/s

Percent Difference: 0.082 %

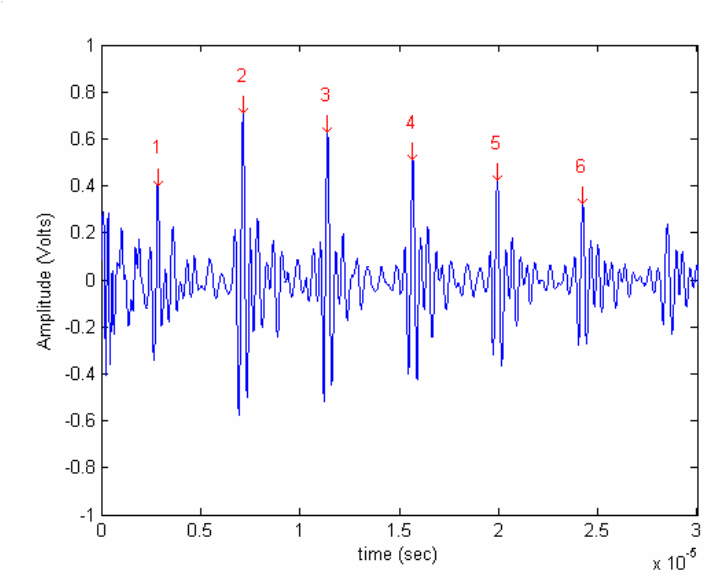

Fig. 7-7 : Received A403 PZT Signal

1 : Direct Longitudinal 2 : 1st Reflection 3: 2nd Reflection

4: 3rd Reflection 5: 4th Reflection 6: 5th Reflection

The measured wave speed for longitudinal and shear waves match published values closely. Since the shear and longitudinal waves match published values, the 20 m/s difference between the measured and published Rayleigh wave is probably due to heavy oxidation of the surface. The measurement methods demonstrated in this chapter are easy to implement and should be repeated for new weld samples to insure accuracy in any weld penetration depth measurement technique used.

Chapter 8

New Data Acquisition Trigger Sensor

A new data acquisition trigger was created using a Fairchild QSE113 phototransistor as a photovoltaic cell. The common pin of the phototransistor was connected to channel A of the GAGE 6012 PCI A/D card and emitter pin to ground. The phototransistor creates a negative pulse when light scattered from the front window of the laser hits it. Comparison of the old laser trigger signal is shown in Fig. 8-1.

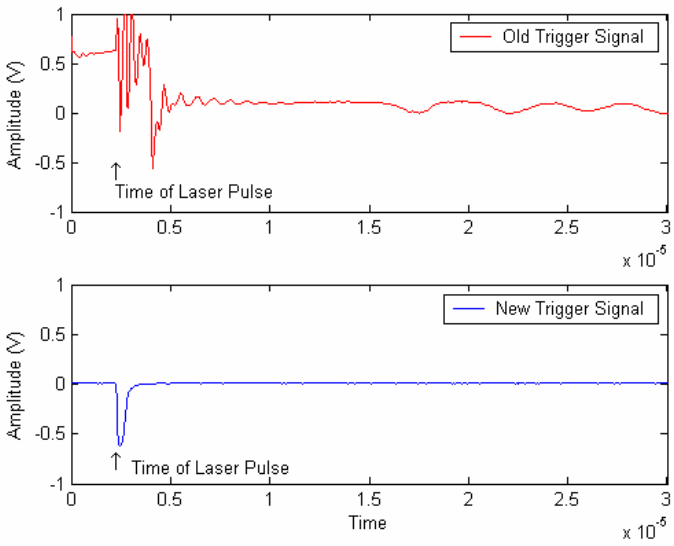

Fig. 8-1 : Old and new data acquisition trigger signal

The old trigger signal is very noisy and is inconsistent between each laser pulse. The noisy trigger signal makes it difficult to keep the time between laser pulse and start of data acquisition consistent. The new trigger signal is clean and repeatable. Consistent timing between laser pulse and start of data acquisition is therefore possible with the clean trigger signal and is important when using TOF techniques. This new trigger signal

was used for measurements done off-line after welding. It is not suitable for use on-line during welding since the weld arc generates infrared light that can create a false trigger signal. The old trigger pulse has to be used for on-line measurements during welding.

Chapter 9

Ultrasound Signal in Weld Samples

A signal was obtained in a pre-welded sample with a penetration depth of 0.003 m to see if a clean unmasked shear wave could be observed. The experimental setup 1 is shown in Fig. 9-1.

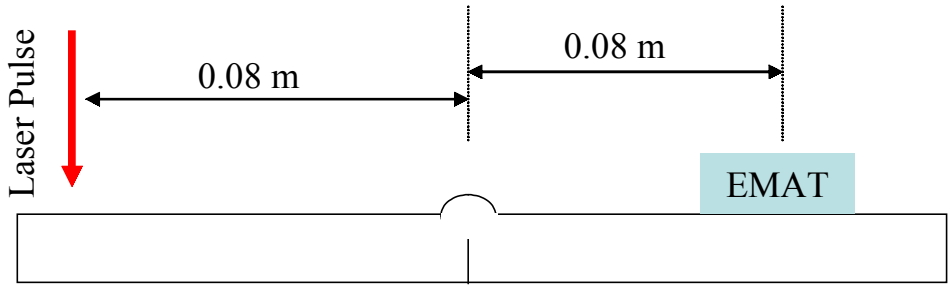

Fig. 9-1 : Experimental Setup 1 to Measure Shear Wave

The received signal is shown in Fig. 9-2.

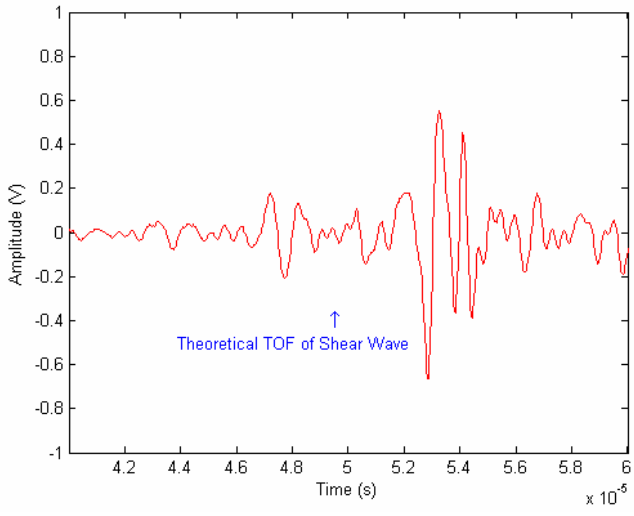

Fig. 9-2 : Received LURL EMAT Signal from Experimental Setup 1

There is a unknown wave stronger than the shear wave before the shear wave. This unknown wave has the potential to mask or alter the shear wave so the propagation path of the unknown wave has to be determined.

9.1. Discovery of the RGLS Mode Converted Wave

Two other experimental setups were used to determine the unknown wave. Experimental setup 2 is shown Fig. 9-3 is used to determine the unknown wave on the generation side of the weld bead. Experimental setup 3 is shown in Fig. 9-4 is used to determine the unknown wave on the reception side of the weld bead.

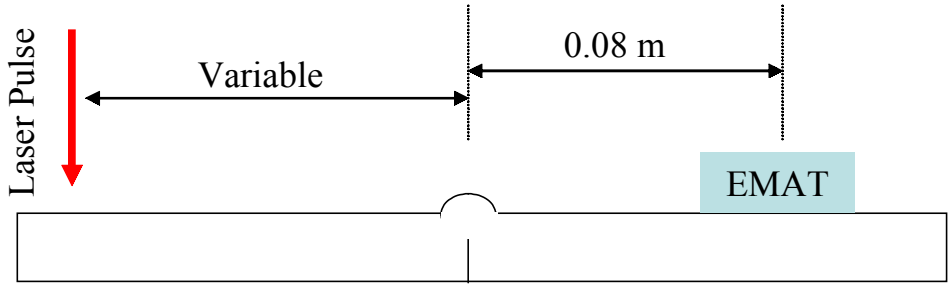

Fig. 9-3 : Experimental Setup 2 to determine unknown wave on the generation side of the weld bead

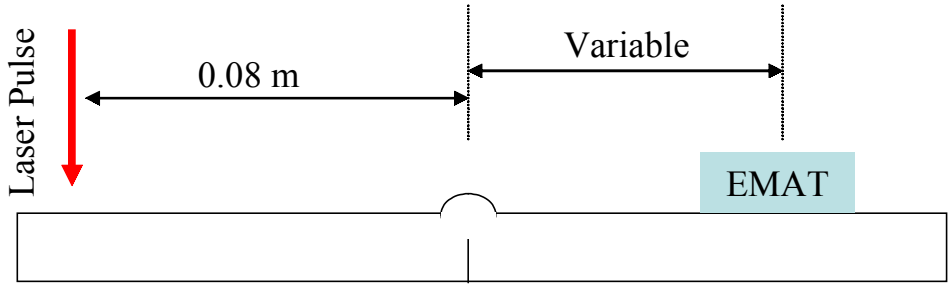

Fig. 9-4 : Experimental Setup 3 to determine unknown wave on the reception side of the weld bead

Example waves from the two experimental setups are shown in Fig. 9-5. Arrows indicate the unknown waves in the figures.

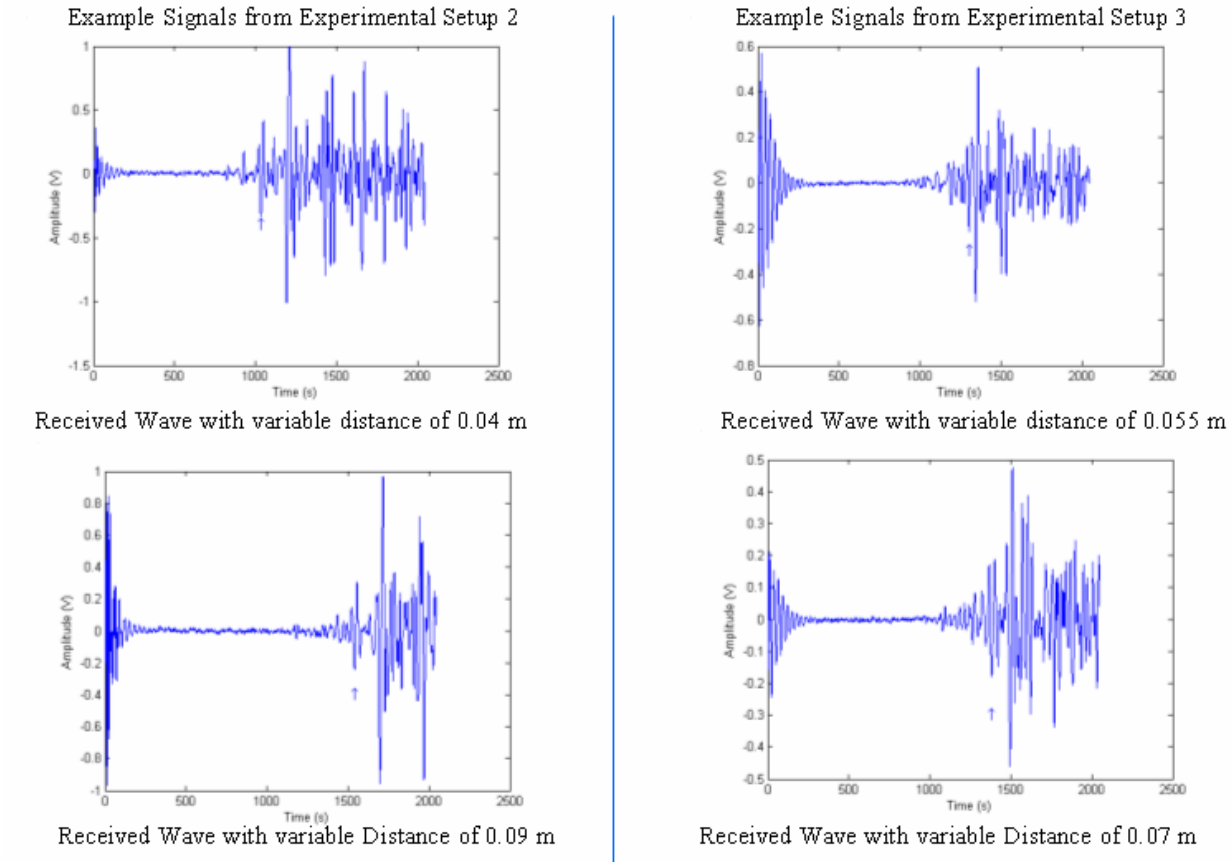

Fig. 9-5 : Example signals from experimental setup 2 and 3

Experimental results are shown in Fig. 9-6 and Fig. 9-7. Blue circles indicate arrival times for the unknown wave for different variable distances. Red lines are linear fits of the data. The dependent variable is shown on horizontal axis and independent variable is on the vertical axis. This was done so that the slope of the linear fit is in m/s.

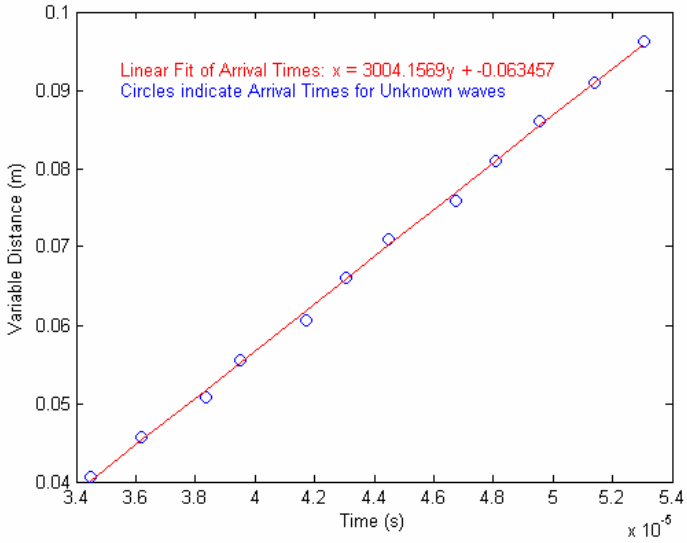

Fig. 9-6 : Results for Experimental Setup 2

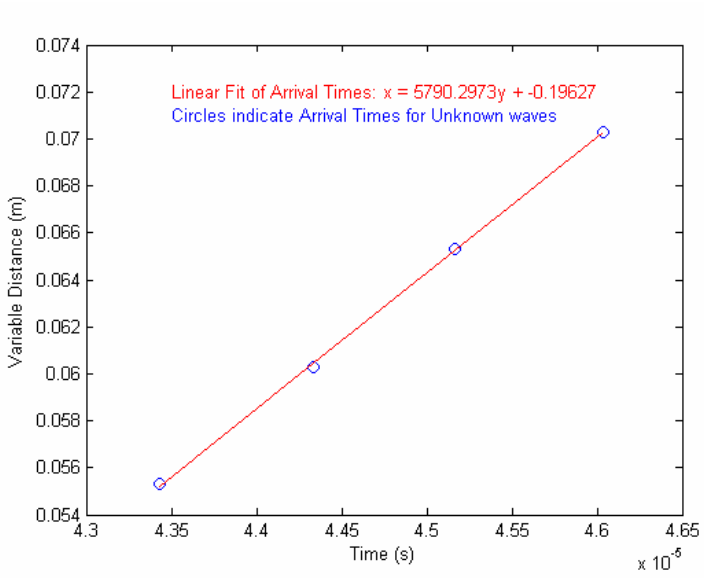

Fig. 9-7 : Results for Experimental Setup 3

For experimental setup 2 the linear fit indicates a speed of approximately 3004 m/s. This indicates that the unknown wave is traveling as a Rayleigh wave between the generation point and weld. For Experimental Setup 3 the linear fit indicates a speed of approximately 5790 m/s. This indicates that the unknown wave has a longitudinal component between the weld and reception point. As seen in the flat plate experiments, the only wave with a longitudinal component that can be seen is a LS mode converted wave.

An experiment was preformed to see if the Rayleigh component of the unknown wave was traveling on the top surface or bottom surface. A signal was taken using experimental setup 1. Then a slot was cut on the top surface between the generation point and the weld bead to reflect any Rayleigh wave back towards the generation point. Another signal was then taken. The two signals are shown in Fig. 9-8. The experimental results show that the unknown wave still propagates though while the top surface Rayleigh wave is reflected

back towards the generation point by the slot. This means the unknown wave is traveling on the bottom surface as a Rayleigh wave.

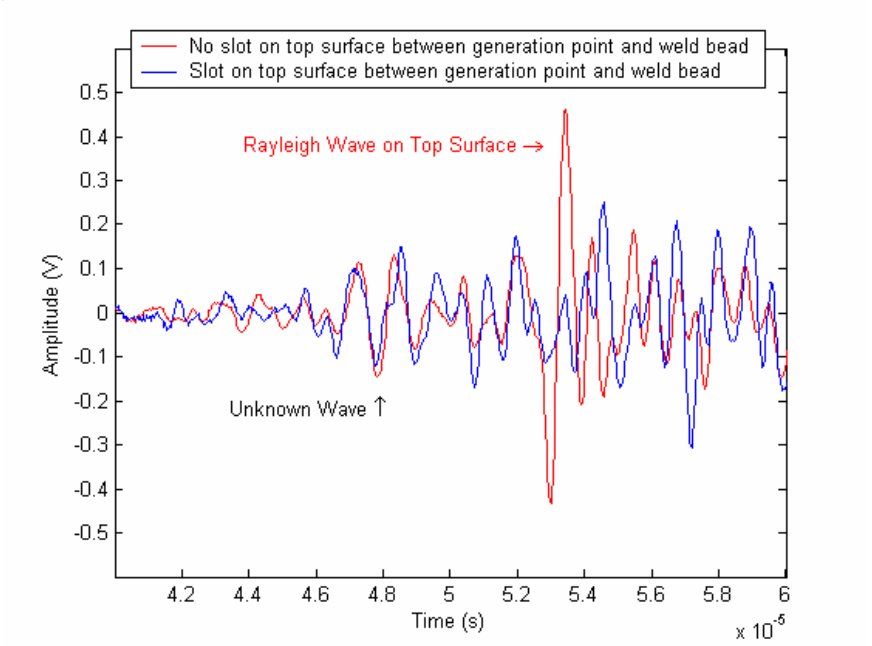

Fig. 9-8 : Unknown wave with and without slot between generation point and weld bead

The Rayleigh wave on the bottom surface must have been created from a bulk wave. If the top surface Rayleigh wave had traveled around the sample to the bottom, the slope seen from experimental setup 2 would be -3004 ms. NDT literature mentions surface following longitudinal and shear waves, creep waves, Stonely waves, etc. created from bulk waves. However, there are no mention of how a bulk wave can create a Rayleigh wave in NDT literature.

Careful thought about the nature of a Rayleigh wave and physics behind Snell's law can lead to an answer. Rayleigh waves are a combination of shear and longitudinal waves. Snell's law enforces the relationship between wavelength and wave speed. A laser pulse

on the surface generates both shear and longitudinal waves as a hemispherical wave front within the bulk of the material. Within the generated longitudinal hemispherical wave front, there is an angle, θ_{GL} , where the horizontal component of the longitudinal wavelength, λ_L, matches the Rayleigh wavelength, λ_R. Similarly, there is an angle θ_{GS} within the generated shear hemispherical wave front where the horizontal component of the shear wavelength, λ_S , matches the Rayleigh wavelength, λ_R. These relationships are shown in Fig. 9-10.

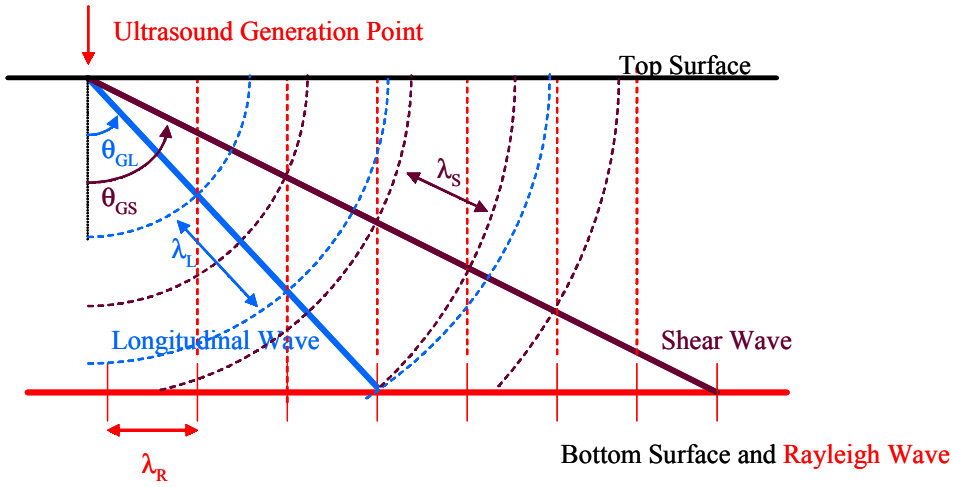

Fig. 9-9 : Determining λ_L and λ_S for Rayleigh wave generation on bottom surface

The angles θ_{GS} and θ_{GL} can be determined using Eq. 9-1 and Eq. 9-2.

$$\theta_{GL} = a\sin\left(\frac{\lambda_R}{\lambda_L}\right) = a\sin\left(\frac{\frac{C_R}{f}}{\frac{C_L}{f}}\right) = a\sin\left(\frac{C_R}{C_L}\right) \qquad \textbf{Eq. 9-1}$$

$$\theta_{GS} = a\sin\left(\frac{\lambda_R}{\lambda_S}\right) = a\sin\left(\frac{\frac{C_R}{f}}{\frac{C_S}{f}}\right) = a\sin\left(\frac{C_R}{C_S}\right) \qquad \textbf{Eq. 9-2}$$

Assume that the Rayleigh wave is generated between where the longitudinal wave and shear wave traveling along θ_{GL} and θ_{GS} strike the bottom surface as shown in Fig. 9-10. From simple geometry, the Rayleigh generation angle, θ_{RG}, is the average of θ_{GL} and θ_{GS}. The location on the bottom surface were the Rayleigh Wave is generated, D_{RG}, can be determined with θ_{RG} since the thickness, T, is known. This is shown in Eq. 9-3. The time between ultrasound generation on the top surface and Rayleigh wave generation on the bottom surface, t_{RG}, depends on when the hemispherical shear wave front reaches the generation point. T_{RG} can be calculated using Eq. 9-4.

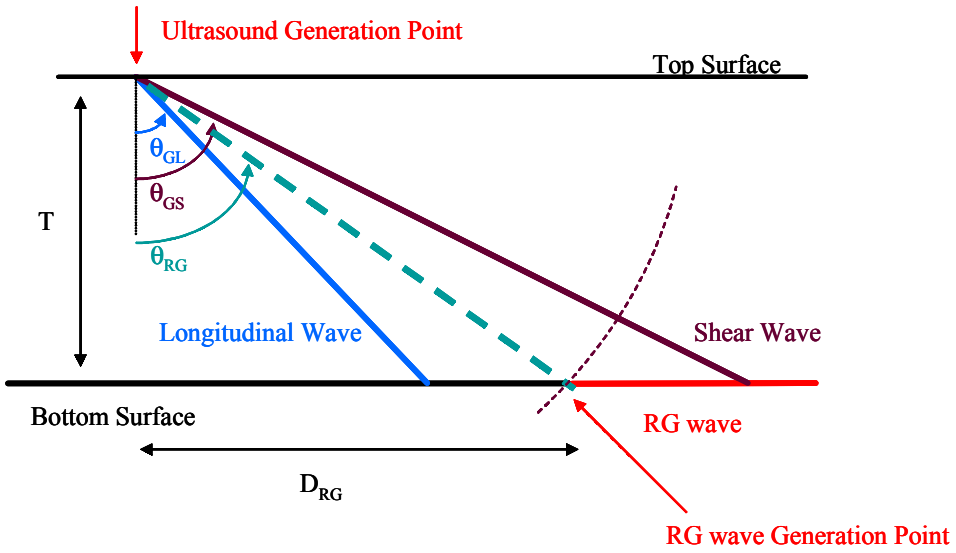

Fig. 9-10 : Determining D_{RG} for Rayleigh wave generation on bottom surface

$$D_{RG} = T \cdot tan(\theta_{RG}) \qquad \textbf{Eq. 9-3}$$

$$t_{RG} = \frac{T}{C_s \, cos(\theta_{RG})} \qquad \textbf{Eq. 9-4}$$

The complete path for the unknown wave is shown in Fig. 9-11. The laser pulse generates a Rayleigh wave on the bottom surface of the weld sample. The generated Rayleigh wave travels to the weld seam where it travels up the seam and strikes the bottom of the weld bead. A LS Mode converted wave is then generated at the bottom of the weld bead and travels to the sensor. The unknown wave will be referred to as the RGLS wave.

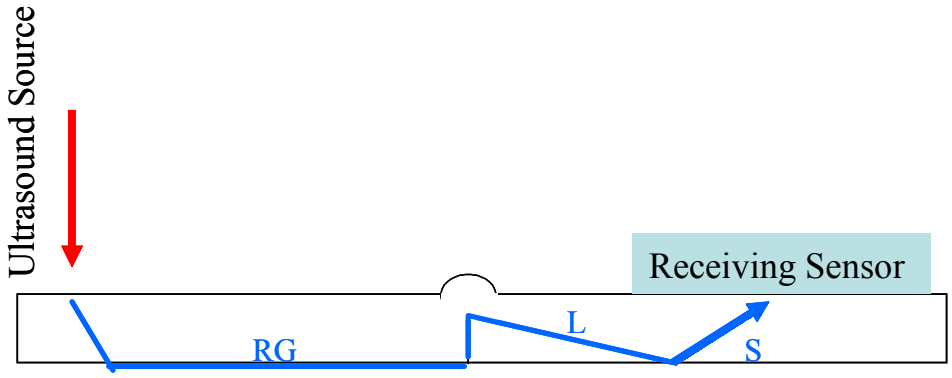

Fig. 9-11 : Path of the RGLS wave

Theoretical TOF for the RGLS wave, TOF_{RGLS}, can be calculated using the following equations:

$$TOF_{RGLS} = t_{RG} + \frac{(D_{GW} + T - d_{penetration} - D_{RG})}{C_R} + \frac{T - d_{penetration}}{C_L \, cos(\theta_{L1})} + \frac{T}{C_S \, cos(\theta_{S1})} \qquad \textbf{Eq. 9-5}$$

where:

t_{RG} : Time between laser pulse and bottom surface Rayleigh wave generation

D_{RG} : Horizontal distance between laser pulse and bottom surface Rayleigh wave generation point

D_{GW} : Distance between laser ultrasound generation point and weld bead

D_{WR} : Distance between weld bead and ultrasound reception point

T : Thickness of weld samples

$d_{penetration}$: Weld penetration depth

θ_{RG} : Rayleigh wave generation angle

C_R, C_L, C_S : Rayleigh, longitudinal, and shear wave speed

θ_{L1}, θ_{S1} : Angles for LS mode conversion of the wave path

The following two equations must be iterated to find θ_{L1} and θ_{S1} :

$$\frac{sin(\theta_{S1})}{C_S} = \frac{sin(\theta_{L1})}{C_L} \qquad \textbf{Eq. 9-6}$$

$$D_{WR} = T \cdot tan(\theta_{S1}) + (T - d_{penetration}) tan(\theta_{L1}) \qquad \textbf{Eq. 9-7}$$

Comparison of the theoretical TOF_{RGLS} and experimental data is shown in Fig. 9-12. The theoretical TOF_{RGLS} and unknown wave location show good agreement.

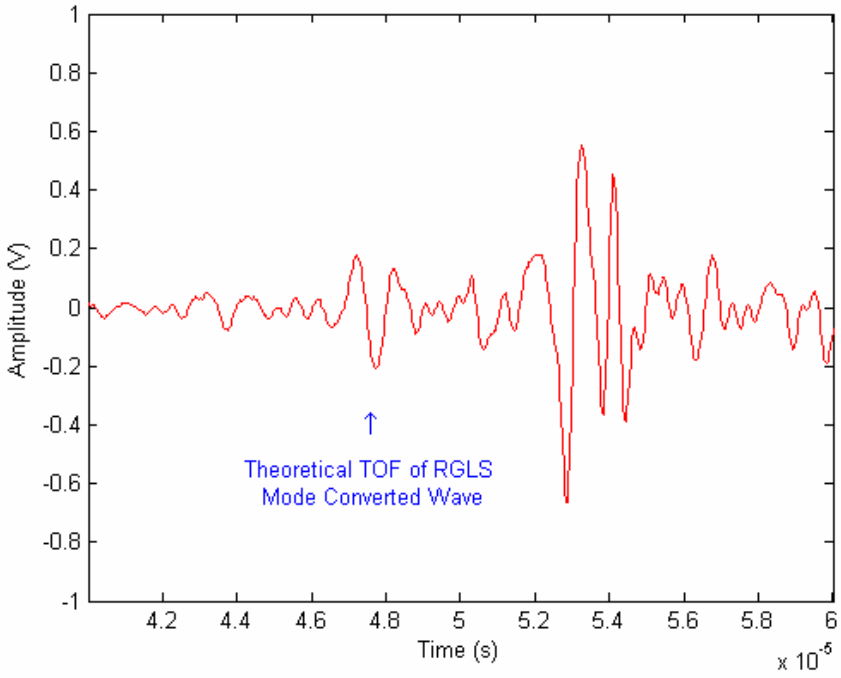

Fig. 9-12 : Comparison of theoretical TOF_{RGLS} and experimental data

Similar experiments with different weld penetration depths continued to show good agreement between the theoretical TOF_{RGLS} and unknown wave location. Therefore the assumption made on the Rayleigh wave generation location on the bottom surface seems to be accurate. The generation of the Rayleigh wave on the bottom surface by a pulse laser is not in current NDT literature. However, it is apparent why this has not been written about in NDT literature. Most ultrasonic NDT use PZT transducers which are incapable of generating both a longitudinal and shear wave at the same time and at the required angles to generate a Rayleigh wave on the bottom surface. In contrast, laser generation of ultrasound by a pulse produces longitudinal and shear waves at all angles from the generation point.

9.2. Simulation of RGLS, Shear, and Rayleigh Ultrasonic Wave Propagation though a Weld bead

The RGLS, Shear, and Rayleigh ultrasonic wave propagation though a weld bead can be simulated with the theoretical TOF_{RGLS} equation. The simulations can be used to determine the distance between the generation point and reception point required in order to acquire a shear wave reflecting from the bottom of the weld bead without interference from other waves. Three simulations were done for different distances of 0.10m, 0.14m and 0.16m between generation and reception points and are shown in Fig. 9-13 thru Fig. 9-15 respectively. The weld bead was placed in the middle of the generation and reception point. Each simulation shows the RGLS, shear, and Rayliegh TOF for different weld penetration depths. Weld reinforcement height was assumed to be 0 m which is the worst case scenario for the Rayliegh and shear wave. The Rayleigh and shear wave TOFs have the least amount of separation with a weld reinforcement height of 0m as determined by the simulations in Chapter 6. The total time to acquire the RGLS wave and Rayleigh wave was set to $2x10^{-6}$ s and $3x10^{-6}$ s respectively based on the signal shown in Fig. 9-12.

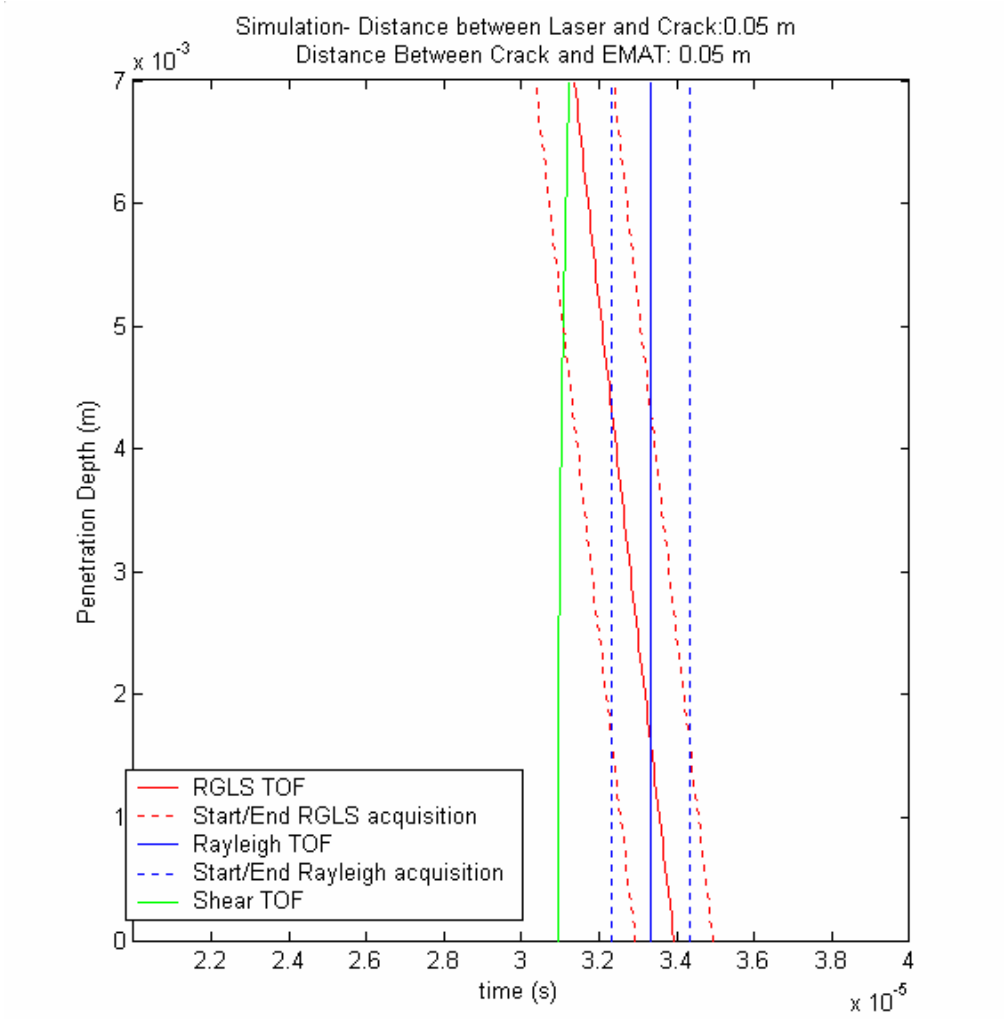

Fig. 9-13 : Simulation with 0.10 m between generation and reception points.

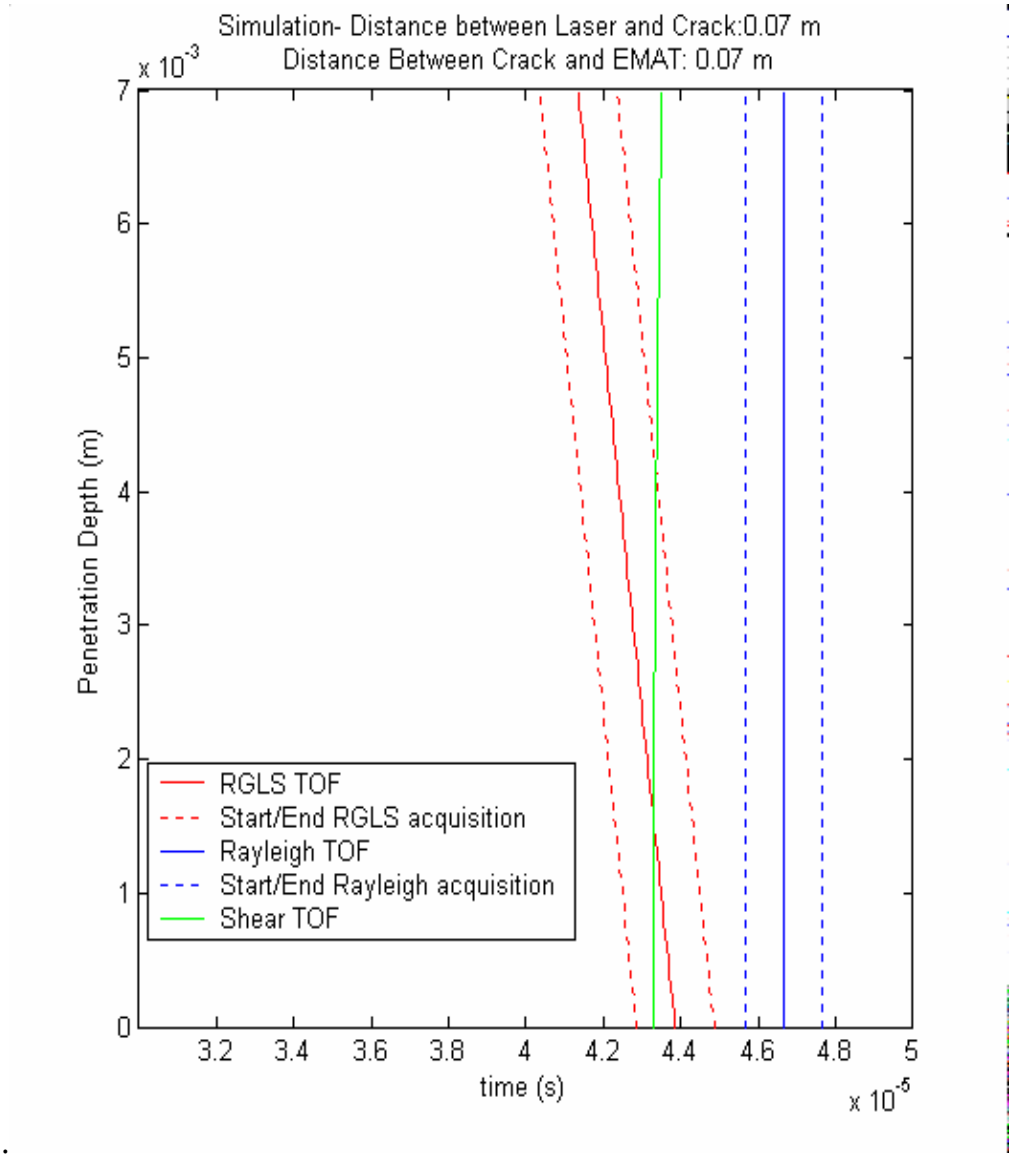

Fig. 9-14 : Simulation with 0.14 m between generation and reception points.

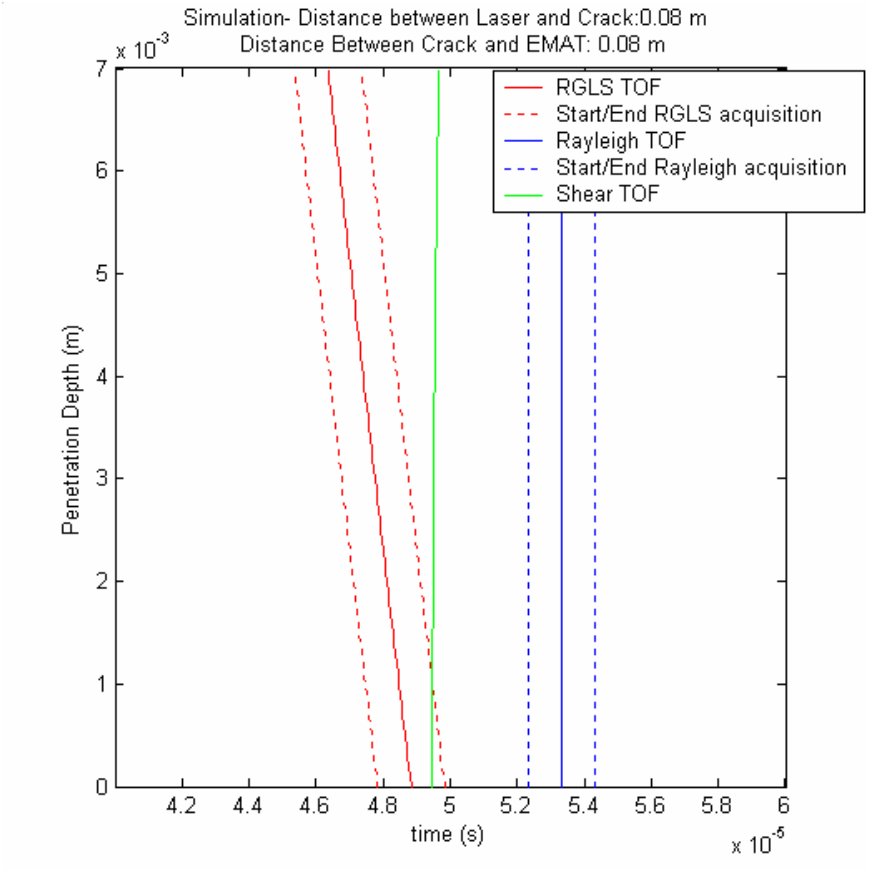

Fig. 9-15 : Simulation with 0.16 m between generation and reception points.

It is apparent from the simulations that the Rayliegh wave start to mask the shear wave if the distance between generation and reception points is less than .10 m. The RGLS wave will mask the shear wave until the source receiver distance is greater than 0.16 m. When a phased array is used, the distance will become greater since each source will create an RGLS wave. At this distance the shear wave is very weak due to attenuation and is not received by the LURL EMAT efficiently since the angle into the LURL EMAT is very shallow. The shear wave will be difficult to acquire with sufficient amplitude. Both the shear TOF and FMLPA methods for measuring weld penetration depth require sensing the shear wave with sufficient amplitude and without interference from other waves.

Therefore shear TOF and FMLPA methods for measuring weld penetration depth is impractical and cannot be used for real time weld quality control. This result also helps explain why previous research was unsuccessful in measuring weld penetration depth using the shear TOF method of weld penetration depth. A new method must be invented in order to measure weld penetration depth. Fortunately, it is apparent from the path of the RGLS wave that it can be used to measure weld penetration depth. The RGLS TOF Method for weld penetration depth measurement will be developed in the next chapter.

Chapter 10

RGLS TOF Method for Weld Penetration Depth Measurement

The RGLS wave can be used to measure weld penetration depth since the RGLS wave travels from the bottom of the sample to the bottom of the weld bead along its path. If the generation and reception points are kept constant, the path of the RGLS wave will only change due to weld penetration depth. This change in path can be measured using the RGLS TOF. This means that the weld penetration depth can be measured using the RGLS TOF. This new method will be called the RGLS TOF method.

There are advantages to using the RGLS TOF method instead of the shear TOF and FMLPA methods. The RGLS wave generates the strongest signal before Rayleigh Wave. This makes signal analysis easier and reduces the amount of signal averaging required in order to get a sufficient signal to noise ratio. The high amplitude also makes it easier to acquire the RGLS wave in a noisy welding environment. The RGLS TOF method requires only one laser source as opposed to the FMLPA method. This would reduce the complexity and cost of the measuring system.

The RGLS TOF method also offers better resolution than the using the Shear TOF method. For example, assume a 0.0126 m thick sample and 0.16 m distance between generation point and reception point. The shear TOF at 0.0 m penetration depth is 4.947 x 10^{-5} sec. The shear TOF at 0.007 m penetration depth is 4.966x 10^{-5} sec. The difference in

shear TOF at 0.0 m and 0.007 m penetration depth is 1.9 x 10^{-7} sec. Number of samples at 30 Mhz sampling rate for 1.9x10^{-7} sec is 6 samples. Therefore the shear TOF measurement resolution is 0.007m divided by 6 samples which is 1.234x 10^{-3} m. The RGLS TOF at 0.0 m penetration depth is 4.851x 10^{-5} sec. The RGLS TOF at 0.007 m penetration depth is 4.603x 10^{-5} sec. The difference in shear TOF at 0.0 m and 0.007m is 2.48 x 10^{-6} sec. Number of samples at 30 Mhz sampling rate for 2.48 x 10^{-6} sec is 74. Therefore the RGLS TOF measurement resolution is 9.407 x 10^{-5} m. The RGLS TOF measurement resolution will be twelve times better than the shear TOF measurement resolution.

10.1. RGLS Method of Measuring Weld Penetration Depth Off-line after Welding

The experimental setup used for measuring weld penetration depth off-line after welding using the RGLS method is shown in Fig. 10-1. Laser pulses from a Laser Photonics Nd:YAG laser is redirected to the surface of the sample using a 45^{o} mirror. The LURL EMAT is placed on the other side of the weld bead against an adjustable locating stop. Pre-welded samples are fixed at a known position using clamps. The LURL EMAT signal is fed into a Khron-hite filter set to a 100 kHz to 5 Mhz band pass filter. The amplified signal is digitized using the GAGE 6012 PCI A/D Card.

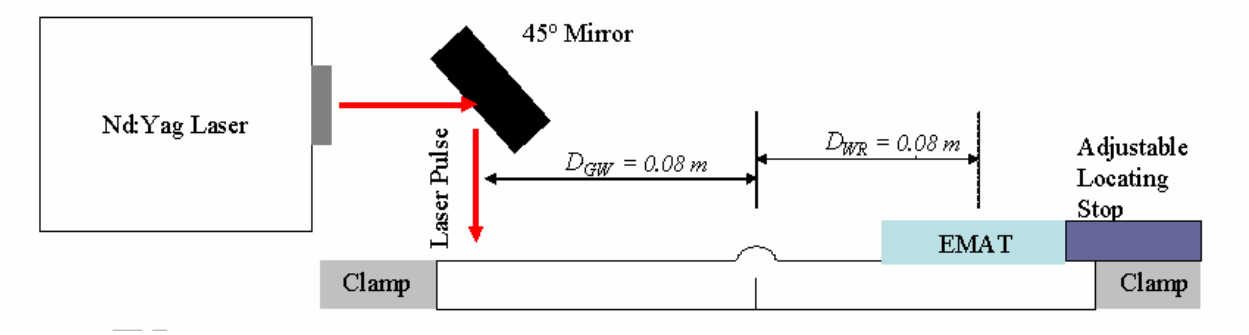

Fig. 10-1 : Experimental Setup to Measure Weld Penetration Depth off-Line after welding

The experimental procedure is as follows. A pre-welded sample is inserted between the clamps and the LURL EMAT is placed against the adjustable locating stop. Eight signals are taken and averaged. The RGLS TOF is measured by finding when the maximum peak before Rayleigh Wave occurs. Eq. 9-5 through Eq. 9-7 are iterated using the bisection method by adjusting an initial guess of penetration depth until the theoretical RGLS TOF matches the measured RGLS TOF. The final guess of penetration depth is compared to actual penetration depth. The actual penetration depth was measured using a optical scanner at 2400x2400 dpi resolution (Note: 1.06×10^{-5} m x 1.06×10^{-5} m resolution). A custom measuring program was written in Borland C++. A screen shot of the custom measuring program is shown in Fig. 10-2. You can select points A and B by clicking on the image. The calculate button will calculate distance between the points based on scanner resolution.

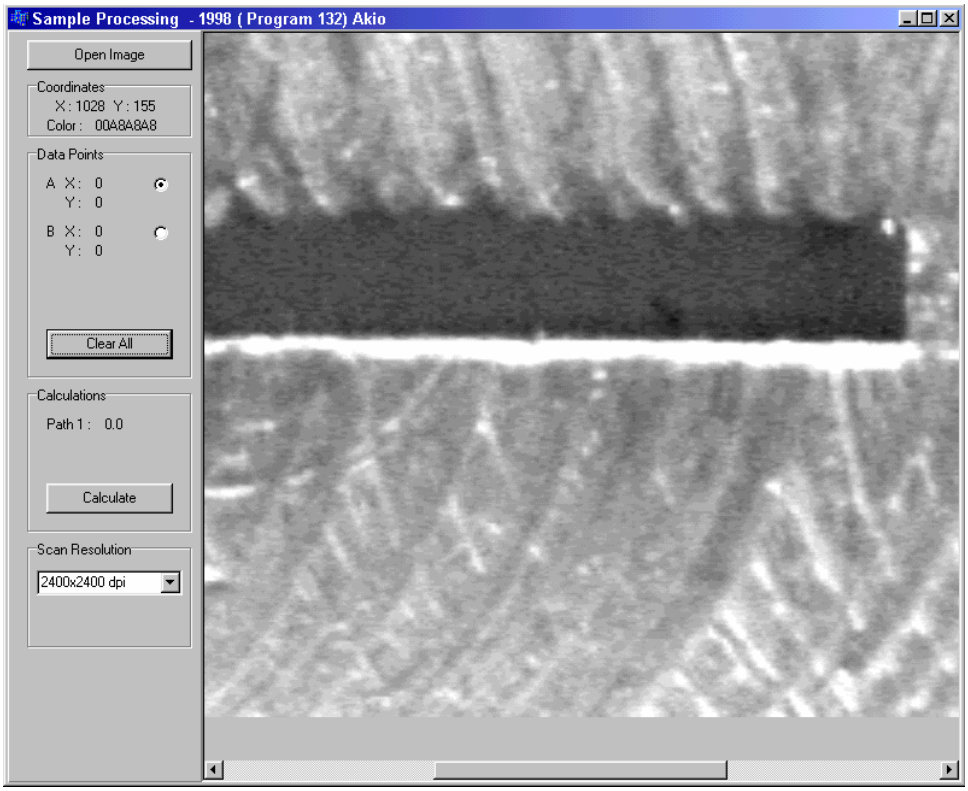

Fig. 10-2 : Program to measure penetration depth using optical scanner

Thirty five pre-welded samples were measured over three days. Fifteen pre-welded samples were measured during the first day. Ten pre-welded samples were measured during the remaining two days. The pre-welded samples were measured in this manner so that repeatability of the RGLS TOF method could be investigated. The results from each individual days are listed below. The average, maximum, and minimum absolute percent error is given for each day. The standard deviation of the differences between measured and actual weld penetration depth is also listed.

1. Results from Day 1

    - Average absolute Percent Error: 1.27 %
    - Minimum Percent Error: 0.19 %
    - Maximum Percent Error: 3.33 %
    - Standard Deviation of Differences : 5.11×10^{-5} m

Table 10-1 : RGLS method weld penetration depth measurement results from Day 1

Sample Number	Actual Penetration Depth	RGLS TOF Penetration Depth	Difference	Absolute Percent Error
A1	3.06E-03	2.98E-03	8.53E-05	2.78
A2	2.76E-03	2.70E-03	6.05E-05	2.19
A3	3.02E-03	3.07E-03	-4.89E-05	1.62
A4	3.86E-03	3.82E-03	3.40E-05	0.88
A5	3.19E-03	3.17E-03	2.40E-05	0.75
A6	4.81E-03	4.77E-03	3.72E-05	0.77
A7	4.09E-03	4.01E-03	8.10E-05	1.98
A8	2.70E-03	2.79E-03	-9.00E-05	3.33
A9	4.72E-03	4.68E-03	4.50E-05	0.95
A10	4.38E-03	4.39E-03	-1.20E-05	0.27
A11	3.81E-03	3.78E-03	3.30E-05	0.87
A12	3.37E-03	3.35E-03	1.82E-05	0.54
A13	4.51E-03	4.58E-03	-7.00E-05	1.55
A14	4.03E-03	4.01E-03	1.40E-05	0.35
A15	5.35E-03	5.34E-03	1.00E-05	0.19

2. Results from Day 2

    - Average absolute Percent Error: 1.13 %
    - Minimum Percent Error: 0.28 %
    - Maximum Percent Error: 2.79 %
    - Standard Deviation of Differences : 4.94x10-5 m

Table 10-2 : RGLS method weld penetration depth measurement results from Day 2

Sample Number	Actual Penetration Depth	RGLS TOF Penetration Depth	Difference	Absolute Percent Error
B1	3.10E-03	3.17E-03	-6.30E-05	2.03
B2	4.98E-03	4.96E-03	1.71E-05	0.34
B3	2.13E-03	2.14E-03	-6.00E-06	0.28
B4	4.99E-03	4.96E-03	3.20E-05	0.64
B5	5.01E-03	5.05E-03	-4.20E-05	0.84
B6	2.15E-03	2.14E-03	1.50E-05	0.70
B7	5.00E-03	4.96E-03	4.10E-05	0.82
B8	3.96E-03	3.92E-03	4.30E-05	1.09
B9	2.10E-03	2.14E-03	-3.69E-05	1.76
B10	3.72E-03	3.82E-03	-1.04E-04	2.79

3. Results from Day 3

- Average absolute Percent Error: 0.64 %
- Minimum Percent Error: 0.14 %
- Maximum Percent Error: 1.96 %
- Standard Deviation of Differences : 3.51×10^{-5} m

Table 10-3 : RGLS method weld penetration depth measurement results from Day 3

Sample Number	Actual Penetration Depth	RGLS TOF Penetration Depth	Difference	Absolute Percent Error
C1	2.50E-03	2.51E-03	-1.40E-05	0.56
C2	3.70E-03	3.68E-03	2.00E-05	0.54
C3	4.26E-03	4.25E-03	6.00E-06	0.14
C4	3.57E-03	3.50E-03	7.00E-05	1.96
C5	4.36E-03	4.34E-03	1.50E-05	0.34
C6	5.34E-03	5.40E-03	-6.10E-05	1.14
C7	4.08E-03	4.06E-03	1.60E-05	0.39
C8	4.42E-03	4.44E-03	-2.30E-05	0.52
C9	2.95E-03	2.93E-03	1.30E-05	0.44
C10	3.60E-03	3.59E-03	9.00E-06	0.25

Low percent errors show accuracy of the RGLS TOF method of finding weld penetration depth. Low standard deviation of the differences between measured and actual penetration depth show precision of the RGLS TOF method of finding weld penetration depth. In order to demonstrate repeatability of the RGLS TOF method, the measurement results for all three days were combined and is shown in Fig. 10-3. Average absolute percent error was 1.05 % for the combined results. Minimum percent error was 0.14 %. Maximum Percent Error was 3.33 %. The standard deviation of differences between measured and actual penetration depth is 4.62×10^{-5} m. The combined results are plotted with the actual versus measured penetration depth. The slope of a linear fit to the data is 0.9963 and the R-squared value is 0.9973. Both the slope and R-squared value indicates a very good correlation between the actual and measured weld penetration depth.

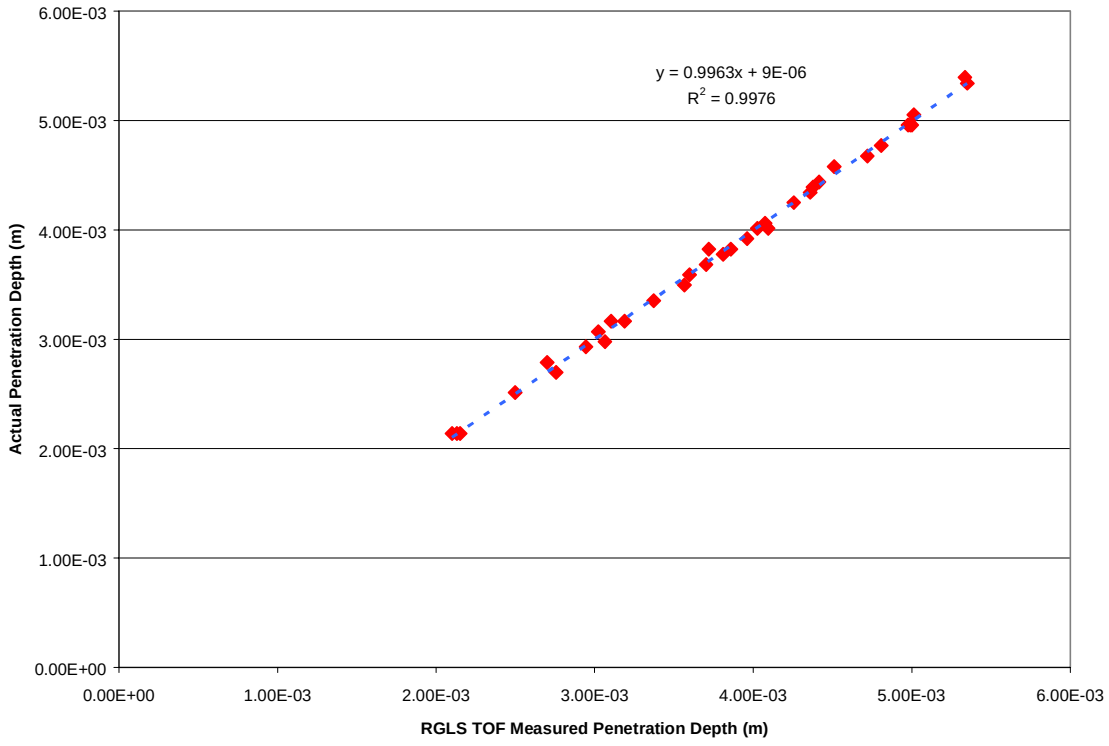

Fig. 10-3 : Combined Experimental Results

The standard deviation of the differences of the overall compared to the standard deviation of the differences for each day is within an order of magnitude. This shows repeatability of the RGLS TOF method of finding weld penetration depth. These experiments demonstrate the accuracy, precision, and reliability of the RGLS method for weld penetration depth measurement off-line after welding. This is also the first method to measure weld penetration depth accurately using non-contact ultrasound generation and reception off-line after welding. However, the real goal of this overall research thrust is to measure weld penetration depth on-line during welding. High temperature gradients may affect the RGLS methods measurement of the weld penetration depth.

10.2. RGLS Method of Measuring Weld Penetration Depth On-line during Welding

An experiment was done to see if the high temperature gradients will effect the measured RGLS wave during welding. The experimental setup is shown below in Fig. 10-4. LURL EMAT was used as the receiving sensor and a Laser Photonics ND:YAG laser was used for generating ultrasound. THe LURL EMAT and laser pulse location is stationary. The welding torch passes between the LURL EMAT and laser pulse location. Some welding parameters were fixed and some were variable in an attempt to generate different weld penetration depths. Fixed welding parameters used were 25 V welding voltage and the weld torch was .5 inches above the weld seam. Variable welding parameters used were torch speed and wire feed rate. An example signal obtained while welding is shown in Fig. 10-5. The example signal shows that noise is not an issue during welding.

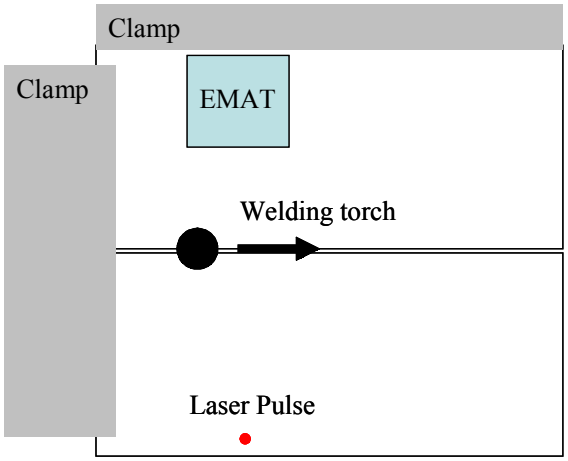

Fig. 10-4 : Top view of experimental setup to determine if high temperature gradients effects measured weld penetration depth during welding

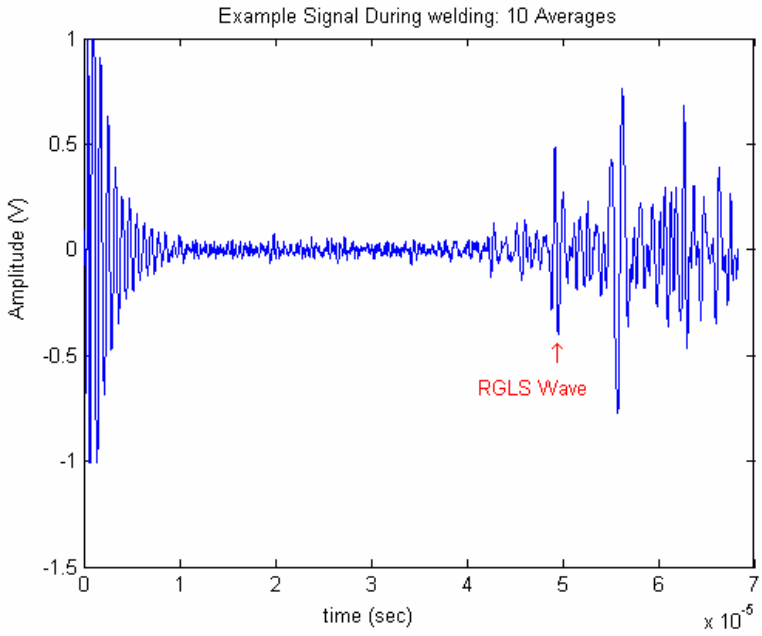

Fig. 10-5 : Example signal received during welding

10.3. RGLS Method of Measuring Weld Penetration Depth On-line During Welding Experimental Results

The experimental results are shown in Fig. 10-6 thru Fig. 10-11. The torch passes between the laser pulse and LURL EMAT at time 0s in all of the results.

In Fig. 10-6 , the torch speed was 0.5 in/sec and the wire feed rate was 500 in/min. The RGLS wave first starts to be received around 0.5 seconds after the torch passes. From 0 to 0.5 seconds, the weld is still molten and the RGLS wave cannot propagate through the weld bead. When the RGLS wave is received, the measured weld penetration starts lower than the actual penetration depth and approaches the actual weld penetration depth around nine seconds after the torch passes. The starting weld penetration depth is lower because ultrasound travels slower in high temperatures. The RGLS TOF is larger since the ultrasound travels slower. A larger RGLS TOF will result in the lower penetration depth.

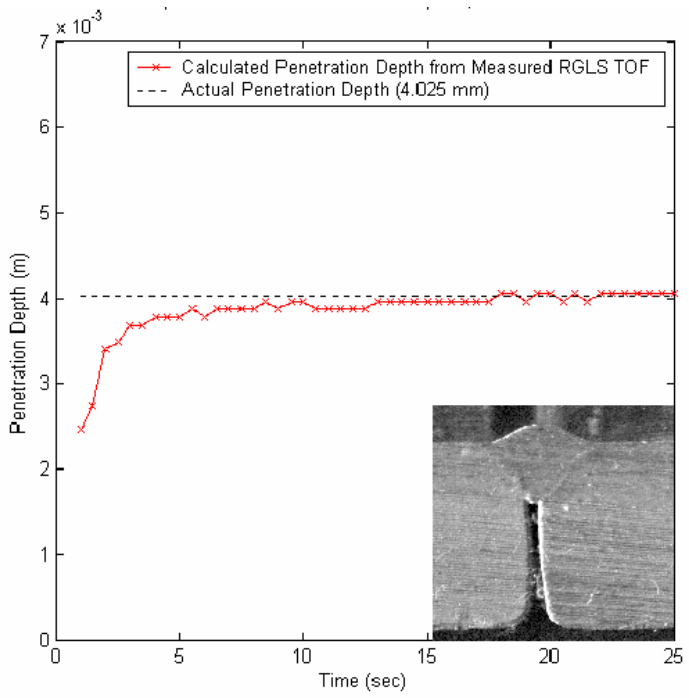

Fig. 10-6 : Measured Penetration Depth Vs. Time: 0.5 in/sec torch speed, 500 in/ min wire feed rate

In Fig. 10-7, the torch speed was 0.375 in/sec and the wire feed rate was 500 in/min. This experimental result is similar to the measurement result shown above in Fig. 10-6.

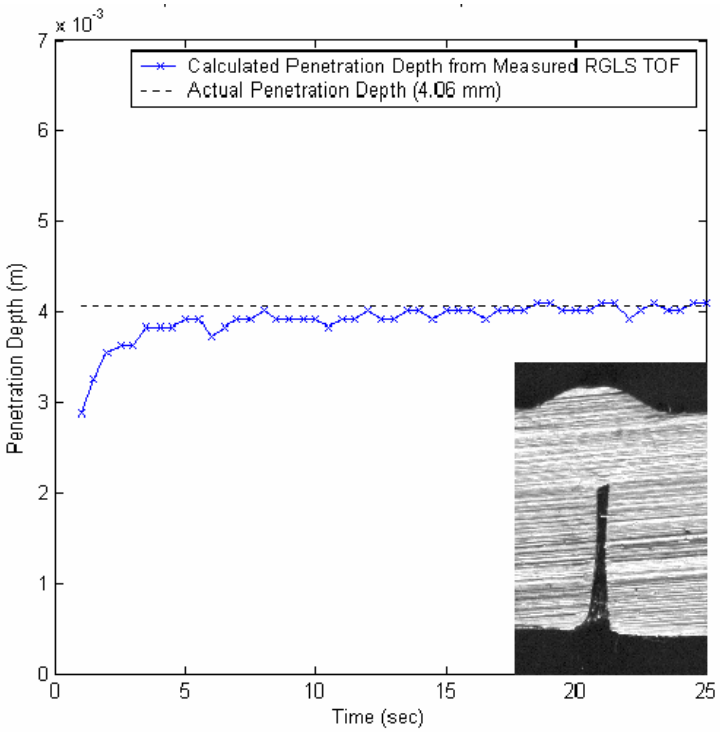

Fig. 10-7 :Measured Penetration Depth Vs. Time: 0.375 in/sec torch speed, 500 in/ min wire feed rate

In Fig. 10-8, the torch speed was 0.25 in/sec and the wire feed rate was 500 in/min. This experimental result is similar to the measurement result shown above in Fig. 10-6. However, since the torch speed was much slower than 0.5 in/sec, the heat input into the weld was higher. The weld took longer to cool with a higher heat input. This is the reason why the weld penetration depth measurement with the 0.25 in/sec torch speed took longer to approach the actual value than the weld penetration depth measurement with 0.5 in/sec torch speed.

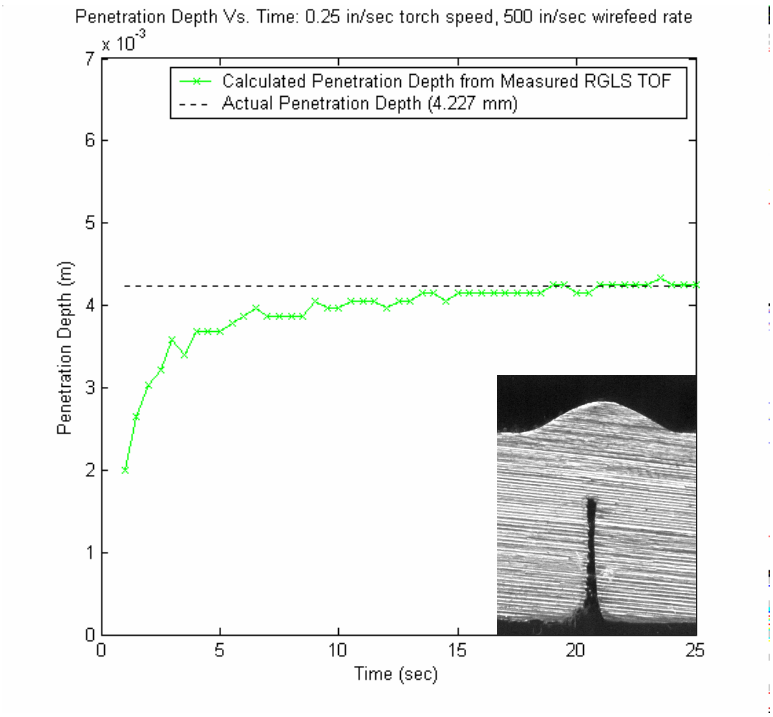

Fig. 10-8 : Measured Penetration Depth Vs. Time: 0.25 in/sec torch speed, 500 in/ min wire feed rate

In Fig. 10-9, the torch speed was 0.375 in/sec and the wire feed rate was 400 in/min. This is the only setting that produced a significant change in weld penetration depth. However, the RGLS TOF method of weld penetration depth measurement still converged to the actual value when the weld cooled sufficiently.

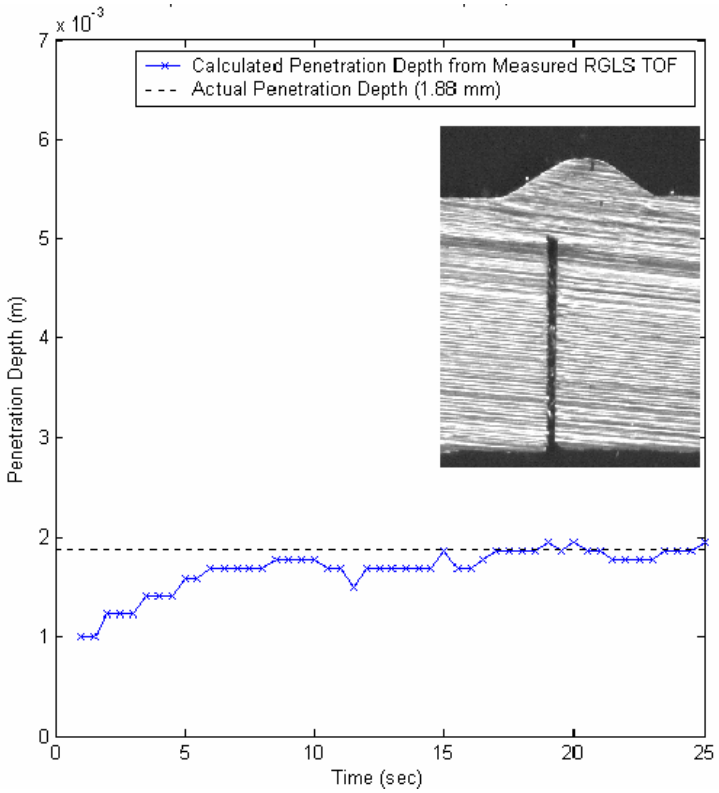

Fig. 10-9 : Measured Penetration Depth Vs. Time: 0.375 in/sec torch speed, 400 in/ min wire feed rate

In Fig. 10-10, the torch speed was 0.375 in/sec and the wire feed rate was 600 in/min.

This experimental result is similar to the result shown above in Fig. 10-6.

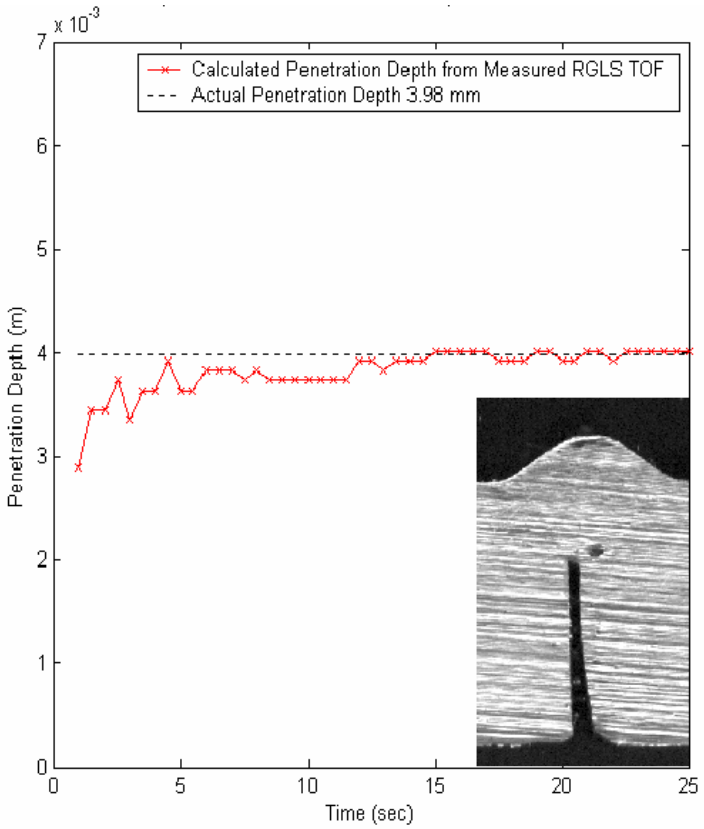

Fig. 10-10 : Measured Penetration Depth Vs. Time: 0.375 in/sec torch speed, 600 in/ min wire feed rate

In Fig. 10-11, the torch speed was 0.375 in/sec and the wire feed rate was 500 in/min. There are three different welds measured in this result. This experimental result is similar to the result shown above in Fig. 10-6. Also, all three weld penetration measurements approach the actual weld penetration depth at nearly the same time.

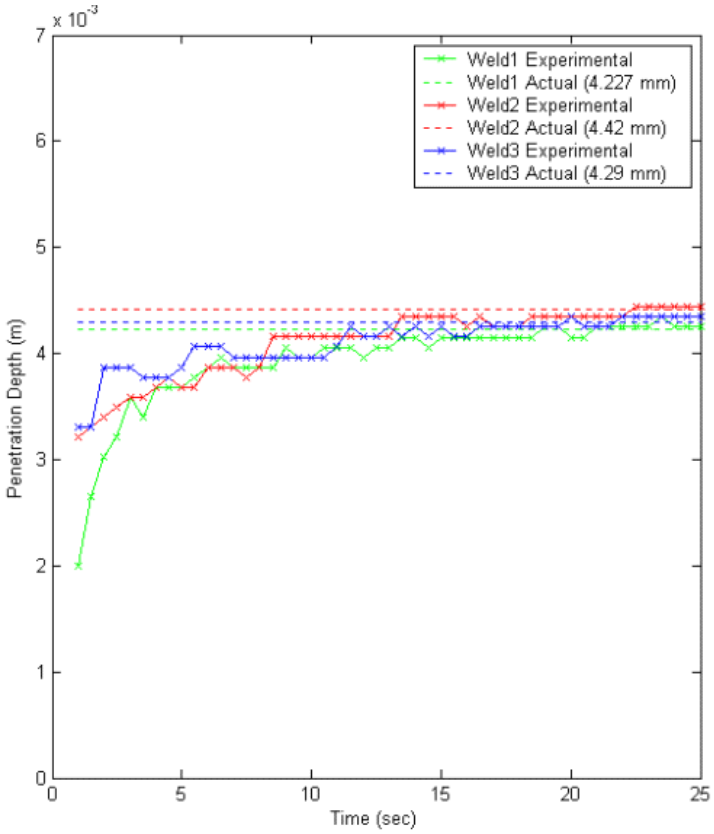

Fig. 10-11 : Measured Penetration Depth Vs. Time for three samples: 0.5 in/sec torch speed, 500 in/ min wire feed rate

Each combination of wire feed rate and weld torch speed takes a different amount of time for the weld to fully solidify and cool. The laser generation point and LURL EMAT must be placed behind the weld torch in order to allow the weld to fully solidify and cool before measuring the penetration depth. For example, the laser generation point and LURL EMAT must be placed 6.75 inches (13.5 sec * 0.5 in/sec) behind the weld torch when using 0.5 in/sec torch speed and 500 in/sec wire feed rate. A look up table of distance behind the weld torch the laser generation point and LURL EMAT must be placed versus welding parameters can be created by further experimentation. Then the laser generation point and EMAT can follow the weld torch and provide continuous weld penetration depth measurements.

These results prove the RGLS TOF method for measuring weld penetration depth can be used on-line during welding. This means for the first time, closed - loop control of weld penetration depth can be implemented. These results also show the LURL EMAT developed in Chapter 4 is capable of withstanding the harsh welding environment.

Chapter 11

Other Possible Methods for Measuring Weld Penetration Depth

The Rayleigh wave traveling on the bottom surface can generate other waves than the RGLS wave when it hits the bottom of a weld bead. These include the RGSS, RGSL, and RGLL waves as shown in Fig. 11-1 thru Fig. 11-3.

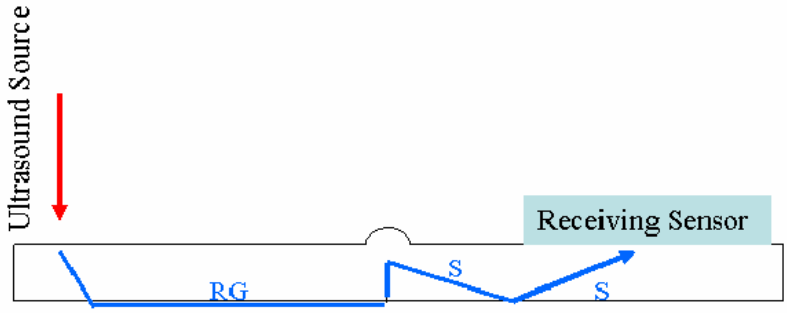

Fig. 11-1 : RGSS mode converted wave

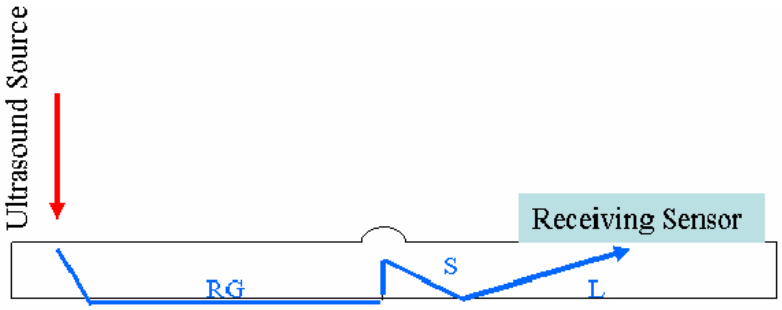

Fig. 11-2 : RGSL mode converted wave

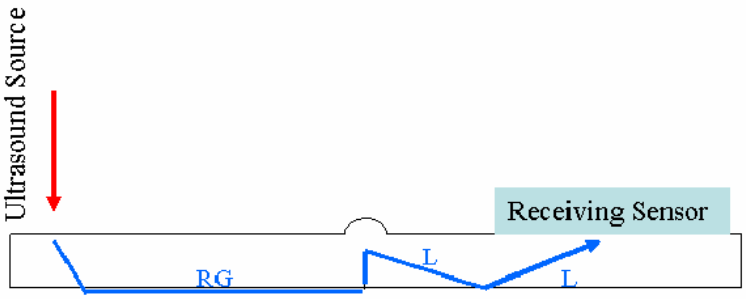

Fig. 11-3 : RGLL mode converted wave

Theoretical TOF for the RGLL, RGSL, and RGSS waves are shown in Eq. 11-1 through Eq. 11-3 respectively. Eq. 11-4 and Eq. 11-5 must be solved iteratively to find θ_{S1} and θ_{L1} for the RGSL mode converted wave.

$$RGLL_{TOF} = t_{RG} + \frac{(D_{GW} + T - d_{penetration} - D_{RG})}{C_R} + \frac{\sqrt{(2 \cdot T - d_{penetration})^2 + D_{WR}^2}}{C_L} \quad \textbf{Eq. 11-1}$$

$$RGSL_{TOF} = t_{RG} + \frac{(D_{GW} + T - d_{penetration} - D_{RG})}{C_R} + \frac{T}{C_L \cos(\theta_{L1})} + \frac{T - d_{penetration}}{C_S \cos(\theta_{S1})} \quad \textbf{Eq. 11-2}$$

$$RGSS_{TOF} = t_{RG} + \frac{(D_{GW} + T - d_{penetration} - D_{RG})}{C_R} + \frac{\sqrt{(2 \cdot T - d_{penetration})^2 + D_{WR}^2}}{C_S} \quad \textbf{Eq. 11-3}$$

$$\frac{\sin(\theta_{S1})}{C_S} = \frac{\sin(\theta_{L1})}{C_L} \quad \textbf{Eq. 11-4}$$

$$D_{WR} = (T - d_{penetration}) \cdot \tan(\theta_{S1}) + T \cdot \tan(\theta_{L1}) \quad \textbf{Eq. 11-5}$$

where:

C_R, C_S, C_L: Rayleigh, shear, and longitudinal wave speeds

t_{RG} : Time for RG wave generation

D_{RG} : Horizontal distance between ultrasound generation point and RG wave generation point

D_{GW} : Distance between ultrasound generation point and weld seam

D_{WR} : Distance between weld seam and ultrasound sensor

T : Sample thickness or distance between opposite surfaces

$d_{penetration}$: Penetration depth of weld

θ_{S1} : Reflection angle of shear wave from bottom surface

θ_{L1} : Reflection angle of longitudinal wave from bottom surface

Since these waves also travel from the bottom of the weld sample to the bottom of the weld bead, the TOF of these waves can also be used to measure weld penetration depth. Experiments were done to see if weld penetration measurements could be obtained using these waves.

11.1. Experimental Setup for the RGSS TOF Method of Weld Penetration Depth Measurement

The experimental Setup for the RGSS wave is shown in Fig. 11-4. Laser pulses from a Laser Photonics Nd:YAG laser is redirected to the surface of the sample using a 45^{o} mirror. The LURL EMAT is placed on the other side of the weld bead against an adjustable locating stop. Pre-welded samples are fixed at a known position using clamps. The LURL EMAT signal is fed into a Khron-hite filter set to a 100 khz to 5 Mhz band pass filter. The signal is digitized using the GAGE 6012 PCI A/D Card.

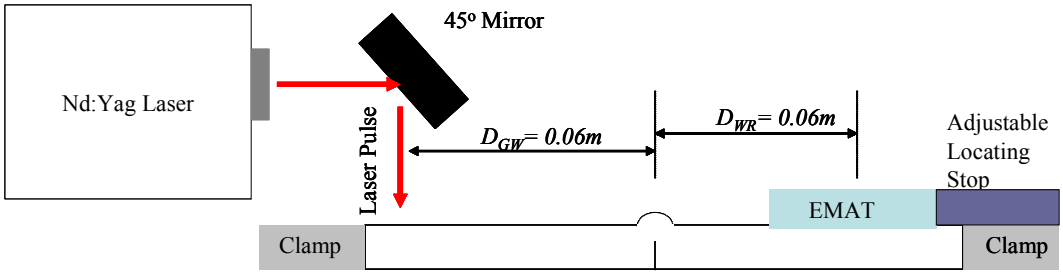

Fig. 11-4 : Experimental Setup to Measure Weld Penetration Depth using RGSS waves

An example signal with the RGSS wave is shown in Fig. 11-5. RGSS is not acquired as well as the RGLS wave because of the shallower incident angle into the LURL EMAT. Reflections and echoes from the top surface Rayleigh wave may also interfere with the RGSS wave in the pre-welded samples because the Rayleigh wave reaches the LURL EMAT before the RGSS wave. The distance between generation and reception points was modified to 0.12 m versus 0.16 m for the RGLS TOF method in an effort to increase the TOF difference between the Rayliegh and RGSS wave.

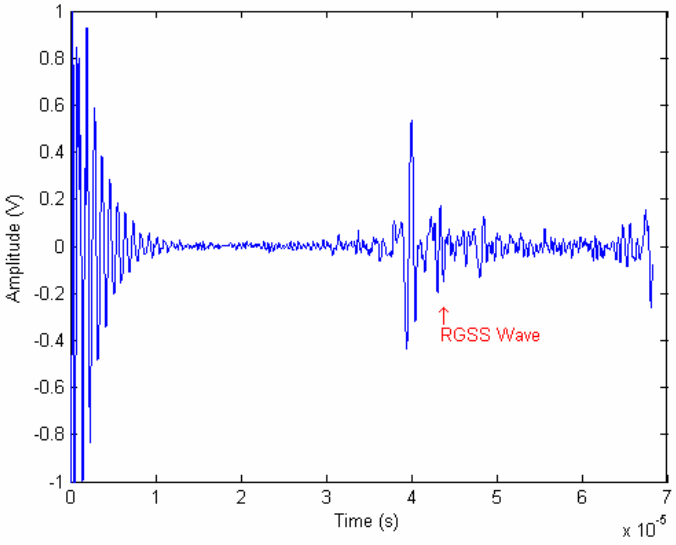

Fig. 11-5 : Example signal with RGSS Wave

11.2. RGSS TOF Method of Weld Penetration Depth Measurement Experimental Results

The experimental results for 5 pre-welded samples using the RGSS TOF weld penetration depth measurement method are given below:

Table 11-1 : RGSS method weld penetration depth measurement results

Sample Number	Actual Penetration Depth	RGSS TOF Penetration Depth	Difference	Absolute Percent Error
D1	4.36E-03	4.42E-03	-6.40E-05	1.47
D2	3.57E-03	3.50E-03	6.10E-05	1.71
D3	4.08E-03	3.96E-03	1.13E-04	2.77
D4	4.42E-03	4.42E-03	-8.00E-06	0.18
D5	3.60E-03	3.66E-03	-5.80E-05	1.61

Average Percent Error	1.55
Minimum Percent Error	0.18
Maximum Percent Error	2.77
Standard Deviation of Difference	7.69E-05

The average percent error of 1.55% and standard deviation of the difference between measured and actual of 7.69×10^{-5} is similar to the results obtained using the RGLS TOF method of weld penetration depth measurement. This RGSS TOF method for measuring weld penetration depth is suited for thicker weld samples since the Rayleigh wave will arrive much earlier than the RGSS wave and would not be able to interfere with the RGSS wave.

11.3. Experimental Setup for the RGSL and RGLL TOF Method of Weld Penetration Depth Measurement

The experimental setup for the RGSL and RGLL wave is shown in Fig. 11-6. The RGSL and RGLL method for weld penetration depth can be used with a longitudinal EMAT. However, a longitudinal EMAT was not available for this research project so a VP-103 Longitudinal Wave PZT pinducer was used. Laser pulses from a Laser Photonics Nd:YAG laser is redirected to the surface of the sample using a 45^{o} mirror. A VP-1093 Longitudinal Wave PZT Pinducer is placed on the other side of the weld bead against an adjustable locating stop. Pre-welded samples are fixed at a known position using clamps. The pinducer signal is fed into a Khron-hite filter set to a 100 kHz to 5 MHz low pass filter. The signal is digitized using the GAGE 6012 PCI A/D Card.

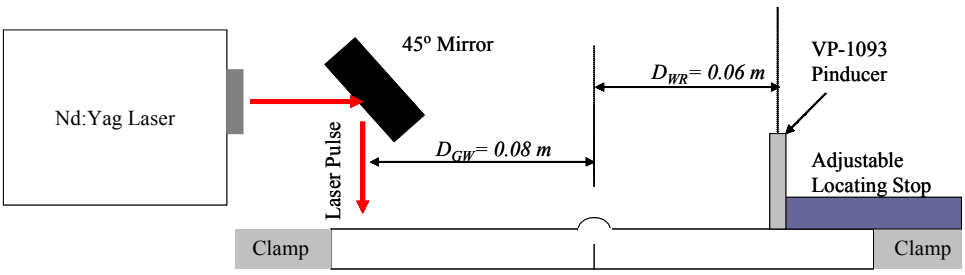

Fig. 11-6 : Experimental Setup to Measure Weld Penetration Depth using RGSL and RGLL waves

An example signal with the RGSL wave is shown in Fig. 11-7. RGSL wave is not acquired as well as the RGLL wave because of the shallower incident angle into pinducer. It requires moving the pinducer close to the weld bead to increase the incident angle into the pinducer. However, the surface wave will interfere with the RGSL and RGLL waves if the pinducer is moved to close to the weld bead. The distance between the generation point and weld bead was set at 0.08 m and the distance between the weld bead and pinducer was set at 0.06 m to get acceptable results.

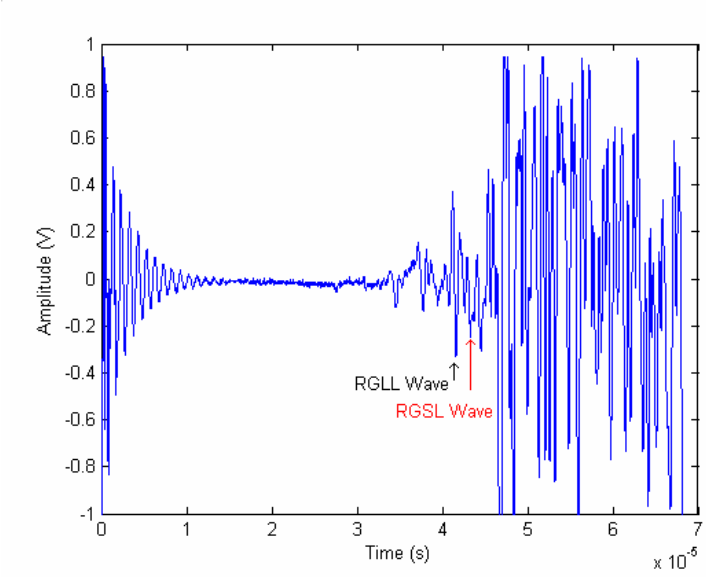

Fig. 11-7 : Example signal with RGSL and RGLL Wave

11.4. RGSS TOF Method of Weld Penetration Depth Measurement Experimental Results

Experimental results for 5 pre-welded samples using the RGSL and RGLL TOF weld penetration depth measurement method are given below:

Table 11-2 : RGLL method weld penetration depth measurement results

Sample Number	Actual Penetration Depth	RGLL TOF Penetration Depth	Difference	Absolute Percent Error
E1	2.50E-03	2.47E-03	3.20E-05	1.28
E2	3.70E-03	3.67E-03	3.60E-05	0.97
E3	4.26E-03	4.18E-03	7.50E-05	1.76
E4	5.34E-03	5.30E-03	3.50E-05	0.66
E5	2.95E-03	2.98E-03	-3.90E-05	1.32

Average Percent Error	1.20
Minimum Percent Error	0.66
Maximum Percent Error	1.76
Standard Deviation of Difference	4.13E-05

Table 11-3 : RGSL method weld penetration depth measurement results

Sample Number	Actual Penetration Depth	RGSL TOF Penetration Depth	Difference	Absolute Percent Error
E1	2.50E-03	2.50E-03	1.00E-06	0.04
E2	3.70E-03	3.72E-03	-1.90E-05	0.51
E3	4.26E-03	4.23E-03	2.90E-05	0.68
E4	5.34E-03	5.29E-03	4.50E-05	0.84
E5	2.95E-03	2.97E-03	-2.70E-05	0.92

Average Percent Error	0.60
Minimum Percent Error	0.04
Maximum Percent Error	0.92
Standard Deviation of Difference	3.08E-05

The average percent error of 1.20% and standard deviation of the difference between measured and actual of 4.13×10^{-5} using the RGLL TOF method of measuring weld penetration depth is similar to the results obtained using the RGLS TOF method. The average percent error of 0.60% and standard deviation of the difference between measured and actual of 3.08×10^{-5} using the RGLL TOF method of measuring weld penetration depth is also similar to the results obtained using the RGLS TOF method.

These results indicate that the RGLS, RGSS, RGLS and RGLL TOF methods can all be used to measure weld penetration depth.

Chapter 12

Conclusion

The overall objective of this research area is to create a robotic welding system with real time quality control using non-contact sensors. Previous research described in Chapters 2 and 3 focused on using an ultrasonic shear wave TOF to measure weld penetration depth. First, laser generation of ultrasound and EMAT reception was researched. A laser phased array has been implemented to try to increase signal strength of the shear wave. Also, finite-element models have been created to predict high temperature effects on shear wave propagation and TOF. The objective of this research was to use a brand new technique, frequency of modulation of a laser phased array (FMLPA), to determine weld penetration depth. The background theory for the FMLPA was conceived from discrepancies between array gain formulations used in prior research and laser generated ultrasound.

Initially, a new custom electromagnetic transducer designed to be physically smaller, more broadband, and with higher signal to noise was developed to assist in validating the FMLPA. The specifications for the new EMAT are given in Chapter 4. The FMLPA was experimentally validated and matched predicted analytical models very well in Chapter 5 when ultrasound from each array member did not interfere with each other. Also, the array gain formulations were experimentally validated when ultrasound from each array member interfered with each other. However, there were a few surprises in the experimental results when validating the array gain. The array gain results must take into

account different types of ultrasonic waves generated by the laser and their relative amplitudes.

Due to the surprises in the experimental results when validating the array gain, this research path reversed its course and initiated more fundamental research. Previously there was theory but no experimental result showing which ultrasonic waves are observable when laser generated ultrasound and EMAT were used on a flat plate. This research experimentally determined that shear EMATs and PZTs can both acquire Rayleigh, shear, LS mode converted, and L(M)S(N)R_LS mode converted ultrasonic waves as shown in Chapter 6. The L(M)S(N)R_LS mode converted waves was another surprise since no prior research has described this wave. The L(M)S(N)R_LS mode converted waves however are very important. If they are allowed to propagate past the weld seam, any other ultrasonic wave used to measure weld penetration depth will be obscured or modified. Therefore, the L(M)S(N)R_LS mode converted waves determine the maximum weld penetration depth that can be observed using ultrasound for butt welds.

There was no experimental validation of the ultrasound wave speeds in the 1018 steel weld samples so that was checked also. Experiments in Chapter 7 show that the published ultrasound wave speeds match the published values for mild steel.

The next step was to determine if a shear wave can be observed on a pre-welded sample in Chapter 9. However, there was a strong unknown wave preceding the expected shear

wave. This unknown wave had the potential of masking the shear wave so experiments were carried out to determine the unknown wave. The unknown wave turned out to be the RGLS mode converted wave. During the determination of the RGLS wave, it was discovered that bulk waves generated on one side of a flat plate using laser ultrasound can generate a Rayleigh wave on the opposing surface. This is a new and previously undiscovered mechanism for generating a Rayleigh wave. Simulations show that the RGLS wave can mask the shear wave. Therefore, both the FMLPA and shear wave TOF techniques have proven to be impractical for real-time control.

This negative result was turned into an advantage with the formulation of the RGLS TOF method for measuring weld penetration depth. The RGLS TOF method for measuring weld penetration depth has proven to be highly accurate, precise, and repeatable as described in Chapter 10. The RGLS TOF method for measuring weld penetration depth has been demonstrated to work both off-line after welding and real-time during welding. During welding, the weld must solidify before taking a measurement. The accuracy was demonstrated to be less than 0.1 mm using available equipment. In Chapter 11, other waves such as the RGSL, RGLL, and RGSS waves have been used to measure weld penetration depth also.

Although the FMLPA technique was proven to be impractical, the RGLS wave TOF method developed has met the ultimate goal of this research area. Weld penetration depth can now be reliably measured both on-line and off-line. The RGLS wave TOF method is suited for non-destructive and non-contact sensing, and will help future researchers

achieve closed-loop control and automation of the GMAW process to improve quality and efficiency, and reduce waste and cost.

Listing of Research Contributions

Major Results:

- FMLPA exists when using laser phased arrays
- Created a new custom EMAT (LURL EMAT) suited for this research
- LS modes will obscure the shear wave if allowed to propagate though a weld bead.
- Shear TOF and FMLPA methods for measuring weld penetration depth is impractical for real-time weld control
- New RGLS TOF method can measure weld penetration depth with accuracy, precision, and repeatability

Experimentally proved:

- FMLPA follows theory developed in proposal
- Array Gain Equations are valid when wave fronts from each array member interfere.
- LURL EMAT, NIST EMAT, and V153 PZT all see Rayleigh, shear, and LS mode converted waves on flat plate
- LS modes will obscure the shear wave if allowed to propagate though a weld bead.
- Previously unknown signal is the RGLS mode converted wave
- New RGLS TOF method can measure weld penetration depth with accuracy, precision, and repeatability

Derived:

- Proof for Vogel's array gain equation
- Theoretical array gain with different time delays between array members (Proved slight differences in time delays do not affect the array gain very much)

- Theoretical array gain with 7 point line source array members (Proved the 7 point line sources used in our experimental setup do not affect the array gain very much)
- Theoretical equations that can be used to derive directivity patterns when the shear wave and surface (Rayleigh) wave arrive at receiver simultaneously.
- Recursive equations for LS and L(M)S(N)R_LS mode converted waves TOF.
- Maximum penetration depth D max penetration allowable for a given source to sensor distance, *D*.
- Theoretical RGLS TOF equation.
- Theoretical RGSS, RGLL, RGSL TOF equations.

Manufactured:

- Capture and Analysis Programs (before proposal)
- Welder to laser communication interface (before proposal)
- Fiber chuck for distal end of FFBLPA (before proposal)
- New custom EMAT (LURL EMAT)
- Program to measure actual weld penetration depth using an optical scanner.

Bibliography

1. Nagarajan, Sundaram, and Banerjee, Probal, and Chen, WeiHua, and Chin, Bryan A.,"Control of the Welding Process Using Infrared Sensors, IEEE Transactions on Robotics and Automation, Vol. 8, No.1, Feb. 1992 pp. 86-93

2. Santos, T.O, and Caetano, R. B., and Lemos, J. M. and Coito, F. J. "Multipredictive Adaptive control of Arc Welding Trailing Centerline Temperature," IEEE Transactions on Control systems technology, Vol. 8, No. 1, January 2000, pp. 159-169

3. Yu M. Zhang, Radovan Kovalevic, and Lin Li, "Adaptive Control of Full Penetration Gas Tungsten Arc Welding," IEEE Transactions of Control Systems Technology, Vol. 4, No. 4, July 1996 , pp. 394 -403

4. Alzamora, G., and Ikeya, H., and Kaneko, Y., and Ohshima, K,, and Chen, Q.," Intelligent welding Robot System.", Proceedings of the Singapore International Conference on Intelligent Control and Instrumentation, Vol.2, 1992 pp. 1058-1062

5. Bigand, A., and Messaadi, K.," Arc Welding Fuzzy Control Using Neural Net Supervisor," Proceedings of the Fifth IEEE International Conference on Fuzzy Systems, Vol. 3, 1996, pp. 2003-2006

6. Chen, S. B, Wu, L., and Wang, Q.L.," Self Learning Fuzzy Neural Networks for Control of the Arc Welding Process," IEEE International Conference on Neural Networks, Vol. 2, 1996 pp. 1209-1214

7. Li, D., and Song, Y., and Feng, Y., "On Line Monitoring of Weld Defects for Short-circuit Gas Metal Arc Welding Based on the Self-Organize Feature Map Neural Networks," Proceedings of the IEEE-INNS-ENNS International Joint Conference on Neural Networks, Vol. 5, 2000, pp. 239-244

8. Peng, J., Chen, Q., Lu, J., Jin, J., and Van Luttervelt, C.A., "Real Time Optimizations of Robotic Arc Welding Based on Machine Vision and Neural Networks," Proceedings of the 24th Annual Conference of the IEEE Industrial Electronics Society, Vol. 3, 1998, pp. 1279-1280

9. Kaneko, Y., and Yamane, S., and Kugal, K., and Ohshima, K., " Neural Control of Weld Pool in the Robotic Welding," Conference Record of the Industry Applications Society Annual Meeting, Vol. 3, 1994 pp. 1914-1919

10. Kim, G., and Kang, S., and Lee, S.," A study on the Estimate of Weld Bead shape and the compensation of Welding Parameters by considering Weld Defects in horizontal Fillet Welding," Third International Conference on Knowledge-Based Intelligent Information Engineering Systems, 1999, pp. 212-216

11. Legendre, S., and Massicotte, D., and Goyette, J., ”Ultrasonic Aluminum Weld Testing Method Based on the Wavelet Transform and Neural Classifier,” Proceeding of the 1999 IEEE Canadian Conference on Electrical and Computer Engineering, May 1999, pp. 761-765

12. Lin, R., and Fischer, G., “ An Online arc welding quality monitor and process control system,” International IEEE/IAS Conference on Industrial Automation and Control: Emerging Technologies, 1995 pp. 22-29

13. Ohshima, K., and Yabe, M., and Akita, K., and Kugai, K., ”Sensor Fusion Using Neural Network in The Robotic Welding” Industry Applications Conference, Vol. 2, 1995 pp.1764-1769

14. Adolfsson, S., and Bahrami, A., and Claesson, I.,” Quality Monitoring in Robotised Welding using Sequential Probability Ratio Test., IEEE TENCON-Digital Signal Processing Applications, 1994. pp. 635-640

15. Andersen, K., and Cook, G., and Karsai, G., and Ramaswamy, K.,” Artificial Neural Networks Applied to Arc Welding Process Modeling and Control,” IEEE Transactions on Industry Applications, Vol. 26, No. 5, September/October, 1990, pp. 824-830

16. Barborak, D., and Conrardy, C., and Madigan, B., and Paskell, T.,” Through – Arc” Process Monitoring Techniques for control of Automated Gas Metal Arc Welding.” Proceeding of the 1999 IEEE International Conference on Robotics & Automation, May 1999, pp. 3053-3058

17. Doumanidis, Charalabos,” Multiplexed and Distributed Control of Automated Welding,” IEEE Control Systems Magazine, Vol. 14, Issue. 4, Aug. 1994, pp. 13-24

18. Brzakovic, D. and Khani, D. T. “Weld Pool Edge Detection for Automated Control of Welding,” IEEE Transactions on Robotics and Automation, Vol. 7, No. 3, June 1991pp. 397-403

19. Bastos, T.F., and Martin, J.M., and Calderon, L., and Ceres, R., “Weld Seams Detection and Recognition for Robotic Arc-Welding.” 1994 IEEE International Symposium on Industrial Electronics, 1994 pp. 310-315

20. Umeagukwu, C., Maqueira, B., and Lambert, R., “Robotic Acoustic Seam Tracking: System Development and Application,” IEEE Transactions on Industrial Electronics, Vol. 36, No. 3, Aug. 1989, pp. 338-348.

21. Graham, G., Ph.D. Dissertation. Georgia Institute of Technology 1995

22. Hopko, S., Ph.D. Dissertation. Georgia Institute of Technology. 1998

23. Ogi, H., and Hirao, M., and Ohtani, T., " Line-Focusing Electromagnetic Acoustic Transducers for the detection of Slit Defects," IEEE Transactions on Ultrasonics, Ferroelectrics, and Frequency Control, Vol. 46, No.2, March 1999, pp. 341-346

24. Yamasaki, T., and Tamai, S., and Hirao, M.,"Arrayed-Coil Emat for Longitudnal Wave in Steel Wires," Proceedings of Ultrasonics Symposium, Vol. 1, 1998, pp.789-792

25. Mi, B., Ph.D. Dissertation. Georgia Institute of Techonology

26. Clark, A.V, and Schaps, S.R., and Fortunko, C.M.,"A Well-Shielded Emat for on-line ultrasonic monitoring of GMA Welding," Proceedings of Ultrasonics Symposium, Vol. 1, 1991 pp. 337-340

27. Edwards, C. and Palmer, S. B. "Wideband Electromagnetic Acoustic Transucers utilizing neodym Iron Boron Permanent Magnets." IEEE Transactions on Magnetics, Vol. 26, No. 5, Sept 1990, pp. 2080-2084

28. Kaltenbacher, M., and Ettinger, K. and Lerch, R., and Tittmann, B.," Finite Member Analysis of Coupled Electromagnetic Acoustic Systems," IEEE Transactions on Magnetics, Vol. 35, No. 3, May 1999, pp. 1029-1034

29. Ludwig, R., and Palanisamy, R., "Numerical Simulations of an Electromagnetic Acoustic Transducer-Receiver System for NDT Applications." IEEE Transactions on Magnetics, Vol. 29, No. 3, 1993, pp. 2081-2089

30. Hutchins, D. A., and Schindel D. W., "Advances in Non-contact and Air-Coupled Transucers," 1994 Ultrasonics Symposium, pp. 1245-1254

31. Boltz, E. S., and Fortunko, C. M., " Absolute Sensitivity Limits of Various Ultrasonic Transducers," Proceedings of Ultrasonics Symposium, Vol.2, 1995, pp. 951-954

32. Graham, G.M., Ume, I.C., "Automated System for Laser Ultrasonic Sensing of Weld Penetration", *Mechatronics*, Vol. 7, No. 8, 1997, pp.711-21

33. Graham, G.M., Sanderson, T.M., Ume, I.C., "Intelligent Welding with Laser Ultrasonic Sensing", *Proceedings of 1st World Congress on Intelligent Manufacturing Processes and Mayaguez*, San Juan, Puerto Rico, Feb. 1995, pp. 1043-53

34. Matt Miller, Bao Mi, Akio Kita, and, I. Charles Ume, "Development of Automated Real-Time Data Acquisition System for Robotic Weld Quality Monitoring",*Journal of Mechatronics*, v.12, n.9-10, p.1259-69, 2002

35. Scruby, C.B., and Drain, L.E., *Laser Ultrasonics:Techniques and Applications,* Adam Hilger, New York.

36. Rose, L. R. F., "Point-Source Representation for Laser-Generated Ultrasound", Journal of Acoustics Society of America, 1984, 75 (3), 723-732

37. Vogel, J. A., Bruinsma, J. A., and Berkhout, A.J., "Beam steering of Laser Generated Ultrasound," Proceedings of Ultrasonics International, 1987, pp. 141-152

38. Ludwid, R., You, Z., Palanisamy, R., "Numerical Simulations of an Electromagnetic Acoustic Transducer-Receiver System for NDT Applications", *IEEE Transactions on Magnetics*, Vol. 29, No. 3, 1993, pp. 2081-89

39. R. Pierce, C. Ume, and J. Jarzynski, " Temporal modulation of a laser source for the generation of ultrasonic waves", *Ultrasonics*, Vol. 33, No. 2, pp. 133-137

40. T.W. Murray, M. Marincek, and J.W. Wagner,"Narrow-band and directed ultrasound generated by laser arrays", Proceedings of Ultrasonics Symposium, Vol.1, 1993, pp. 639-626